Scholars' Mine

Masters Theses   Student Theses and Dissertations

Spring 1982

The influence of manganese oxide on sintering of a commercial natural magnesite.

Alamar Kasan Duarte

Recommended Citation

Duarte, Alamar Kasan, "The influence of manganese oxide on sintering of a commercial natural magnesite." (1982). *Masters Theses*. 3917.
https://scholarsmine.mst.edu/masters_theses/3917

THE INFLUENCE OF MANGANESE OXIDE ON SINTERING

OF A COMMERCIAL NATURAL MAGNESITE

BY

ALAMAR KASAN DUARTE, 1952-

A THESIS

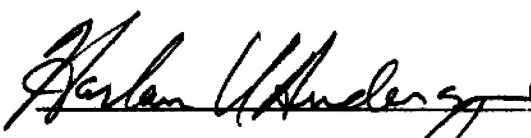Presented to the Faculty of the Graduate School of the

UNIVERSITY OF MISSOURI-ROLLA

In Partial Fulfillment of the Requirements for the Degree

MASTER OF SCIENCE IN CERAMIC ENGINEERING

1982

Approved by

_____ (Advisor) _____

_____

ABSTRACT

Sintering studies on a commercial natural magnesite have been done to investigate the influence of MnO doping (MnO concentration from 0.16 to 2.50 wt.%) on the densification process over the temperature range 1520 to $1760^{\circ}C$, over periods of time from 3,600 to 57,600s in both oxidizing and reducing atmospheres (Air and $P_{O_2} = 10^{-7}$ KPa. In an air atmosphere the additions of MnO enhances the densification process. This fact may be associated with an increase in lattice diffusion of Mg ions due to an increase in cation vacancies in the MgO lattice from the presence of Mn^{+3}. Under reducing conditions MnO additions do not effect densification, which may be due to the minimization of cation defects since Mn should be in the +2 oxidation state. In air, sintering temperature was found to be more important than time. On the other hand, under reducing conditions little densification occurred for temperatures greater than $1640^{\circ}C$. This appears to be associated with an evaporation process which tends to suppress the densification rate.

ACKNOWLEDGEMENTS

The author wishes to express his appreciation for the guidance he received from his advisor, Dr. Harlan U. Anderson. Appreciation is also expressed to Dr. Robert E. Moore, Head of the Department of Ceramic Engineering and also to all his teachers at the University of Missouri-Rolla who directly or indirectly have contributed to the success of this research.

The author is very grateful to the company MAGNESITA SA of Brazil for financial support during the course of this investigation. A special thanks is dedicated to the Department of R & D of MAGNESITA SA for its assistance in preparing raw materials, making chemical analysis, and microstructure studies.

Finally, the author expresses his gratitude to his wife, Toê, his sons, Yan and Gustavo, his relatives, his friends, and dedicate this thesis to them.

TABLE OF CONTENTS

LIST OF ILLUSTRATIONS

LIST OF TABLES

I. INTRODUCTION

In the last thirty years, basic refractories have become increasingly important to the refractory industry. They have found widespread application both in basic steel-making process and in non-ferrous applications such as the production of glass, copper and cement.[1] Magnesia raw materials, as dead-burnt MgO grain, have been used in all three main types of basic refractories; in magnesite refractories as a unique component, in chrome-magnesite refractories mixed with chrome ore, and finally in dolomite refractories in association with doloma (MgO.CaO) refractory grain.

Dead-burnt MgO grain for use in basic refractories is obtained by sintering either naturally occurring magnesite ($MgCO_3$) or $Mg(OH)_2$ precipitated from either sea-water or brine solutions.[2] In both cases, the process of sintering may involve a single or a double thermal treatment. In the single stage firing process, the material is fed directly into a shaft or rotary kiln, where it is subjected to temperatures greater than $1700^{\circ}C$ to produce what is called dead-burnt magnesia grain. In the two-stage firing process, the material is first calcined at temperatures between 800 to $1000^{\circ}C$, then pelletized at pressures of approximately 300 MPa, and finally heated to temperatures up to $2000^{\circ}C$ in

rotary or shaft kilns. The grain obtained by the two-step process is denser and more homogeneous than that obtained through the single firing process.[2,3]

In general, the properties most desired for the dead-burnt MgO grain are high density and high temperature mechanical strength. These properties directly influence both the slag resistance and the stress the material can withstand during service.[4] The MgO grain density obtained during the sintering process is dependent upon many variables such as particle size distribution and chemical impurities of the raw materials, calcination and pelletizing conditions, firing temperature, rate of temperature rise, time at maximum temperature and atmosphere. The mechanical strength at high temperatures depends mainly upon grain density and development of a microstructure during the sintering process, which has high MgO to MgO grain bonding and low silicate bonding.[5] The silicate bonding needs to be minimized since in many instances it leads to a liquid phase under normal use conditions which greatly decreases mechanical strength.[4,5]

The major impurities present in MgO raw materials are CaO, SiO_2, Fe_2O_3 and Al_2O_3 in natural magnesites and CaO, SiO_2, Fe_2O_3, Al_2O_3 and B_2O_3 in sea-water magnesia.[1,2] The presence of B_2O_3, even in concentrations as low as 0.05 wt.% affects the hot mechanical strength of the MgO grain. This is done by fluxing the silicate phase at

temperatures as low as $1200^{\circ}C$ and by increasing the
amount of liquid coexisting with MgO at higher tempera-
tures. As a matter of fact, B_2O_3 constitutes the major
technical disadvantage of sea-water MgO grain in
comparison with MgO grain from natural magnesites.[6,7]

There are two types of natural magnesites: crypto-
crystalline and coarse crystalline.[3,4] One of the largest
deposits of coarse-crystalline magnesite in the world
occurs in Brazil. The three different MgO grains
produced with the Brazilian natural magnesite have been
described in the literature[8-10] and are shown in Table I.
Grain M10 is produced by the single firing process and
grains M20 and M30 are produced by the double firing
process. The first two MgO grains have approximately
the same chemical analysis because they are derived from
the same deposit. The MgO grain called M30 comes from a
purer deposit and has MgO content higher than 98.0 wt.%,
calcined basis.

One interesting feature of some deposits of
Brazilian magnesite, as compared to other sources, is
the presence of relatively high concentrations of MnO.
The Brazilian magnesite has MnO concentrations ranging
from 0.16 wt.% in the purest deposit to 0.83 wt.% in
the most impure one as shown in Table I. Few studies
have been done on the influence of MnO on the properties
of the MgO grain. The purpose of this work is to

TABLE I

CHARACTERISTICS OF DEAD BURNT MgO GRAINS FROM THE
BRAZILIAN NATURAL MAGNESITE

	SINTER "M10"	SINTER "M20"	SINTER "M30"
Chemical Analysis (wt%)			
MgO	95.35	95.35	98.48
CaO	0.48	0.48	0.52
SiO_2	1.25	1.25	0.32
Fe_2O_3	1.80	1.80	0.43
Al_2O_3	0.29	0.29	0.07
MnO	0.83	0.83	0.16
B_2O_3	0.005	0.003	0.003
Bulk Density $(Kg/m^3) \times 10^{-3}$	2.89 – 2.95	3.24 – 3.30	3.30 – 3.36
Apparent Porosity (%)	16 – 18	3 – 5	1 – 2

investigate the influence of small amounts of MnO
(ranging from 0.16 to 2.50 wt.%) on the sintering behavior
of the purest Brazilian natural magnesite and to see how
the manganese oxide will influence the hot mechanical
strength of the grain.

II.   LITERATURE REVIEW: SINTERING THEORY OF CERAMIC OXIDES

A.   GENERAL CONSIDERATIONS

Sintering may be defined as the process by which loose powders are compacted and then fired at temperatures sufficient to be transformed into useful objects.[11] During the firing process many changes may occur in the material.   There may be initially a decomposition or phase transformation in some of the phases present.   On further heating, microstructural changes occur with size and shape of grains and pores.[12,13]   Under certain conditions of temperature and composition, liquid as a minority phase may be present for multicomponent systems.[11]

A powder compact, as formed, contains a large percentage of pores.   In order to maximize such properties as strength, thermal conductivity, corrosion resistance, density, etc., these pores need to be eliminated during the sintering process.   Since the elimination of porosity is so important, the discussion on sintering is focused mainly on changes occurring with size and shape of the pores during the firing process.[13]

There are many variables which may profoundly influence the rate of the sintering process and the properties of the product.   Some of the these variables are the nature of the powder, the pressing conditions, the impurities present, the sintering time, the temperature

and the atmosphere.[12] Sintering is very complex due to the number of mechanisms responsible for mass transport, as well as to the changes in the geometry of the particles occurring during the process. For simplicity, investigators have formulated their models based on geometrically defined particles, in general equisized spheres. They have also assumed a single-phase solid, which remains solid during the process, and they have not considered chemical reactions taking place during densification.[11]

B. MECHANISMS OF MATERIAL TRANSFER

Sintering involves the transport of atoms or ions from one part of a particle to the region of contact with other particles. Resulting from this movement, necks form between particles.[11] The neck formation can occur by two different classes of mechanisms of matter transport: those which can produce shrinkage and those which cannot.[12]

1. Mechanisms Which Produce Densification. Two general processes may operate to produce shrinkage: plastic flow and bulk diffusion mechanisms, as shown in Figure 1. Plastic Flow by dislocation movement is not important for crystalline oxides due to the few number of slip systems present in these materials.[11] However, plastic flow by viscous flow occurs in the sintering of glass,[15] and plastic flow as a general process is an
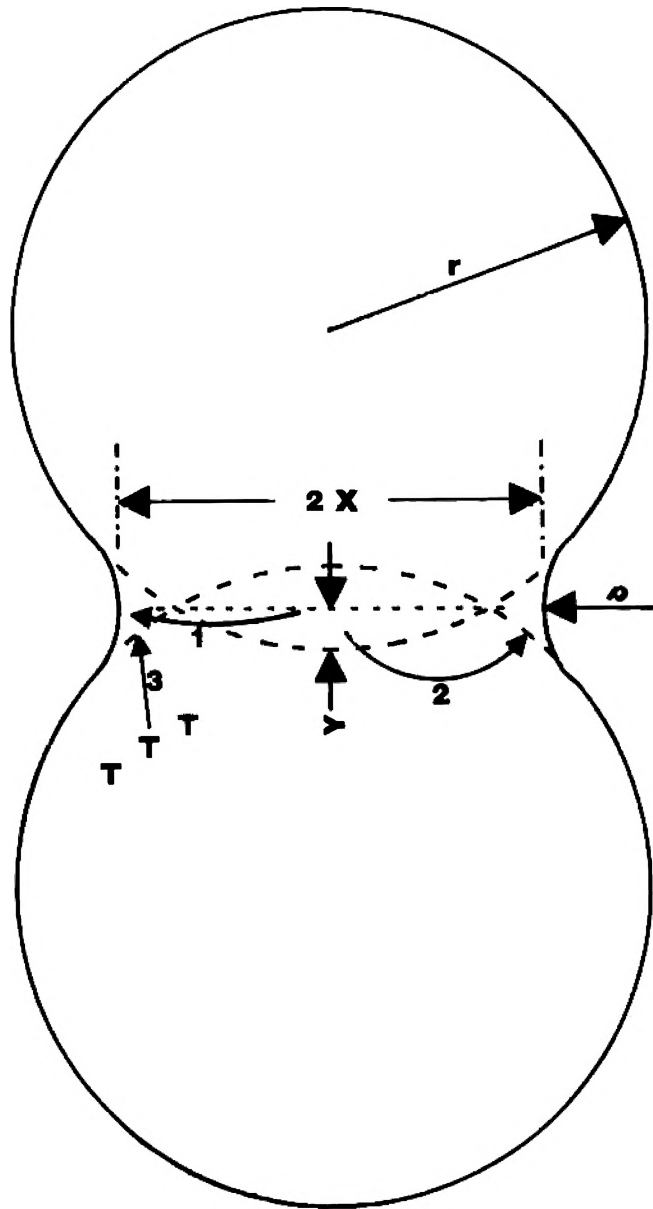
Figure 1. Two spheres sintering model for mechanisms which produce densification: (1) grain-boundary diffusion, (2) lattice diffusion, and (3) plastic flow by dislocation mechanism (after Anderson[11]).

important mechanism in hot pressing.[11] Bulk diffusion, either grain boundary or lattice diffusion, occurs when the matter in the contact area between the two grains or in the interior of the grains, diffuses to pores on the surface, so the grains approach each other, causing shrinkage and densification of the material.

Bulk diffusion is the most important mechanisms of densification. The relative importance of grain boundary and lattice diffusion contributions to the whole process has been discussed.[14] The diffusion transport of ions through the crystals is accompanied by an opposite flux of lattice vacancies. As a result, the sintering process is generally discussed in terms of vacancies, their formation at vacancy sources, their diffusion, and their annihilation at vacancy sinks.[16-18] The pores are the vacancy sources and the grain boundaries are assumed to be the vacancy sinks. In general, the activation energy for lattice diffusion is greater than that for grain boundary diffusion, so the former mechanism becomes more favorable at higher temperatures. Minor additions of second components which produce lattice defects can cause an increase in the diffusion rate through the lattice thereby increasing the rate of sintering.[14]

When liquid phase is present, the remaining solid particles can move closer together and eliminate porosity by viscous flow of the liquid. In addition, the pores

may also be eliminated by diffusion through the liquid. The important technological aspect of liquid phase sintering is that the sintering temperature for densification may be decreased.[12] However, this type of mechanism will not be taken into consideration in this MgO sintering study since it probably is not important at the temperatures being used.

2. <u>Mechanisms Which do not Produce Densification</u>.

Two general processes may operate without producing shrinkage: evaporation-condensation and surface diffusion, as illustrated in Figure 2. Evaporation can occur from the convex surfaces of the particles where the chemical potential of the atoms is higher, with redeposition at the neck between particles, where the chemical potential of the atoms is lower due to the concave surface.[19] This mechanism is only important for materials with relatively high vapor pressure at the sintering temperatures.[11] Surface diffusion involves the movement of atoms or ions on the surface of a particle. It is usually important at low temperatures where surface diffusion coefficients are generally higher than either lattice or grain boundary diffusion coefficients.[19]

As discussed by Anderson,[11] surface diffusion and evaporation-condensation processes cause formation of necks between particles and change the shape of the pores, but the centers of adjacent spheres do not approach
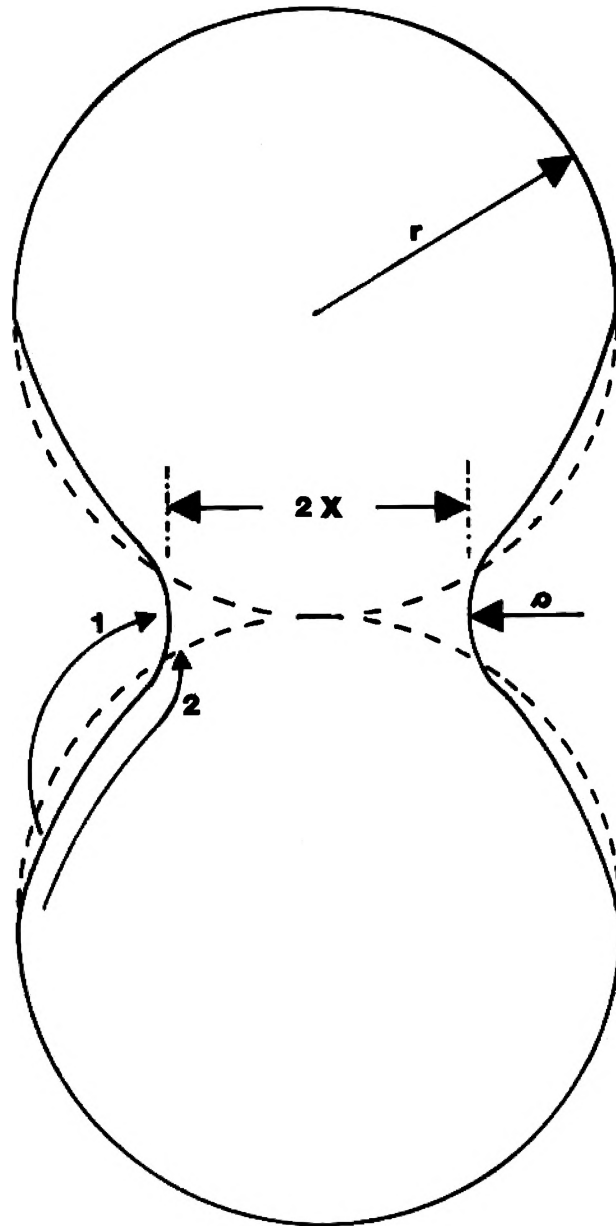
Figure 2. Two spheres sintering model for mechanisms which do not produce densification: (1) evaporation-condensation, and (2) surface diffusion (after Anderson[11]).

each other. Therefore, these two mechanisms cannot be detected with shrinkage measurements and do not lead to densification. When these two mechanisms occur simultaneously with other mechanisms which cause densification, they will have a deleterious effect on densification rates since they cause reduction in surface area and reduce the driving force for densification.[19]

In general, studies in sintering involve the identification of the mechanism of matter transport and also the determination of the effect of the important variables upon the rate. However, the identification of the mechanism of matter transport is not so simple because more than one mechanism may operate at the same time.[12] It has been established that the sintering rate is controlled by the slowest diffusing atom or ion.[11] Among the important variables which influence the sintering rate, temperature is perhaps the most easily understood because of its influence on diffusion. Particle size is also very important because the smaller the particle the higher will be the sintering rate because the transport distance of atoms to the neck will be smaller, regardless of the mechanism of matter transport.[12] Diffusion coefficient values and time complete the group of the four most important variables

affecting sintering. All of the other variables influence sintering indirectly, by modifying the contribution of this group of variables.

C. DRIVING FORCES FOR SINTERING

According to Anderson[11], the driving force for sintering is the tendency of a finely divided material to decrease its excess free energy by decreasing total surface area. The magnitude of this excess free energy depends on the size and surface curvature of the particles,[13] and can be represented by the Kelvin equation

$$\Delta G = \gamma_{sv} \; \Omega \; (\frac{1}{r_1} + \frac{1}{r_2}) \tag{2.1}$$

where ΔG is the excess free energy, γ_{sv} is the surface-free energy in the solid-vapor interface, Ω is the molar volume and r_1 and r_2 the principle radii of curvature.

From the Kelvin equation one can deduce that if the particle size and consequently the radius of curvature is small, a large excess free energy will result.[13] It is also possible to deduce that the free energy will be decreased when material is transported from either the convex surface or grain boundary of the particle to the concave neck surface during the sintering process, thereby lowering the driving force for densification.[11]

1. Driving Force for the Evaporation-Condensation
Process. The positive radius of curvature at the convex
surface of the particles (Figure 2), causes an increase
in vapor pressure of the atoms in comparison to what
would be observed for a flat surface. The small negative
radius of curvature at the concave neck surface causes
a large decrease in the vapor pressure of the atoms in
comparison to the same flat area. The resulting vapor
pressure difference between the neck area and the
particle surface may cause mass transport to the neck
area by the evaporation-condensation mechanism.[13]

It is possible to deduce from the Kelvin equation
(2.1) that Δp, the difference between the vapor pressure
of the small negative radius of curvature at the neck and
the saturated vapor in equilibrium with the nearly flat
particle surfaces, is the driving force for the evapora-
tion-condensation process, and is given by:

$$\Delta p = \frac{\gamma_{sv} M p_o}{\rho d R T} \qquad (2.2)$$

where p_o is the vapor pressure over a flat particle
surface, M is molecular weight, d is density, R is the
gas constant, T is temperature, and ρ is the radius of
curvature at the neck surface.[13]

2. Driving Forces for the Solid-State Processes.

Although the excess surface energy may be small at the particle surface, it is large enough in the neck area to cause stresses which will produce the changes in neck diameter during sintering.[20] The value for these stresses can be obtained from the Kelvin equation (2.1) and are given by:

$$\sigma = \gamma \ [(\frac{1}{x}) + (-\frac{1}{\rho})] \tag{2.3}$$

where x is the neck radius (Figure 1) and the other variables have been defined before. Since ρ is much smaller than x, for a first approximation σ is equal to $-\gamma/\rho$. The negative sign indicates that the stress acting in the neck area is tensional, directed outward. Kuczynski[20] has estimated that the values for this stress for copper powder may reach 27.6 MPa, not negligible considering the elevated temperatures at which sintering takes place.

The stress in the neck may produce mass flow, such as viscous or plastic flow, in compacts which contain large amounts of liquid phase, or which are composed entirely of glassy particles. In single-phase crystalline materials, however, the matter transport occurs by diffusion of lattice vacancies because their concentrations are different under surfaces of different

curvature.[20] It is possible to deduce that ΔC, the excess concentration of vacancies in the neck region, is the driving force for sintering for the solid state process, and is given by:

$$\Delta C = \frac{\gamma a_o^3 C_o}{\rho k T}$$ (2.4)

where C_o is the equilibrium concentration of vacancies under a flat surface, a_o^3 is the vacancy volume and k is the Boltzman's constant. This excess concentration of vacancies in the neck region will cause bulk and surface diffusion of atoms to the neck area.[20]

D. SINTERING STAGES

According to Coble[16], the sintering process can be divided into three geometrically identifiable stages: initial, intermediate and final.

1. Initial Sintering Stage. The initial stage is the one in which the neck starts to form between adjacent particles and lasts until they grow to such a size that they start to impinge upon one another (Figures 1 and 2).[11] In this stage there is no grain growth and the total shrinkage, if present, is only a few percent. This is the most easily understood sintering stage. Many investigators[15,21-23] have developed models trying to identify the mechanism of matter transport, and to predict the rate of the major geometrical changes (neck

growth and specimen shrinkage) taking place during the process.[12] In general the neck growth and shrinkage may be represented by equations of the form:

$$(\frac{x}{r})^n = K_1 tr^{m-n} \qquad (2.5)$$

and

$$y = \frac{K_2{}^q t^q}{r^p} \qquad (2.6)$$

where x is the neck radius, r is particle radius, t is time, y is fractional shrinkage, K_1 and K_2 are temperature dependent constants, and m, n, p and q are constants which depend upon mechanisms.[11]

The values for the constants in equations 2.5 and 2.6 change from investigator to investigator depending on the assumptions made and on the geometry considered. In addition to this, in most instances the values of these constants are not independent of time as have been assumed. In spite of that, the identification of the mechanism of matter transport can be made by measuring both neck growth and shrinkage simultaneously, and comparing the experimental constants with the theoretical constants values. After doing that, in principle it should be possible to calculate the diffusion coefficients, at least theoretically for ideal systems. However,

in general the values found by sintering differ from those measured by tracer methods so should be used with care.[11]

2. <u>Intermediate Sintering Stage</u>. The intermediate region covers from neck impingement to that density at which the surface seals the interior off from the ambient atmosphere.[11] This stage is characterized by a system of interconnected pores which have complex geometry and for this reason it is difficult to find a reasonable model to represent it.[24] This stage is the most important for densification[11], since it is here that most of the densification occurs, up to about 93% of the theoretical density. This stage is characterized by grain growth and changing in pore geometry.

Coble[16-18] and Coble and Gupta[25] have presented models attempting to describe the intermediate stage of sintering. They have assumed that all grains have the same size and shape (cube, dodecahedron, or tetra-kaidecahedron) and that all pores are cylinders of the same size residing on the three-grain edges. They have also assumed that grain growth does not occur and that only one densification mechanisms prevails (either grain boundary or lattice diffusion). The resulting equations may be written in the form:

$$f(P) = \frac{K\gamma\Omega D}{G^m kT} (t_f - t) \qquad (2.7)$$

where P is porosity, f(P) is a function of the porosity, K and m are constants, D is the diffusion coefficient (equal to D_v for lattice diffusion and D_b for grain boundary diffusion mechanism), G the equivalent spherical grain diameter, t the time and t_f is the extrapolated time for disappearance of the pores.

Johnson[26] proposed a general model for the intermediate stage of sintering relating the densification rate to the instantaneous geometry in the compact. The advantage of his model is that no grain shape needs to be assumed and more than one mechanism can operate simultaneously. The resulting equation is:

$$\frac{1}{V} \cdot \frac{dV}{dt} = -\frac{8\gamma\Omega\bar{H}}{\bar{x}kT} (D_v \ S_v + b \ D_b \ L_v) \qquad (2.8)$$

where $\bar{H}$ is the average mean curvature obtainable by quantitative stereological techniques, $\bar{x}$ is proportional to the average grain size ($\bar{x}=\bar{G}/4$), S_v is the pore surface area/unit volume, L_v is the grain boundary-pore intersection perimeter/unit volume, V is the volume of element which is shrinking uniformly, and b is the width of the region of enhanced diffusion at the grain boundary.

Although Johnson's model is more general than Coble and Coble and Gupta's models, it is much more difficult to apply. Coble[17], trying to explain his data on

sintering of alumina compacts, incorporated in his initial equation the fact that grain growth occurred, and developed an equation which showed that the densification rate was predicted to change linearly with log time. However, Jorgensen[27] pointed out a mathematical error in his method. The fact is, however, that many experiments[12,17,25,28-34] have shown that the density increases linearly with the logarithm of sintering time at constant temperature. Many investigators[17,24,32,35,36] have, then, tried to develop models which could express this behavior. Coble[37] later concluded that the time dependence in the intermediate stage cannot be predicted precisely, even if grain growth is assumed.

3. **Final Sintering Stage**. The final stage of sintering starts when the continuous pore phase becomes discontinuous. The reason for distinguishing this stage from the intermediate stage is that the rate of the process may change.[11] The rate change to be expected cannot be predicted quantitatively, but it is assumed that the rate should decrease during the transition from one stage to the other. The reason for this unpredictable rate change behavior comes from the fact that many complications may appear in the process.[12]

In theory, if all pores remain on grain boundaries and the trapped gas can diffuse through the oxide to the surface, theoretical density may be achieved. The

densification rate then is either dependent upon the rate of gas diffusion to the surface or the diffusion rate of the slowest diffusing specie. If the gas is insoluble in the oxide and cannot escape to the surface, the pore will shrink until the gas pressure in the pore equals $2\gamma/r$, counter-balancing the driving force for sintering. It has been well established that pores which lie on or near a grain boundary always disappear more rapidly than pores far removed from grain-boundaries. These isolated pores may, in fact, increase in size during sintering, acting as vacancy sinks and competing with grain boundaries.[12] The average pore size may also increase through pore coalescence, depending on the relative rates of densification and grain growth.[26]

In spite of all these complications, Coble[17,18] has used his equation for the intermediate stage,

$$\frac{dP}{dt} = -N \frac{D\gamma\Omega}{G^3 kT} \tag{2.9}$$

to explain behavior in the final stage, by assuming that only the numerical constant N changes from one stage to the other. However, this equation has only a qualitative value.

4. <u>Grain Growth During Sintering</u>. Grain growth is a common phenomena taking place at high temperatures in most polycrystalline materials. The driving force for

grain growth is the excess free energy of the grain boundaries.[12] Grain growth takes place by the motion of grain boundaries towards their center of curvature in such a way to decrease the excess free energy.[11] In this process some grains disappear and the average size of the remaining grains increases.[14] Since the models for the later stages of sintering predict that the densification rate depends upon some power of the reciprocal of grain size (equations 2.7-2.9) it is clear that grain growth will cause the densification rate to decrease.[16]

Grain growth has been found to be the most important factor modifying the kinetics of sintering.[12] Grain growth changes the configuration of grain-boundaries relative to pores, causing an important effect on the sintering rate.[11] Since grain-boundaries play such an important role in the process, their mobility is of great importance in controlling the ultimate density of a specimen; the greatest densities are attained when the grain growth is inhibited.[14]

Grain growth is inhibited by the presence of pores and/or second phase inclusions which inhibit the migration of grain-boundaries. In the early stages of sintering, all pores lie on grain-boundaries, and the volume fraction of pores is so large that generally little grain growth occurs. As sintering proceeds, the volume fraction of pores gradually decreases until

finally the grain boundary starts to migrate and grain growth occurs. Under special conditions, there may be an exaggerated growth of the grains and many pores may become isolated within the grains, far removed from grain boundaries, and can disappear only very slowly. If this happens, the densification stops. Second phase inclusions may also inhibit grain boundary migration. As a result, continuous grain growth may also be stopped in the presence of dispersed second phase inclusions.[14]

III. LITERATURE REVIEW: THE MgO
REFRACTORY GRAIN

Magnesium oxide (periclase) has a cubic close-packed structure and is substantially ionic in bond character. The divalent Mg ion is very stable in this structure, so the MgO may be considered as a stoichiometric oxide. The Pauling ionic radii of Mg^{+2} and O^{-2} are 0.065 and 0.140 nm, and the lattice spacing for MgO is 0.420 nm. The formation of interstitial ions is not expected to be energetically feasible in this close-packed rock salt structure. Therefore, only Schottky type defects are expected to be found in pure MgO, and if impurities are present within the crystals, they will only occupy substitutional positions.[38]

In most cases the solubility of an impurity in MgO requires the substitution onto MgO lattice which is dependent on size and valence of both ions, chemical affinity, and also on similarity of crystal structures. If the impurity is insoluble within the MgO lattice, it will form a second phase around the MgO grains, which may be solid or liquid at the sintering temperature. A low temperature insoluble phase may show solubility at high temperatures, however it will probably segregate back to the second phase or to the grain boundaries on cooling, depending on the cooling rate.[13]

Aliovalent impurities may enhance vacancy concentrations, thereby having a large influence on diffusion of ions during the sintering process. This appears to be the case for MgO.[38] Due to the technological importance of magnesium oxide, the influence of impurities on sintering of MgO has been extensively studied.

A. SINTERING STUDIES ON MgO

The influence of the prior calcination of the raw materials ($MgCO_3$ and $Mg(OH)_2$) on grain densification at the final firing for the double-firing process, has received much study.[39-45] It has been shown that there is an optimum calcination temperature, in general between 800 to 1100°C, which leads to better densification in the final firing. The reduction of sinterability for higher calcination temperatures has been associated with the development of petrographically identifiable periclase crystals.[42]

Sintering of pure MgO system has been studied by Brown[33] at temperatures between 1300 and 1500°C, and more recently by Gupta[34] at temperatures between 1450 and 1650°C. They found, in both cases, a linear dependence of the densification rate with logarithm of time. Gupta found that this type of dependence was observed up to about 94% of the theoretical density, followed by marked lowering of densification rate for extended periods of

time. It was postulated that sintering was controlled
by the diffusion of Mg ions because the rate of the
process appeared to be related to the tracer measured
diffusion of Mg. However, since oxygen diffusion is
thought to be several orders of magnitude slower than
Mg diffusion, they proposed that enhanced oxygen diffusion
occurred along grain boundaries.

Due to the importance of MgO refractories, the
influence of impurities on sintering of MgO has been
extensively studied. As can be seen in Tables II and III
oxides of elements from nearly the entire periodic table
have been considered. Many impurities may improve
densification by going into solid solution with MgO
and creating either cation vacancies (TiO_2, ZrO_2, Mn
oxide and Fe oxide, and small additions of SiO_2 and
Al_2O_3) or anion vacancies (Li_2O), or by formation of a
liquid phase (Cu_2O and V_2O_5). On the other hand, many
impurities go into solid solution without altering
densification (NiO, CoO, and Fe oxide in reducing
atmosphere). Finally, many impurities may inhibit
densification either by formation of a second phase (for
example, Al_2O_3, SiO_2 and Fe oxides, over a certain
concentration) or by evaporation of the oxide (ZnO,
Cr_2O_3, and PbO).

TABLE II

INFLUENCE OF ADDITIVES ON SINTERING OF MgO; ELEMENT OXIDES OTHER THAN TRANSITION METAL OXIDES

Group	Oxide	Ionic** Radii(nm)	Sintering Temperature (°C)	Percent Addition (wt%)	Effect on Densification/Reason*	References
I A	Li_2O	Li^{+1} = 0.068	1210 to 1525	0.1 to 3.0	↑↑↑(conc. ≤ 0.4%)/V_O	46-49
	Na_2O	Na^{+1} = 0.097	1225 to 1525	0.1 to 6.0	↓↓/no solid solution; large ion	47-49
II A	CaO	Ca^{+2} = 0.099	1225 to 1800	0.1 to 10.0	→/no V_M, small solubility	47-51
	BaO	Ba^{+2} = 0.134	1225 and 1525	0.1 to 1.0	↓/no V_M, small solubility	48, 49
II B	ZnO	Zn^{+2} = 0.074	1400 and 1600	2.0 to 21.0	↑↑(T = 1400°C)/defective structure ↓↓(T = 1600°C)/volatility	47
	CdO	Cd^{+2} = 0.097	-	-	("Poor")/no solid solution	47
III A	Al_2O_3	Al^{+3} = 0.051	1225 to 1600	0.1 to 18.0	↑(conc. < 1.0%)/V_M ↓↓↓(high conc.)/spinel phase	47-50
IV A	SiO_2	Si^{+4} = 0.042	1225 to 1600	0.1 to 11.5	↑↑(conc. ≤ 1.0%, T < 1450°C)/V_M(?) (higher conc. or T > 1450°C)/Forsterite phase	47-50
	PbO	Pb^{+2} = 0.121	-	-	("Poor")/volatility, no solid solution	47

*↑, ↑↑, ↑↑↑ (small, high, very high increase); ↓, ↓↓, ↓↓↓ (small, high, very high decrease); → (no effect), V_M(cation vacancies), V_O(anion vacancies)

**Ionic radii (Mg^{+2} = 0.065nm, O^{-2} = 0.140nm)

TABLE III

INFLUENCE OF ADDITIVES ON SINTERING OF MgO; TRANSITION METAL OXIDES

Group	Oxide	Ionic Radii (nm)	Sintering Temperatures (°C)	Percent Addition (wt%)	Effect on Densification/Reason	References
I B	Cu_2O	$Cu^{+1} = 0.096$	–	–	↑↑(low T.) / liquid phase	47
IV B	TiO_2	$Ti^{+4} = 0.068$	900 to 1600	1.0 to 23.0	↑↑↑($T \geq 1300°C$; conc. $\leq 1.0\%$)/V_M	47, 50, 52, 55
	ZrO_2	$Zr^{+4} = 0.079$	900 to 1800	0.1 to 30.0	↑↑(conc. $\leq 2.0\%$)/V_M	47-49, 52, 55
V B	V_2O_5	$V^{+5} = 0.059$	1050 to 1600	0.1 to 3.0	↑↑↑($T \leq 1450°C$), →($T = 1600°C$/liquid phase	33, 48, 49, 55
	Ta_2O5	$Ta^{+5} = 0.068$	1225 and 1525	0.1 to 1.0	→/no explanation	48, 49
VI B	Cr_2O_3	$Cr^{+3} = 0.074$	1225 to 1600	0.1 to 25.0	↓↓↓(in air), →($P_{O_2} \leq 10^{-\epsilon}$ KPa)/Volatility	44, 47-49, 53, 54
	MoO_2	$Mo^{+4} = 0.070$	–	–	("Poor")/no solid solution	47
	WO_3	$W^{+6} = 0.062$	1225 and 1525	0.1 to 1.0	→/no solid solution	48, 49
VII B	"MnO"	$Mn^{+2} = 0.080$ $Mn^{+3} = 0.046$	1225 and 1525	0.1 to 1.0	↑↑↑/V_M	47-49
VIII	"FeO"	$Fe^{+2} = 0.075$ $Fe^{+3} = 0.064$	900 to 1600	0.1 to 25.0	↑↑(conc. $\leq 3.0\%$, in air)/V_M →(in H_2)/ no V_M	47-50, 52
	CoO	$Co^{+2} = 0.072$	–	–	→/no V_M	50
	NiO	$Ni^{+2} = 0.070$	1400 and 1600	1.0 to 22.0	→/no V_M	50

Investigations on MgO systems containing multi-component impurity phases usually present in the MgO refractory grain, have also been made. Spencer and Colemen[51] investigated the influence of 0.5 and 1.0 wt.% additions of forsterite, monticellite, merwinite, dicalcium silicate, and tricalcium silicate on sintering of MgO at temperatures ranging from 1400 to 1800°C. They found that each of the additions initially increased the densification of pure MgO at all temperatures. However, with sintering times longer than 360s these silicates inhibited the densification process especially at high temperatures. These effects were magnified with increased silicate content. Kriek et al.[50] also investigated the influence of 2.5 wt.% additions of dicalcium ferrite (C_2F) and brownmillerite (C_4AF) on sintering of MgO at temperatures between 1200 and 1500°C. These additions formed liquids and were very effective on densification at the lower temperatures, but became ineffective at the higher temperatures.

Water vapor is well known to have a positive influence on densification of MgO, particularly during the early stages of sintering. Investigations[56-59] in the temperature range 800 to 1200°C, with water vapor partial pressures between 10^{-5} to 87.1 KPa have shown that the water vapor increases the cation vacancy concentration at the surface and grain boundaries, thereby

increasing the grain-boundary diffusion and consequently the densification rate. The influence of gas entrapment (A) as a limiting factor to the final stage densification has also been studied at 1800°C.[60] The results have shown that an insoluble gas in the MgO lattice, in fact, does limit final densification.

B. SOLID PHASE RELATIONSHIPS IN THE MgO GRAIN

The most important impurities of the MgO grain are Ca and Si oxides. Their importance derives from the fact that the CaO/SiO_2 molar ratio determines which silicate phases will be present in equilibrium with MgO. This is illustrated by the compatibility triangles in the phase diagram $MgO-CaO-SiO_2$ (Figure 3). These phases will be: MgO, M_2S, and CMS for C/S molar ratio lower than 1.0; MgO, CMS, and C_3MS_2 for C/S ratio between 1.0 and 1.5; MgO, C_3MS_2, and C_2S for C/S ratio between 1.5 and 2.0; MgO, C_2S, and C_3S for C.S ratio between 2.0 and 3.0; and finally MgO, C_3S, and CaO for C/S ratio higher than 3.0. The mineral names for these phases are periclase for MgO, forsterite for M_2S, monticellite for CMS, merwinite for C_3MS_2, dicalcium silicate for C_2S, and tricalcium silicate for C_3S, where we have used the notation C for CaO, M for MgO and S for SiO_2.

Many investigations have considered the influence of impurities on the properties of MgO. White[6]
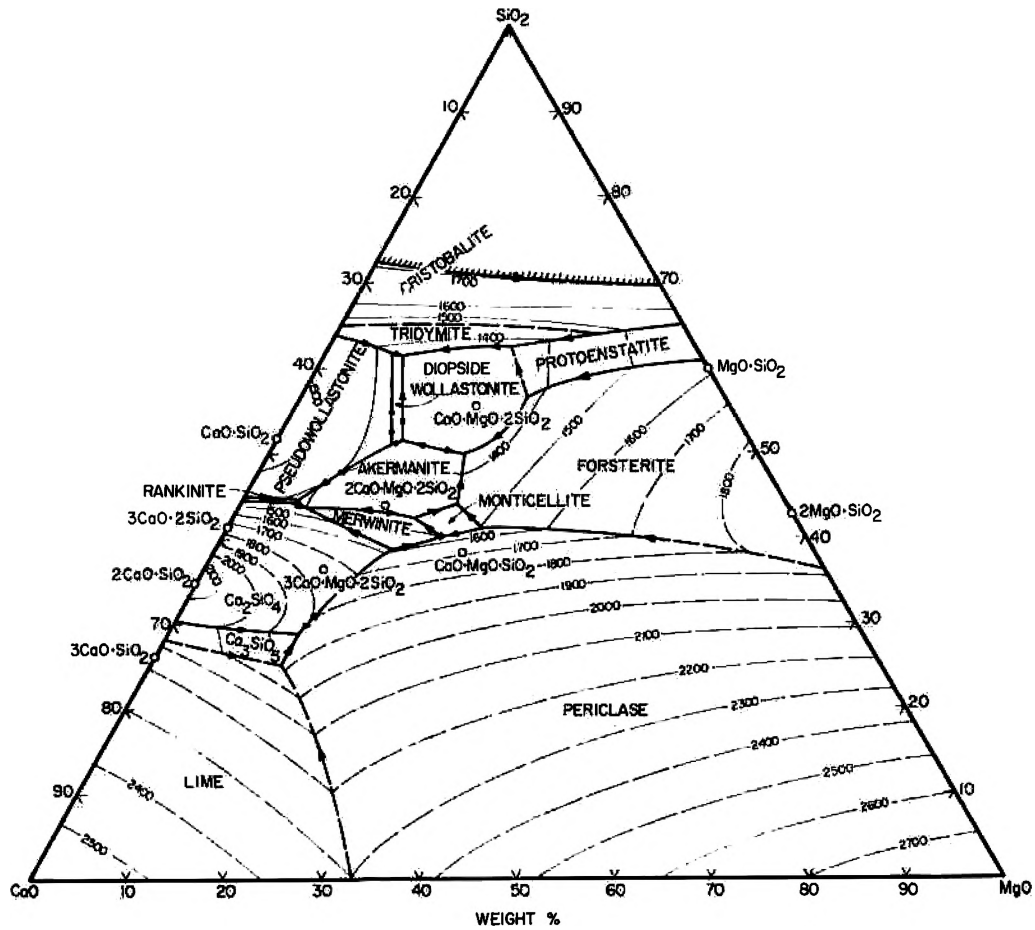
Figure 3. Phase diagram for the system $CaO-MgO-SiO_2$ (after
Osborn and Muan[101], based on work of Ferguson
and Merwin, and of Greig).

particularly has made a great contribution to the under-standing of these systems. He has developed what is called the "Diagram of White" to predict the phases that will be present in the MgO grain, when the type and concentration of the impurities are known. He has worked with CaO, SiO_2, FeO, Fe_2O_3, Al_2O_3, Cr_2O_3 and B_2O_3 as impurities. Since the number of components involved in the system is very high, his diagram is based on combinations of mutually compatible phases which coexist within various composition ranges.

The purest Brazilian natural magnesite (Table I) which has been used in this investigation has Al_2O_3, Cr_2O_3 and B_2O_3 in small enough concentrations to not be considered as variables in our analysis. Therefore, only CaO, SiO_2, Fe and Mn oxides will be considered as impurities for this MgO grain. The foundation of the understanding of the Brazilian MgO grain chemistry is based on the elucidation by White[6] of the solid-phase assemblages in the system $MgO-CaO-SiO_2-FeO-Fe_2O_3$, in which magnesiowustite (MgO containing FeO and other oxides in solid solution) occurs as a separate phase. He determined that because of the prevalence of solid isomorphous replacement, particularly in the spinel and magnesiowustite phases, the principal features of the phase relationships involved can be understood from the solid-phase relationships in the corresponding part of

the system $CaO-MgO-Fe_2O_3-SiO_2$, which is shown in Figure 4. Starting with a mixture of MgO, M_2S and MF ($MgO.Fe_2O_3$) and adding CaO to it (i.e. moving from left to right through the composition tetrahedron), the composition will pass in turn through the phase assemblages, as shown in Table IV. Between these four-phase assemblages, three-phase assemblages, corresponding to the phases separating the tetrahedra, will, of course, occur.

White[6] has emphasized the importance of the CaO/SiO_2 ratio in the MgO system. When the molar ratio is 2.0, the composition lies on the phase assemblage $MgO-MF-C_2S$. When it is less than 2.0 all the Fe_2O_3 occurs in combination with MgO as spinel. When the ratio is greater than 2.0, all or part of the Fe_2O_3 occurs in combination with CaO. The "Diagram of White" has proved useful in predicting the equilibrium phase assemblage to be expected in actual refractories as a function of composition. However, it is now known that at high temperatures there is an appreciable solid solubility between some of the phases, and the limiting CaO/SiO_2 ratios indicated in Table IV are no longer precise.

Doman et al.[61] have shown that the solubility of CaO in MgO, for the pure system CaO-MgO, increases from approximately 0.9 wt.% at 1600^OC to 7 wt.% at 2370^OC. Jones and Melford[5] have found that CaO as C_2S is soluble
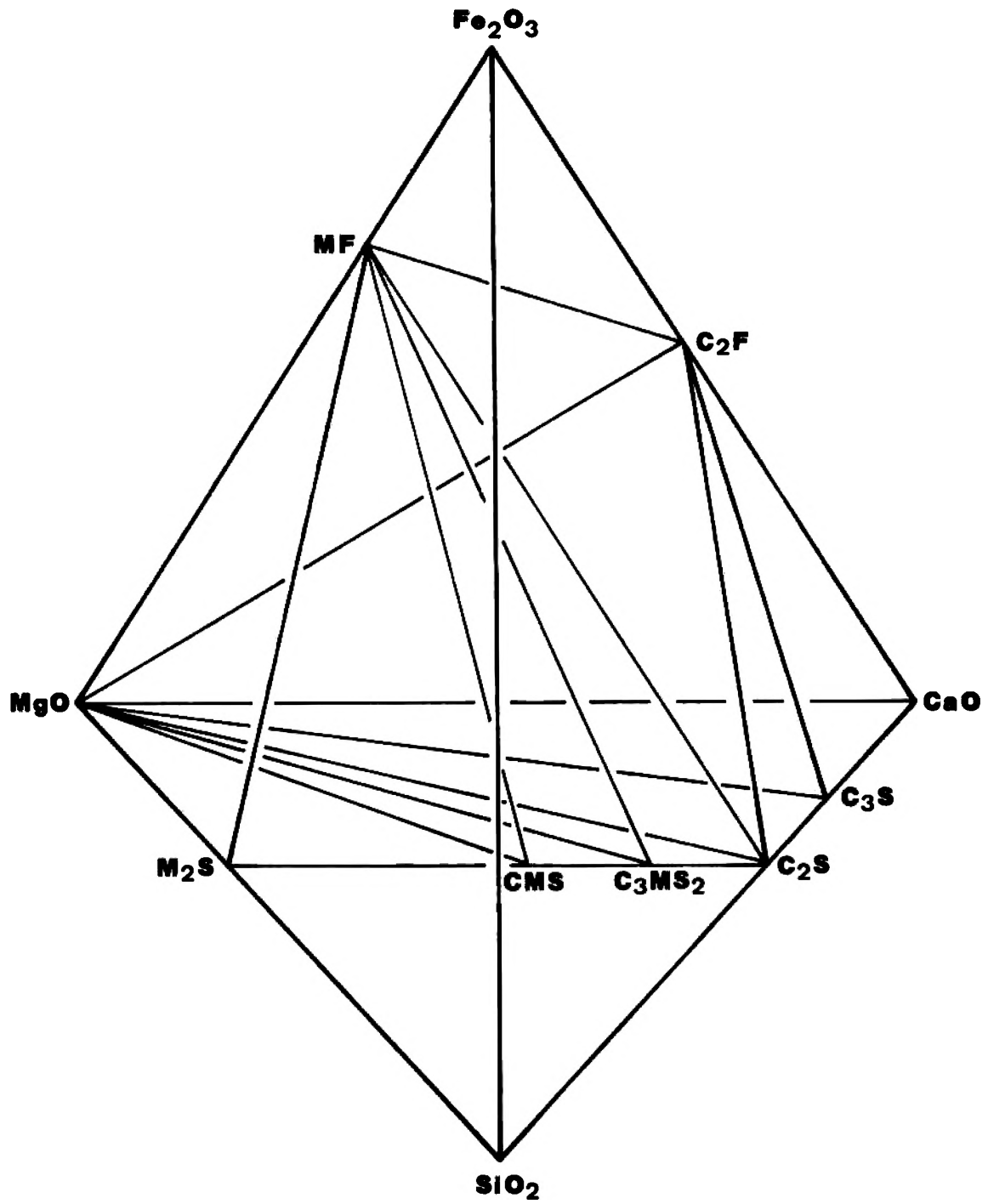
Figure 4. Phase relationships in the solid state in the system CaO-MgO-SiO$_2$-Fe$_2$O$_3$ (after White[6]).

TABLE IV

SOLID PHASE COMBINATIONS IN THE SYSTEM MgO-CaO-SiO_2-FeO-Fe_2O_3 (AFTER WHITE[6])

$\begin{bmatrix} MgO \\ FeO \end{bmatrix}$	$\begin{bmatrix} MgO \\ FeO \end{bmatrix}$	$\begin{bmatrix} MgO \\ FeO \end{bmatrix}$	$\begin{bmatrix} MgO \\ FeO \end{bmatrix}$	$\begin{bmatrix} MgO \\ FeO \end{bmatrix}$	$\begin{bmatrix} MgO \\ FeO \end{bmatrix}$
MF	MF	MF	MF	C_2F	C_2F
$\begin{bmatrix} M_2S \\ F'_2S \end{bmatrix}$	CMS	C_3MS_2	C_2F	C_2S	C_3S
CMS	C_3MS_2	C_2S	C_2S	C_2S	CaO
(1)	(2)	(3)	(4)	(5)	(6)

*Ceramic Notation: $M=MgO$, $C=CaO$, $S=SiO_2$, $F'=FeO$, $F=Fe_2O_3$

Brackets indicate that a single solid solution phase is formed.
CaO/SiO_2 molar ratio increasing from left to right.

in MgO to a level of about 0.5 wt.% at 1700°C. Upon
slow cooling, the CaO comes out of solution and enters
the bonding phase. This behavior will cause an appreciable
decrease in the CaO/SiO$_2$ ratio in the bond at service
temperatures for low SiO$_2$ content magnesites. As it is
shown in Figure 3, the decrease in the CaO/SiO$_2$ ratio
lead to the formation of silicates with lower
refractoriness, thereby lowering maximum service
temperatures.

Henney and Jones[62] have shown in the pure system
MgO-CaO that CaO is soluble up to about 1.9 wt.% at
1750°C. They have also shown that the solubility of
CaO when silicate was present increased with increasing
CaO content in the silicate. For example, with CMS
present no detectable solubility was observed. But with
C$_3$MS$_2$ present, slight solubility was detected which
reduced the CaO/SiO$_2$ molar ratio in the silicate to
about 1.4, and with C$_2$S present, the solubility was higher
and depended initially on the amount of C$_2$S present.
They pointed out, however, that these results are
strictly true only for pure MgO-CaO-SiO$_2$ compositions
and that in commercially available materials the presence
of other oxides, e.g. Al$_2$O$_3$, Fe$_2$O$_3$ could apparently
reduce the solid solubility of CaO in MgO. Spencer
et al.[63], in a similar work, have found that at constant
SiO$_2$ content the degree of solid solubility of CaO in the

periclase phase at 1800°C, generally rose as the CaO/ SiO_2 ratio of the silicate increased. It is also known from the phase diagram $MgO-SiO_2$ that there is no appreciable solubility of SiO_2 in MgO.[64]

Hatfield et al.[65] have investigated the effect of high temperature solution of CaO in MgO on the melting behavior of the silicate phase as function of SiO_2 content. For compositions low in SiO_2, they found a considerable effect. They have also discussed the importance of the presence of a second solid phase at high temperature in the prevention of penetration of slag between the MgO grains in magnesite refractories. In the absence of special additions, a second solid phase could be maintained at working temperatures either by keeping the CaO/SiO_2 ratio low enough to produce a silicate phase that is predominantly forsterite, or high enough to produce dicalcium silicate. They have shown that a second solid phase made up with forsterite is worse than that with dicalcium silicate. This is because in steelmaking practice lime pick-up by the refractory occurs in service, increasing the CaO/SiO_2 ratio. Although forsterite persists up to 1900°C in the absence of CaO, the temperature of the MgO-forsterite-liquid boundary falls rapidly when CaO is present. Dicalcium silicate is the alternative used in practice since it avoids this problem. In this case, the maximum temperature to which

the solid silicate persists is 1800°C but to retain solid dicalcium silicate up to this temperature, CaO/ SiO_2 molar ratios considerably higher than 2 are required in magnesites of low silica content. Hall and Spencer[2], however, discussed that the main disadvangages of having CaO/SiO_2 ratio very high are that the hydration resistance and the refractory resistance to slags containing high Fe_2O_3 contents will decrease. In fact, the presence of small Fe_2O_3 content lowers the refractoriness of the silicate phase particularly at high CaO/SiO_2 ratios.

Henney and Jones[66] have shown that at 1500°C, MgO grains containing small amounts of forsterite (M_2S) and dicalcium silicate (C_2S) had the same M.O.R. They have also shown that the hot mechanical strength was very dependent on the CaO/SiO_2 ratio and reached a minimum around a ratio of 1/1. The presence of liquid even in very small proportions lowered the strength markedly. Spencer[1] has also shown the effect of chemical purity on the hot mechanical strength of the magnesia grain. He has found that CaO/SiO_2 molar ratios greater than 2 are required to maximize high temperature mechanical strength and that the lower the SiO_2 content the greater the CaO/SiO_2 ratio required to maximize it. The results are consistent with the established fact the part of the CaO enters into solid solution in the periclase

phase resulting in a lower CaO/SiO_2 ratio in the silicate phase than in the overall composition.

Due to the strong influence of the CaO/SiO_2 ratio on properties, for this study the ratio will be held at a constant value of two. According to the "Diagram of White" (Figure 3 and Table IV), we can expect to have our MgO grain between phase assemblages no. 3 and 4, where the phases in equilibrium will be: magnesiowustite, spinel ($MgO.Fe_2O_3$) and dicalcium silicate. Manganese oxides have not been considered in any previous work in relation to these phase assemblages. However, Mn oxides are predicted to behave like Fe oxides in these MgO systems.

C. SYSTEMS CONTAINING IRON AND MANGANESE OXIDES IN THE MgO GRAIN

Iron and Mn oxides are very important constituents of MgO refractories either because they are present as impurities in the refractory, or because they are present in the slags which contact the refractory during its industrial use.[67] Iron and Mn oxides may go into solid solution with MgO in the periclase-type structure ($MgO.FeO$ and $MgO.MnO$) or may form the spinel-type structure ($MgO.Fe_2O_3$ and $MgO.Mn_2O_3$). If they are associated with the silicate phases around the MgO crystals, these oxides would form different phases depending on the type of silicate present.

1. <u>Solid Solutions in the Periclase-Type Structure</u>
<u>and Spinel-Type Structure</u>. Magnesium oxide forms solid
solution with oxides of divalent Fe and Mn. In these
binaries there is complete mutual solubility between the
end members. The phase diagrams of these systems are
characterized by continuously sloping solidus and
liquidus curves from the MgO end member toward the
transition metal oxide, as shown in Figures 5a[68,69] and
6a[70,71].

The MgO."FeO" solid solution is not strictly binary,
because an appreciable part of Fe is present in the
trivalent state even when the system is in contact with
metallic Fe.[67] Figure 5b[72] shows phase relations in
MgO-Fe oxide mixtures in air. As we can see, Fe_2O_3
is partially soluble in MgO at high temperatures. In
this system, loss of oxygen occurs at high temperatures
to an extent that depends on the oxygen pressure, so that
the magnesiowustite formed contains both Fe^{2+} and Fe^{3+}
cations. The solubility of the spinel phase in the
magnesiowustite lattice increases with rising temperature
but is very low below $1000^{\circ}C$.[67]

In the representation of the phase assemblages in
Figure 4 and Table IV, White[6] assumed that Fe oxide
would be present both as FeO and Fe_2O_3, which, as was
pointed out in discussing the solubility of Fe oxide in
MgO, is to be expected at high temperatures. Partial
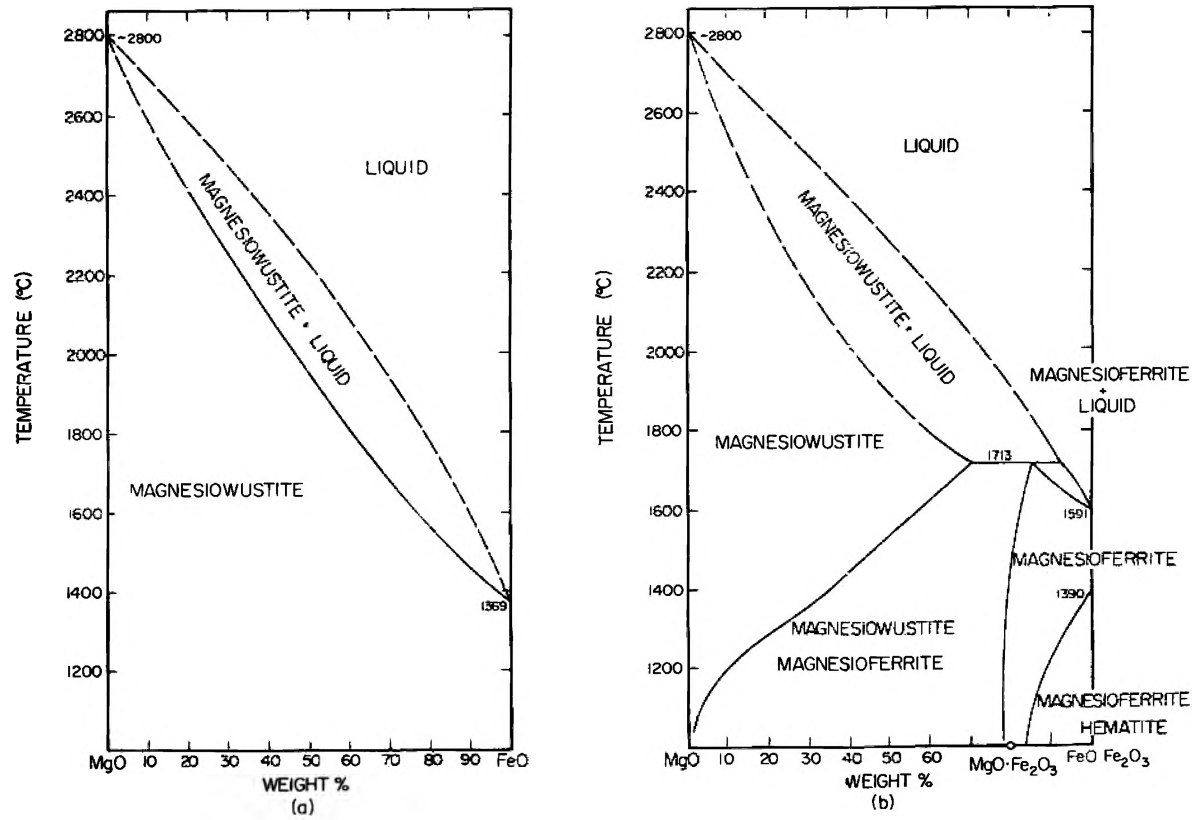
Figure 5. Phase diagram for the system MgO-Fe oxides (a) in contact
with metallic Fe[68,69] and (b) in air[72] (ex. Muan and
Osborn[101]).
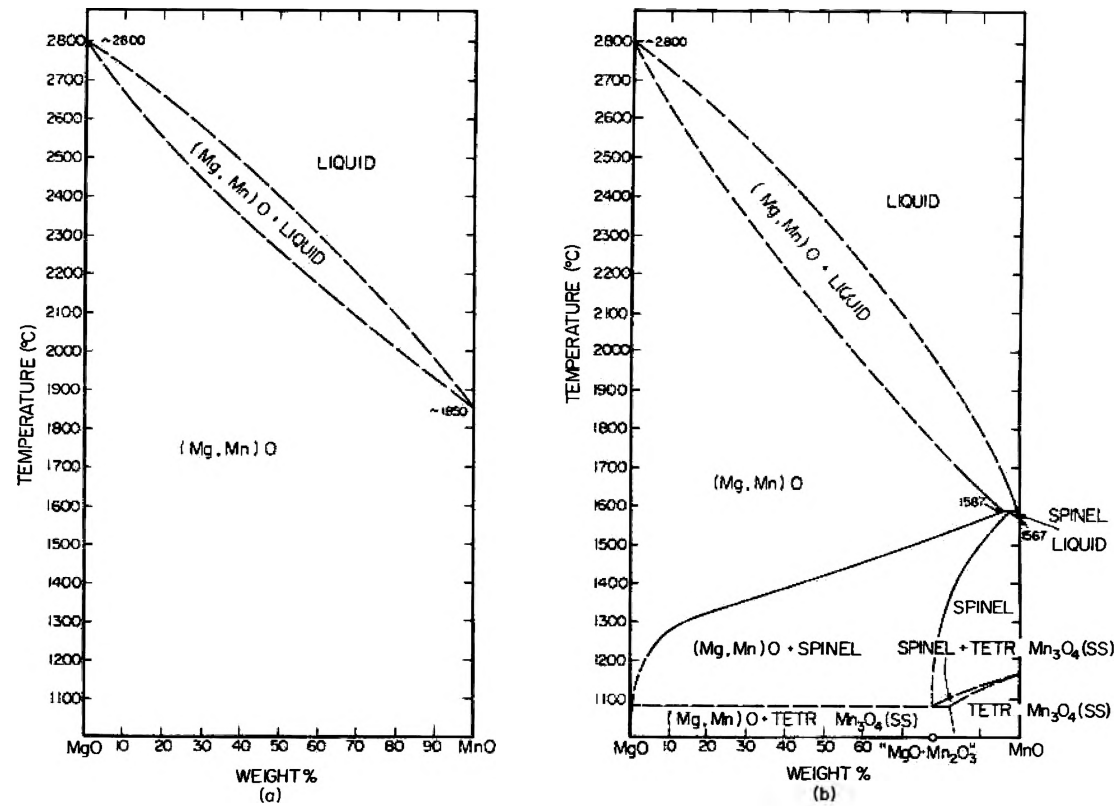
Figure 6.   Phase diagram for the system MgO-Mn oxides (a) at the low oxygen pressure prevailing at the maximum melting point of MnO, and (b) in air (after Riboud and Muan[73], ex. Muan and Osborn[101]).

isomorphous replacement of MgO by FeO (or more precisely, of Mg^{2+} by Fe^{2+}), will then occur in the magnesio-wustite phase, the spinel phase and the silicates, as is indicated in Table IV. Hence, in certain phase assemblages, FeO will occur in two or even three phases, and it is not possible to predict how it will be distributed between them.[6]

The phase assemblages, of course, give no indication of the way in which the state of oxidation of the iron will vary with temperature and furnace atmosphere. Changes in the Fe_2O_3/FeO ratio will influence the distribution of Fe oxide over the various phases. A decrease in the ratio will usually result in a decrease in the proportion of Fe oxide occurring in the spinel phase and, consequently, a decrease in the amount of spinel with an accompanying increase in the proportion occurring in the magnesio-wustite and the silicates. It can also cause phase changes to occur during heating and cooling.[6]

The diagram MgO-Mn oxide in air (Figure 6b) shows that the MgO-MnO solid solution is stable over a very large temperature and composition range.[73] Comparison of the diagrams MgO-Fe oxides (Figure 5) and MgO-Mn oxides (Figure 6) leads us to the conclusion that Mn oxides will behave like Fe oxides in MgO systems. It can be predicted from these diagrams that MgO refractories would

be resistant to attack by Mn oxide, since it is well-
known that MgO refractories are quite resistant to
attack by slags rich in Fe oxides.

2. Silicate Phases Containing Fe and Mn Oxides
as Components. Iron oxides in combination with CaO
behave quite differently than the analagous MgO-Fe
oxide systems. The size difference between the cations
is sufficiently large in the system CaO-FeO[64] so that
there is incomplete solubility between the end members.
Phillips and Muan[74] have studied the system CaO-Fe
Oxide-SiO_2 in air and they have shown that Fe oxide is
a strong fluxing agent for the phases C_2S, C_3S, and
CaO which are usually present in MgO refractories.

As we have discussed before, when the CaO/SiO_2
molar ratio in the MgO grain is 2.0, the phases in
equilibrium will be MgO (Magnesio-Wustite)-MF-C_2S.
When the CaO/SiO_2 molar ratio is less than 2.0, the
Fe_2O_3 occurs in combination with MgO as spinel. When the
ratio is greater than 2.0, all or part of the Fe_2O_3
occurs in combination with CaO.[6] In the latter case,
the Fe_2O_3 will form a calcium ferrite phase which has a
strong fluxing effect for the high CaO/SiO_2 ratio phases
(C/S > 2).[74] However, the ability of Fe to enter into
solid solution in the MgO phase as FeO at high tempera-
tures reduces the effective concentration of Fe_2O_3
present in the silicate phase thereby reducing the

fluxing action. This is the reason why Fe_2O_3 contents up to a certain concentration has little effect on decreasing the mechanical strength of MgO at high temperature. Spencer[1] has reported that on an equivalent weight basis, B_2O_3 is approximately 10 times more deleterious than Al_2O_3, which in turn is 6 times more deleterious than Cr_2O_3 and 17 times more deleterious than Fe_2O_3 to the modulus of rupture strength at $1500^{\circ}C$ for a particular MgO composition.

The system CaO-MnO has been studied by Schenck et al.[71] who have shown that there is a complete mutual solubility between the end members, which is a different behavior than that observed for the similar CaO-FeO system. Riboud and Muan[73] have shown that for the system CaO-Mn oxide in air, Mn oxide can go into solid solution with CaO up to a concentration of about 17% at temperature of $1588^{\circ}C$. On the other hand, the similar binary CaO-Fe oxides in air[64] shows practically no solid solubility of Fe oxide in CaO. Although the system $CaO-SiO_2$-Mn oxides in air is not known, it is known in conditions of reducing atmosphere which was studied by Glasser.[75] He has shown that MnO can go into solid solution with CaO over an extensive region in the ternary diagram, a behavior also completely different from the similar FeO system.

With respect to the other silicates present in the MgO grain when the CaO/SiO_2 molar ratio is less than 2.0, Muan[67] mentioned that for the case of the orthosilicate of magnesium (forsterite), there is a complete solid solution with Mn and Fe oxides, where the cations Mn^{2+} and Fe^{2+} are incorporated by substitution into the forsterite lattice. Snow[76], in a previous work, mentioned that Mn^{2+} and Fe^{2+} have practically no solid solution with the other silicates (monticellite and merwinite) occurring in magnesite refractories.

IV. EXPERIMENTAL PROCEDURE

A. RAW MATERIALS

The MgO used in this investigation was provided by the company MAGNESITA SA of Brazil. It was prepared by calcination of the purest Brazilian natural magnesite (see Table I - "M30") in a Herreshoff type of furnace at temperatures between 800 and $1000^{\circ}C$. The influence of the calcination of the magnesite on densification during the final firing has been previously studied so it has not been included in this work. The intent of this study was to investigate the effect of Mn oxide (compositions ranging from 0.16% to 2.50 wt.% MnO) on the sintering properties of the Brazilian natural magnesite. To simplify the study, the CaO/SiO molar ratio was maintained at a constant value of 2:1.

The chemical analysis for the MgO as received from MAGNESITA SA is shown in Table V. As the CaO/SiO_2 molar ratio of this calcined MgO was lower than two, so the ratio had to be corrected by addition of $CaCO_3$. The MnO addition was made at six different composition levels ranging from 0.16 to 2.50 wt.% MnO by mixing appropriate amounts of $MnCO_3$. The chemical analysis for these six compositions, identified as A(0.16% MnO), B(0.50% MnO), C(1.00% MnO), D(1.50% MnO), E(2.00% MnO), and F(2.50% MnO),

TABLE V

CHEMICAL ANALYSIS FOR ALL COMPOSITIONS USED DURING THE INVESTIGATION

Chemical Analysis (wt%)	As Received	A	B	C	D	E	F
MgO	98.48	98.31	98.01	97.56	96.94	96.48	95.92
SiO_2	0.32	0.33	0.35	0.29	0.33	0.34	0.31
CaO	0.52	0.66	0.62	0.61	0.65	0.59	0.60
Fe_2O_3	0.43	0.45	0.43	0.43	0.43	0.41	0.43
MnO	0.16	0.16	0.50	1.03	1.56	2.10	2.65
Al_2O_3	0.07	0.07	0.06	0.06	0.07	0.06	0.06
TiO_2	0.02	0.02	0.03	0.02	0.02	0.02	0.03
Cr_2O_3	0.00	0.00	0.00	0.00	0.00	0.00	0.00
C/S calcul.	–	1.87	1.87	1.87	1.87	1.87	1.87
C/S exper.	–	2.00	1.77	2.10	1.97	1.74	1.94
MnO calc.	–	0.16	0.50	1.00	1.50	2.00	2.50
MnO exper.	–	0.16	0.50	1.03	1.56	2.10	2.65

are shown in Table V. The chemical analysis of $CaCO_3$
and $MnCO_3$ used are shown in Appendix A.

B. SAMPLE PREPARATION

The calcined MgO as received from MAGNESITA SA was
first characterized with respect to particle size
distribution. The results for a wet-sieve analysis
were:

Sieves	Percentages
> 0.210 mm	4%
< 0.105 mm	76%
< 0.062 mm	60%
< 0.044 mm	55%

Two methods for mixing the MgO powders with $CaCO_3$
and $MnCO_3$ were tried. In the first one, the magnesium
oxide was mixed with water for form a thick slurry;
$CaCO_3$ and $MnCO_3$ were then dissolved in acid and then
added to the slurry, with the resulting solution being
agitated by a magnetic stirrer for about 1200s. Since
the solution of MgO in water has a basic pH, a precipita-
tion of $Mn(OH)_2$ and $Ca(OH)_2$ over the MgO particles
should be expected, since these hydroxides have a very
low solubility in water. Chemical analysis of samples
taken in different points of the suspension showed a
very good distribution for Mn. However, Ca was poorly
distributed. Further chemical analysis showed that a
dry mixing method gave better homogeneity so this method
was used.

Each sample (from A to F) was calcined in an electric furnace for 3,600s at 800°C. This process decomposed the carbonates, and removed possible water adsorbed by the MgO particles after the calcination in Brazil. The calcined powder was removed from the furnace while still warm, and placed in beakers inside a desiccator to minimize hydration that would result in loss of powder reactivity. The chemical analyses shown in Table V were made after this step.

C.   SINTERING PROCEDURE

The sintering experiments were made using the samples prepared as described above. Twelve grams of each composition were poured into a high speed blender and mixed for 600s. A solution of polyethylene glycol in water (0.01 Kg/100 ml water) was added to the powder at a level of 5 wt.% as a binder. Finally, pellets 12.8 mm diameter by approximately 5.5 mm height (0.0015 Kg each), were pressed at 530 MPa, yielding green densities in the range of 56 to 59% of the theoretical density. To avoid hydration, the pressed pellets were then immediately placed in the furnace for firing. Pellets stored for one day after pressing showed a small decrease in bulk density after firing and so have not been included in this analysis.

Two different samples, containing six specimens each, were fired each time. The specimens were placed on MgO setters of the same composition, in two different levels inside the furnace. A Mo-wound resistor type of furnace having an Al_2O_3 - tube chamber was used. The determination of the hot zone was made by a Pt-Pt 10% Rh thermocouple at $1650^{\circ}C$ and showed a gradient of $\pm 2^{\circ}C$.

As discussed previously, the heating rate influences the densification process. Therefore, the heating rate was controlled manually at 1,800s intervals, and it was approximately constant throughout the investigation following schedules shown in Figure 7. The pellets were sintered for times ranging from 3.6 to 57.6 Ks at either $1700^{\circ}C$ or $1760^{\circ}C$. Time of 57.6 Ks was also used for temperatures of 1520, 1580, and $1640^{\circ}C$. The furnace temperature was controlled electronically within approximately $\pm 5^{\circ}C$. The actual temperature was determined by an optical pyrometer. Samples were cooled in about 28.8 Ks and then stored in hermetically sealed containers.

Two different atmospheres were used in the investigation: air and an atmosphere of partial pressure of oxygen of 10^{-7} KPa. This partial pressure of oxygen was controlled by using a buffer system which consisted of a mixture of CO_2 and forming gas $(N_2 + H_2)$. A solid electrolyte constituted by a solid solution of
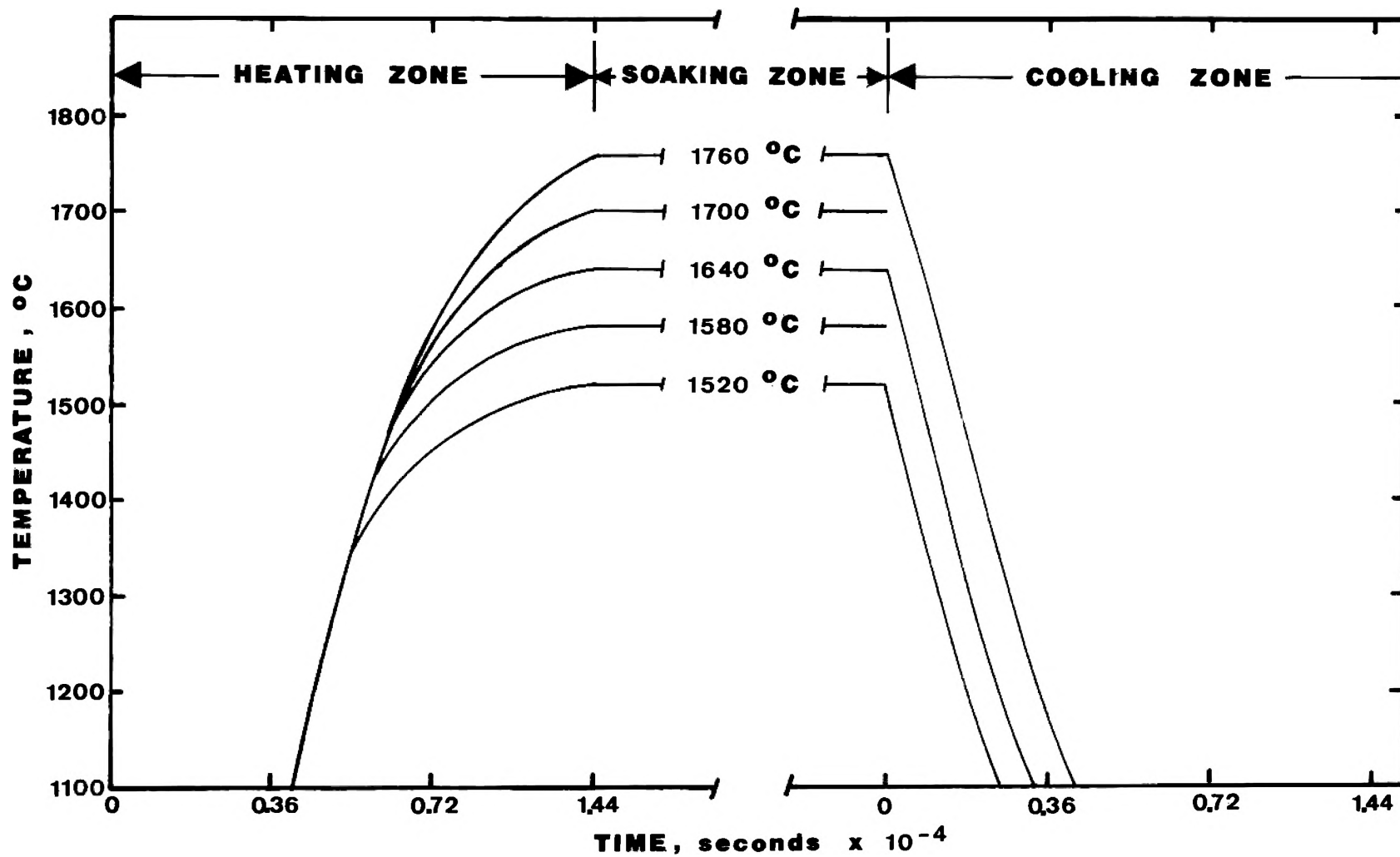
Figure 7. Heating curves for the sintering experiments.

ZrO_2 - 15 wt.% CaO was used as the oxygen sensor. The EMF calculations for using the oxygen sensor are included in Appendix B.

D.   SAMPLE EVALUATION

Shrinkage was measured on each fired pellet with a micrometer. The units fired in reducing atmosphere showed deformation and weight loss which made it difficult to measure shrinkage accurately. This effect was independent of composition. Therefore, shrinkage measurements were not used to follow the sintering process.

Bulk density and apparent porosity were measured following approximately the general procedure as described by the standard C830-79 from ASTM.[77] At the beginning the measurements were being made for each pellet. However, due to the small sample weight the precision of the results was poor. Therefore, six pellets for each composition were measured at the same time. This was repeated four times for each set of specimens and the results were shown to be very reproducible. Tables VI to XIV list the results for compositions A to F, fired in different temperatures, different times, and different atmospheres.

As can be seen in Tables VI to XIV, the data on bulk densities are also reported in terms of the percentage of theoretical density of MgO. This

theoretical density has been considered as 3,576 Kg/m^3 throughout the calculations. This value has not been corrected for the addition of any second phases. Also included in these tables are the percentage total porosity and the percentage closed pores. The first was calculated according to:

$$\% \text{ Total Porosity} = 100 - \% \text{ Theoretical Density} \quad (4.1)$$

The percentage of closed pores was calculated according to the relation:

$$\% \text{ Closed Pores} = (1-(\% \text{ Apparent Porosity}/ \% \text{ Total Porosity})) \times 100 \quad (4.2)$$

The color differences in the fired units are probably a good indication of the ionization state of impurities. All samples fired in the reducing atmosphere were white, showing that Mn and Fe were in the valence state plus two. The samples fired in air had color varying from light brown for sample A containing 0.16 wt.% MnO to chocolate brown for sample F containing 2.50 wt.% MnO, which suggests an increasing presence of Mn^{+3} and Fe^{+3}.

The influence of MnO doping on sintering of MgO was determined by plotting percent theoretical density against MnO content as function of sintering conditions (Figures 8 to 11). The influence of time on sintering of MgO was determined by plotting percent theoretical

density versus logarithm of time (Figures 15 to 20) for different compositions, temperatures, and atmospheres. The influence of temperature on densification of the MgO was determined by plotting percent theoretical density versus sintering temperature, for different compositions and atmospheres, at a constant soaking time of 57.6 Ks (Figures 21 to 26).

Samples for microstructure studies were taken for each composition fired at $1760^{\circ}C$ for 57.6 Ks in both air and reducing atmosphere. The polished sections were prepared by grinding on 240, 320, 400 and 600 grit SiC paper followed by polishing with 5 um and 0.3 μm Al_2O_3 powder. Samples to be examined by optical microscope were then etched by using either distilled water, a 5 wt.% aqueous solution of NH_4Cl or a 10% (by volume) aqueous solution of HCl, following procedure given by Snow.[76] Samples to be examined by the electron micro-probe were polished following the same procedure above. Then they were covered with a thin layer of carbon, by vapor deposition, to produce a conductive surface.

The "random intercept" method of Fullman[78] was used to determine the main grain diameter D. For random straight lines drawn across a section of a microstructure composed of equal spherical grains, he showed that:

$$D = 1.5L \tag{4.3}$$

where L is the average length of the intercepts of individual grains on the lines. This method is considered valid if the range of grain size is not too wide.

V.   RESULTS AND DISCUSSION

A.   SINTERING RESULTS

The results obtained in this investigation are shown in Tables VI (composition A; MnO = 0.16 wt.%), VII (composition B, MnO = 0.50 wt.%), VIII (composition C; MnO = 1.00 wt.%), IX (composition D; MnO - 1.50 wt.%), X (composition E; MnO = 2.00 wt.%), and XI (composition F; MnO = 2.50 wt.%). For each composition, the results are shown as a function of time (3,600 to 57,600s), temperature (1700°C and 1760°C), and atmosphere (air and $P_{O_2} = 10^{-7}$ KPa).

A more complete study of the influence of temperature on densification is shown in Tables XII (compositions A and B), XIII (compositions C and D), and XIV (compositions E and F). For each composition the results are shown as functions of temperature (1520°C to 1760°C) and atmosphere (air and $P_{O_2} = 10^{-7}$ KPa), for a constant time of sintering.

1.   Influence of MnO Concentration. Figures 8 to 11 show data on percent theoretical density plotted versus MnO concentration ranging from 0.16 wt.% to 2.50 wt.%. Figures 8 and 9 include data for samples fired in air at 1700 and 1760°C, respectively. Figures 10 and 11 include data for samples fired in an atmosphere of $P_{O_2} = 10^{-7}$ KPa at 1700 and 1760°C, respectively. For

TABLE VI

DENSITY AND POROSITY DATA VERSUS TIME OF SINTERING
FOR COMPOSITION A(MnO = 0.16 wt.%)

Temperature; Atmosphere	Time s x 10^{-4}	Bulk Density (Kg/m^3) x 10^{-3}	% ρ/ρ_T	% Total Porosity	% Apparent Porosity	% Closed Pores
1700°C; Air	0.36	3.13 ± 0.01	87.5	12.5	10.0	20
	0.72	3.17 ± 0.01	88.6	11.4	7.9	31
	1.44	3.19 ± 0.01	89.2	10.8	3.3	69
	2.88	3.22 ± 0.01	90.0	10.0	0.9	91
	5.76	3.24 ± 0.01	90.6	9.4	0.7	93
1760°C; Air	0.36	3.18 ± 0.02	88.9	11.1	6.1	45
	0.72	3.21 ± 0.01	89.8	10.2	3.1	70
	1.44	3.24 ± 0.01	90.6	9.4	0.9	90
	2.88	3.26 ± 0.01	91.2	8.8	0.8	91
	5.76	3.29 ± 0.01	92.0	8.0	0.6	93
1700°C; P_{O_2} = 10^{-7} KPa	0.36	3.10 ± 0.02	86.7	13.3	9.7	27
	0.72	3.12 ± 0.01	87.2	12.8	6.7	48
	1.44	3.12 ± 0.01	87.2	12.8	5.3	59
	2.88	3.15 ± 0.01	88.1	11.9	2.0	83
	5.76	3.17 ± 0.02	88.6	11.4	1.1	90
1760°C; P_{O_2} = 10^{-7} KPa	0.36	3.11 ± 0.01	87.0	13.0	9.0	31
	0.72	3.12 ± 0.01	87.2	12.8	5.7	55
	1.44	3.15 ± 0.01	88.1	11.9	1.5	87
	2.88	3.18 ± 0.01	88.9	11.1	1.3	88
	5.76	3.19 ± 0.01	89.2	10.8	1.0	91

TABLE VII

DENSITY AND POROSITY DATA VERSUS TIME OF SINTERING
FOR COMPOSITION B (MnO = 0.50 wt.%)

Temperature; Atmosphere	Time $s \times 10^{-4}$	Bulk Density $(Kg/m^3) \times 10^{-3}$	% ρ/ρ_T	% Total Porosity	% Apparent Porosity	% Closed Pores
1700°C; Air	0.36	3.14 ± 0.01	87.8	12.2	9.4	23
	0.72	3.16 ± 0.01	88.4	11.6	8.2	29
	1.44	3.18 ± 0.01	88.9	11.1	2.8	75
	2.88	3.22 ± 0.01	90.0	10.0	0.8	92
	5.76	3.25 ± 0.01	90.9	9.1	0.7	94
1760°C; Air	0.36	3.20 ± 0.01	89.5	10.5	3.8	64
	0.72	3.23 ± 0.01	90.3	9.7	1.0	90
	1.44	3.26 ± 0.01	91.2	8.8	0.8	91
	2.88	3.28 ± 0.01	91.7	8.3	0.9	89
	5.76	3.30 ± 0.01	92.3	7.7	0.6	92
1700°C; $P_{O_2} = 10^{-7}$ KPa	0.36	3.09 ± 0.01	86.4	13.6	12.8	6
	0.72	3.12 ± 0.02	87.2	12.8	9.6	25
	1.44	3.13 ± 0.01	87.5	12.5	8.7	30
	2.88	3.15 ± 0.01	88.1	11.9	1.7	86
	5.76	3.17 ± 0.02	88.6	11.4	1.1	90
1760°C; $P_{O_2} = 10^{-7}$ KPa	0.36	3.12 ± 0.01	87.2	12.8	9.5	26
	0.72	3.13 ± 0.01	87.5	12.5	5.3	58
	1.44	3.15 ± 0.01	88.1	11.9	2.8	76
	2.88	3.17 ± 0.01	88.6	11.4	1.4	88
	5.76	3.19 ± 0.01	89.2	10.8	0.9	87

TABLE VIII

DENSITY AND POROSITY DATA VERSUS TIME OF SINTERING
FOR COMPOSITION C(MnO = 1.00 wt.%)

Temperature; Atmosphere	Time s x 10^{-4}	Bulk Density (Kg/m^3) x 10^{-3}	% ρ/ρ_T	% Total Porosity	% Apparent Porosity	% Closed Pores
1700°C; Air	0.36	3.16 ± 0.01	88.4	11.6	8.2	29
	0.72	3.18 ± 0.01	88.9	11.1	6.1	45
	1.44	3.21 ± 0.01	89.8	10.2	1.8	82
	2.88	3.24 ± 0.01	90.6	9.4	0.8	91
	0.76	3.26 ± 0.01	91.2	8.8	0.9	90
1760°C; Air	0.36	3.21 ± 0.01	89.8	10.2	5.7	44
	0.72	3.24 ± 0.01	90.6	9.4	1.7	82
	1.44	3.27 ± 0.02	91.4	8.6	0.8	91
	2.88	3.29 ± 0.01	92.0	8.0	0.8	90
	5.36	3.30 ± 0.01	92.3	7.7	0.5	94
1700°C; P$_{O_2}$ = 10^{-7} KPa	0.36	3.10 ± 0.01	86.7	13.3	11.1	17
	0.72	3.12 ± 0.01	87.2	12.8	7.5	41
	1.44	3.14 ± 0.01	87.8	12.2	6.5	47
	2.88	3.16 ± 0.02	88.4	11.6	1.2	90
	5.76	3.17 ± 0.01	88.6	11.4	1.1	90
1760°C; P$_{O_2}$ = 10^{-7} KPa	0.36	3.11 ± 0.01	87.0	13.0	9.3	28
	0.72	3.13 ± 0.01	87.5	12.5	5.8	54
	1.44	3.15 ± 0.02	88.1	11.9	2.3	81
	2.88	3.18 ± 0.01	88.9	11.1	1.6	86
	5.76	3.20 ± 0.01	89.5	10.5	1.2	89

TABLE IX

DENSITY AND POROSITY DATA VERSUS TIME OF SINTERING
FOR COMPOSITION D(MnO = 1.50 wt.%)

Temperature; Atmosphere	Time $s \times 10^{-4}$	Bulk Density $(Kg/m^3) \times 10^{-3}$	% ρ/ρ_T	% Total Porosity	% Apparent Porosity	% Closed Pores
1700°C; Air	0.36	3.18 ± 0.01	88.9	11.1	6.7	43
	0.72	3.20 ± 0.01	89.5	10.5	2.4	77
	1.44	3.24 ± 0.01	90.6	9.4	1.4	85
	2.88	3.25 ± 0.01	90.9	9.1	0.8	91
	5.76	3.27 ± 0.02	91.4	8.6	0.7	92
1760°C; Air	0.36	3.24 ± 0.01	90.6	9.4	2.1	78
	0.72	3.25 ± 0.01	90.9	9.1	1.2	87
	1.44	3.28 ± 0.01	91.7	8.3	0.7	92
	2.88	3.30 ± 0.01	92.3	7.7	1.0	87
	5.76	3.32 ± 0.02	92.8	7.2	0.7	90
1700°C; $P_{O_2} = 10^{-7}$ KPa	0.36	3.11 ± 0.01	87.0	13.0	11.6	11
	0.72	3.13 ± 0.01	87.5	12.5	8.6	31
	1.44	3.13 ± 0.01	87.5	12.5	4.3	66
	2.88	3.16 ± 0.01	88.4	11.6	2.3	80
	5.76	3.18 ± 0.01	88.9	11.1	1.3	88
1760°C; $P_{O_2} = 10^{-7}$ KPa	0.36	3.12 ± 0.01	87.2	12.8	8.8	31
	0.72	3.14 ± 0.01	87.8	12.2	6.4	48
	1.44	3.16 ± 0.01	88.4	11.6	3.3	72
	2.88	3.18 ± 0.01	88.9	11.1	1.5	86
	5.76	3.20 ± 0.02	89.5	10.5	1.0	90

TABLE X

DENSITY AND POROSITY DATA VERSUS TIME OF SINTERING
FOR COMPOSITION E(MnO = 2.00 wt.%)

Temperature; Atmosphere	Time s x 10^{-4}	Bulk Density (Kg/m^3) x 10^{-3}	% ρ/ρ_T	% Total Porosity	% Apparent Porosity	% Closed Pores
1700°C; Air	0.36	3.19 ± 0.01	89.2	10.8	6.9	36
	0.72	3.22 ± 0.01	90.0	10.0	4.0	60
	1.44	3.25 ± 0.01	90.9	9.1	2.0	78
	2.88	3.27 ± 0.02	91.4	8.6	0.7	92
	5.76	3.28 ± 0.01	91.7	8.3	0.7	92
1760°C; Air	0.36	3.25 ± 0.01	90.9	9.1	2.5	73
	0.72	3.27 ± 0.01	91.4	8.6	1.2	86
	1.44	3.30 ± 0.01	92.3	7.7	0.8	90
	2.88	3.31 ± 0.01	92.6	7.4	0.7	91
	5.76	3.32 ± 0.01	92.8	7.2	0.7	90
1700°C; $P_{O_2} = 10^{-7}$ KPa	0.36	3.10 ± 0.01	86.7	13.3	12.4	7
	0.72	3.12 ± 0.01	87.2	12.8	8.4	34
	1.44	3.13 ± 0.01	87.5	12.5	5.5	56
	2.88	3.15 ± 0.01	88.1	11.9	2.3	81
	5.76	3.18 ± 0.01	88.9	11.1	1.7	85
1760°C; $P_{O_2} = 10^{-7}$ KPa	0.36	3.11 ± 0.01	87.0	13.0	10.7	18
	0.72	3.14 ± 0.02	87.8	12.2	8.4	31
	1.44	3.16 ± 0.02	88.4	11.6	1.8	84
	2.88	3.18 ± 0.02	88.9	11.1	1.6	86
	5.76	3.19 ± 0.01	89.2	10.8	1.3	88

TABLE XI

DENSITY AND POROSITY DATA VERSUS TIME OF SINTERING
FOR COMPOSITION F (MnO = 2.50 wt.%)

Temperature; Atmosphere	Time $s \times 10^{-4}$	Bulk Density $(Kg/m^3) \times 10^{-3}$	% ρ/ρ_T	% Total Porosity	% Apparent Porosity	% Closed Pores
1700°C; Air	0.36	3.20 ± 0.01	89.5	10.5	8.1	23
	0.72	3.23 ± 0.01	90.3	9.7	1.9	80
	1.44	3.27 ± 0.01	91.4	8.6	1.1	87
	2.88	3.28 ± 0.01	91.7	8.3	0.8	90
	5.76	3.30 ± 0.02	92.3	7.7	0.7	91
1760°C; Air	0.36	3.26 ± 0.01	91.2	8.8	1.8	80
	0.72	3.29 ± 0.01	92.0	8.0	0.8	90
	1.44	3.30 ± 0.01	92.3	7.7	0.7	91
	2.88	3.32 ± 0.01	92.8	7.2	0.7	90
	5.76	3.34 ± 0.02	93.4	6.6	0.8	88
1700°C; $P_{O_2} = 10^{-7}$ KPa	0.36	3.11 ± 0.01	87.0	13.0	12.0	8
	0.72	3.12 ± 0.01	87.2	12.8	10.6	17
	1.44	3.14 ± 0.01	87.8	12.2	6.2	49
	2.88	3.15 ± 0.01	88.1	11.9	1.9	94
	5.76	3.18 ± 0.01	88.9	11.1	1.6	86
1760°C; $P_{O_2} = 10^{-7}$ KPa	0.36	3.12 ± 0.02	87.2	12.8	10.0	22
	0.72	3.13 ± 0.02	87.5	12.5	6.3	50
	1.44	3.16 ± 0.01	88.4	11.6	3.5	70
	2.88	3.18 ± 0.01	88.9	11.1	1.8	84
	5.76	3.20 ± 0.01	89.5	10.5	1.1	90

TABLE XII

DENSITY AND POROSITY DATA VERSUS TEMPERATURE OF SINTERING
(time = 57,600 s) FOR COMPOSITIONS A AND B

Composition; Atmosphere	Temperature ($^{\circ}$C)	Bulk Density (Kg/m^3) x 10^{-3}	% ρ/ρ_T	% Total Porosity	% Apparent Porosity	% Closed Pores
A; Air	1520	3.15 ± 0.01	88.1	11.9	9.1	24
	1580	3.19 ± 0.01	89.2	10.8	5.6	48
	1640	3.21 ± 0.01	89.8	10.2	2.3	77
	1700	3.24 ± 0.01	90.6	9.4	0.7	93
	1760	3.29 ± 0.01	92.0	8.0	0.6	93
A; $P_{O_2} = 10^{-7}$ KPa	1520	3.16 ± 0.01	88.4	11.6	9.4	19
	1580	3.16 ± 0.01	88.4	11.6	5.3	54
	1640	3.20 ± 0.01	89.5	10.5	2.0	81
	1700	3.17 ± 0.02	88.6	11.4	1.1	90
	1760	3.19 ± 0.01	89.2	10.8	1.0	91
B; Air	1520	3.16 ± 0.02	88.4	11.6	8.7	25
	1580	3.19 ± 0.01	89.2	10.8	6.4	41
	1640	3.22 ± 0.02	90.0	10.0	2.5	75
	1700	3.25 ± 0.01	90.9	9.1	0.7	94
	1760	3.30 ± 0.01	92.3	7.7	0.6	92
B; $P_{O_2} = 10^{-7}$ KPa	1520	3.16 ± 0.01	88.4	11.6	8.0	31
	1580	3.18 ± 0.01	88.9	11.1	4.4	60
	1640	3.19 ± 0.01	89.2	10.8	1.7	84
	1700	3.17 ± 0.02	88.6	11.4	1.1	90
	1760	3.19 ± 0.01	89.2	10.8	0.9	87

TABLE XIII

DENSITY AND POROSITY DATA VERSUS TEMPERATURE OF SINTERING
(time = 57,600 s) FOR COMPOSITIONS C AND D

Composition; Atmosphere	Temperature (^{O}C)	Bulk Density (Kg/m^3) x 10^{-3}	% ρ/ρ_T	% Total Porosity	% Apparent Porosity	% Closed Pores
C; Air	1520	3.17 ± 0.01	88.6	11.4	9.3	18
	1580	3.19 ± 0.01	89.2	10.8	5.6	48
	1640	3.23 ± 0.01	90.3	9.7	3.6	63
	1700	3.26 ± 0.01	91.2	8.8	0.9	90
	1760	3.30 ± 0.01	92.3	7.7	0.5	94
C; $P_{O_2} = 10^{-7}$ KPa	1520	3.16 ± 0.01	88.4	11.6	10.1	13
	1580	3.18 ± 0.01	88.9	11.1	6.7	40
	1640	3.19 ± 0.01	89.2	10.8	2.0	81
	1700	3.17 ± 0.01	88.6	11.4	1.1	90
	1760	3.20 ± 0.01	89.5	10.5	1.2	89
D; Air	1520	3.19 ± 0.01	89.2	10.8	8.6	20
	1580	3.20 ± 0.01	89.5	10.5	5.8	45
	1640	3.23 ± 0.01	90.3	9.7	1.7	82
	1700	3.27 ± 0.02	91.4	8.6	0.7	92
	1760	3.31 ± 0.02	92.6	7.4	0.7	91
D; $P_{O_2} = 10^{-7}$ KPa	1520	3.18 ± 0.01	88.9	11.1	8.7	22
	1580	3.18 ± 0.01	88.9	11.1	4.3	61
	1640	3.20 ± 0.01	89.5	10.5	2.9	72
	1700	3.18 ± 0.01	88.9	11.1	1.3	88
	1760	3.20 ± 0.02	89.5	10.5	1.0	90

TABLE XIV

DENSITY AND POROSITY DATA VERSUS TEMPERATURE OF SINTERING
(time = 57,600 s) FOR COMPOSITIONS E AND F

| Composition; Atmosphere	Temperature (°C)	Bulk Density (Kg/m³) x 10⁻³	% ρ/ρ_T	% Total Porosity	% Apparent Porosity	% Closed Pores
E; Air	1520	3.19 ± 0.01	89.2	10.8	8.5	21
	1580	3.22 ± 0.01	90.0	10.0	5.0	50
	1640	3.25 ± 0.01	90.9	9.1	1.8	80
	1700	3.28 ± 0.01	91.7	8.3	0.7	92
	1760	3.32 ± 0.01	92.8	7.2	0.7	90
E; P_{O_2} = 10⁻⁷ KPa	1520	3.17 ± 0.01	88.6	11.4	9.2	19
	1580	3.19 ± 0.01	89.2	10.8	7.3	32
	1640	3.21 ± 0.01	89.8	10.2	2.1	79
	1700	3.18 ± 0.01	88.9	11.1	1.7	85
	1760	3.19 ± 0.01	89.2	10.8	1.3	88
F; Air	1520	3.20 ± 0.02	89.5	10.5	8.7	17
	1580	3.23 ± 0.01	90.3	9.7	5.9	39
	1640	3.26 ± 0.01	91.2	8.8	1.3	85
	1700	3.30 ± 0.02	92.3	7.7	0.7	91
	1760	3.34 ± 0.02	93.4	6.6	0.8	88
F; P_{O_2} = 10⁻⁷ KPa	1520	3.18 ± 0.01	88.9	11.1	9.5	14
	1580	3.18 ± 0.01	88.9	11.1	5.8	48
	1640	3.20 ± 0.01	89.5	10.5	2.6	75
	1700	3.18 ± 0.01	88.9	11.5	1.6	86
	1760	3.20 ± 0.01	89.5	10.5	1.1	90
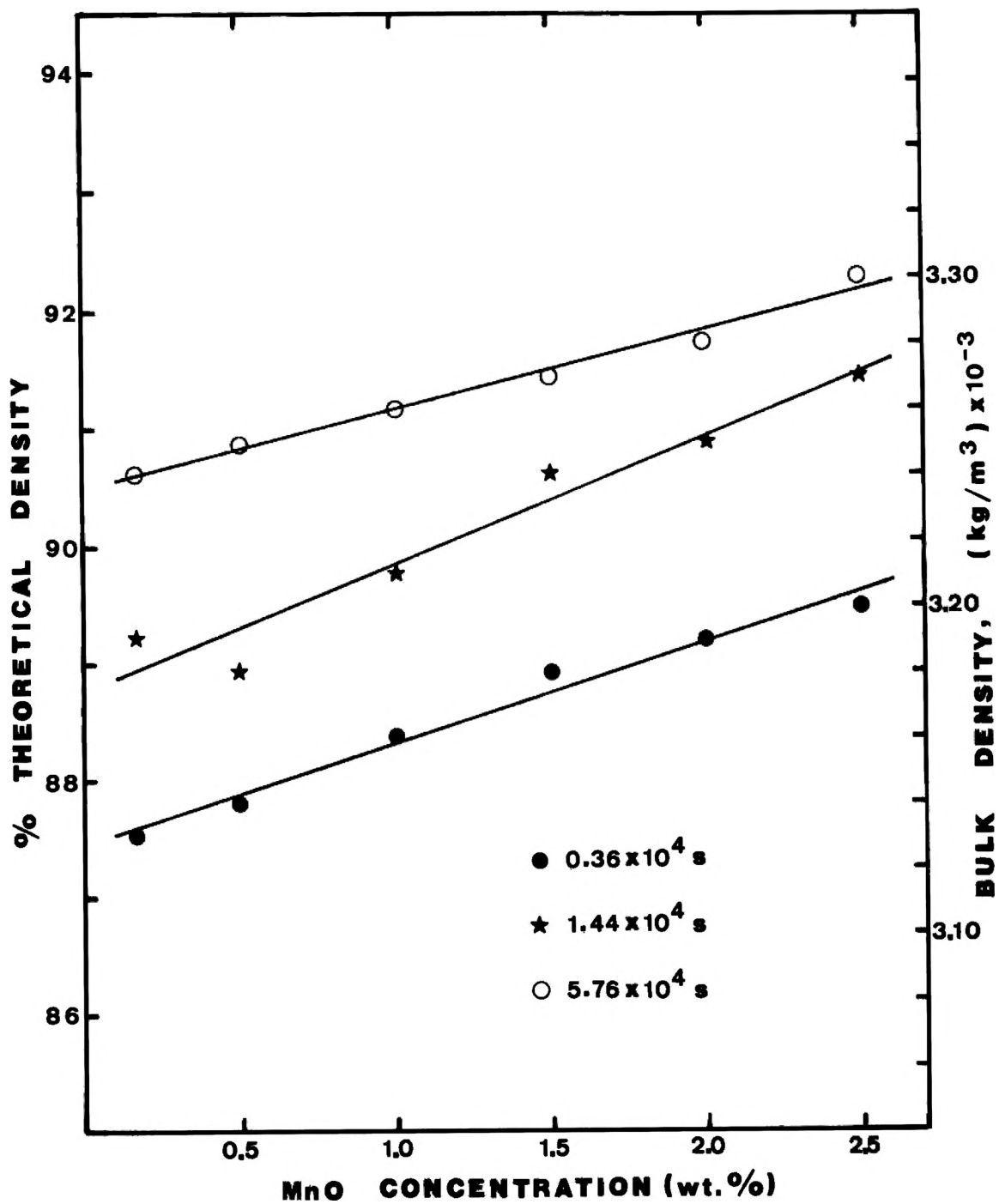
Figure 8.   Percent theoretical density versus MnO concentration
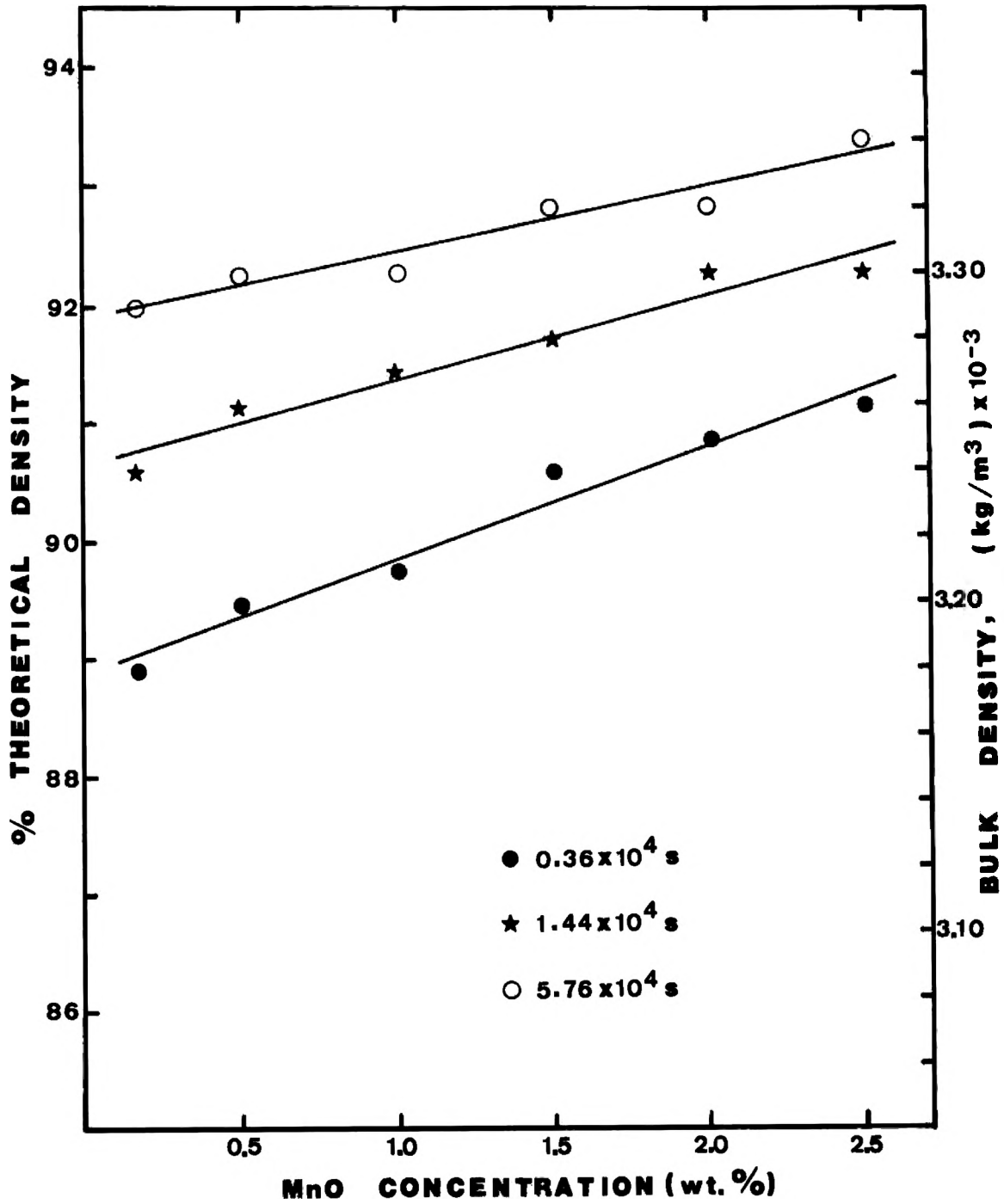   for samples fired in air at 1700°C.

Figure 9.   Percent theoretical density versus MnO concentration
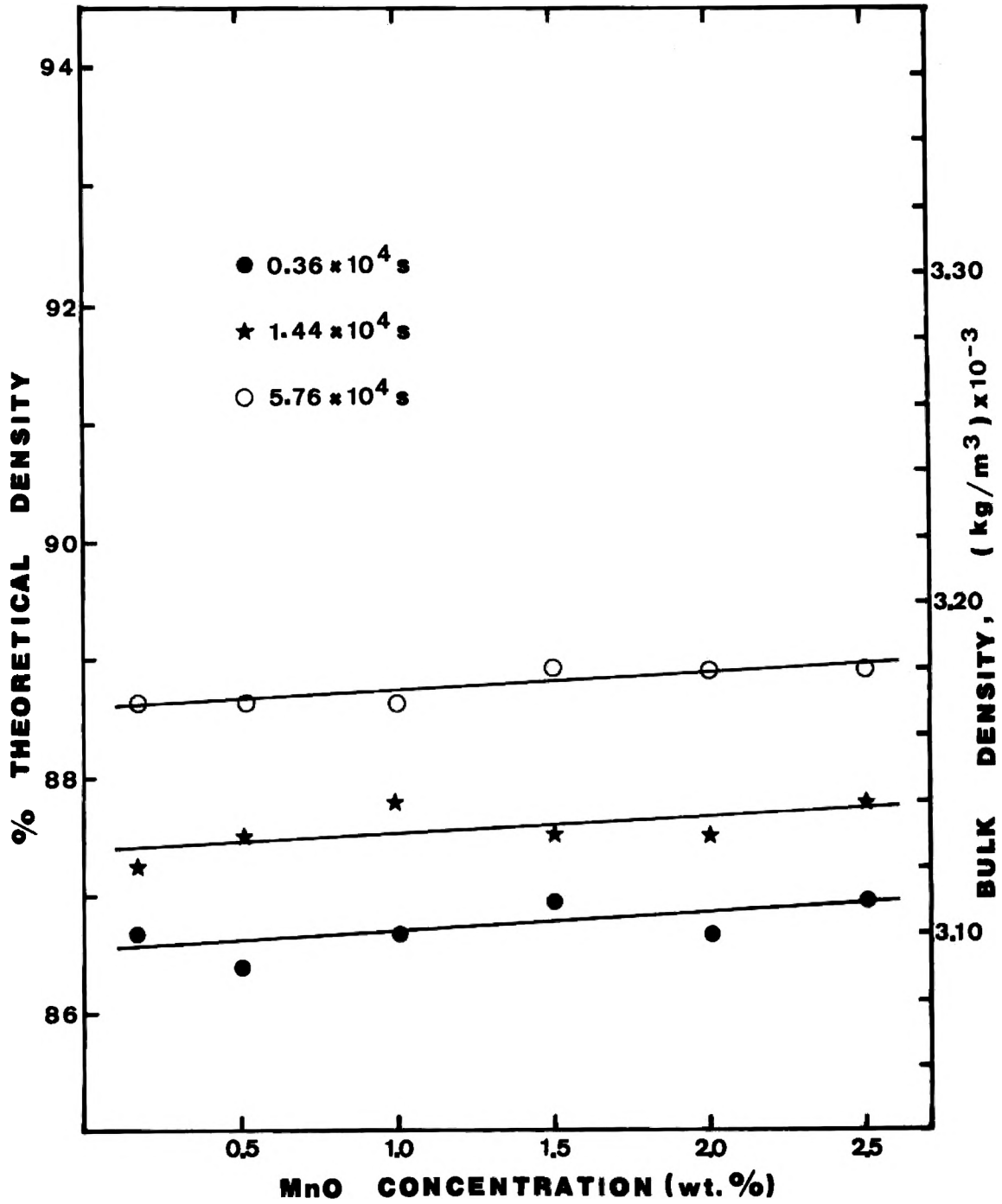for samples fired in air at 1760°C.

Figure 10. Percent theoretical density versus MnO concentration for samples fired in $P_{O_2} = 10^{-7}$ KPa at 1700°C.
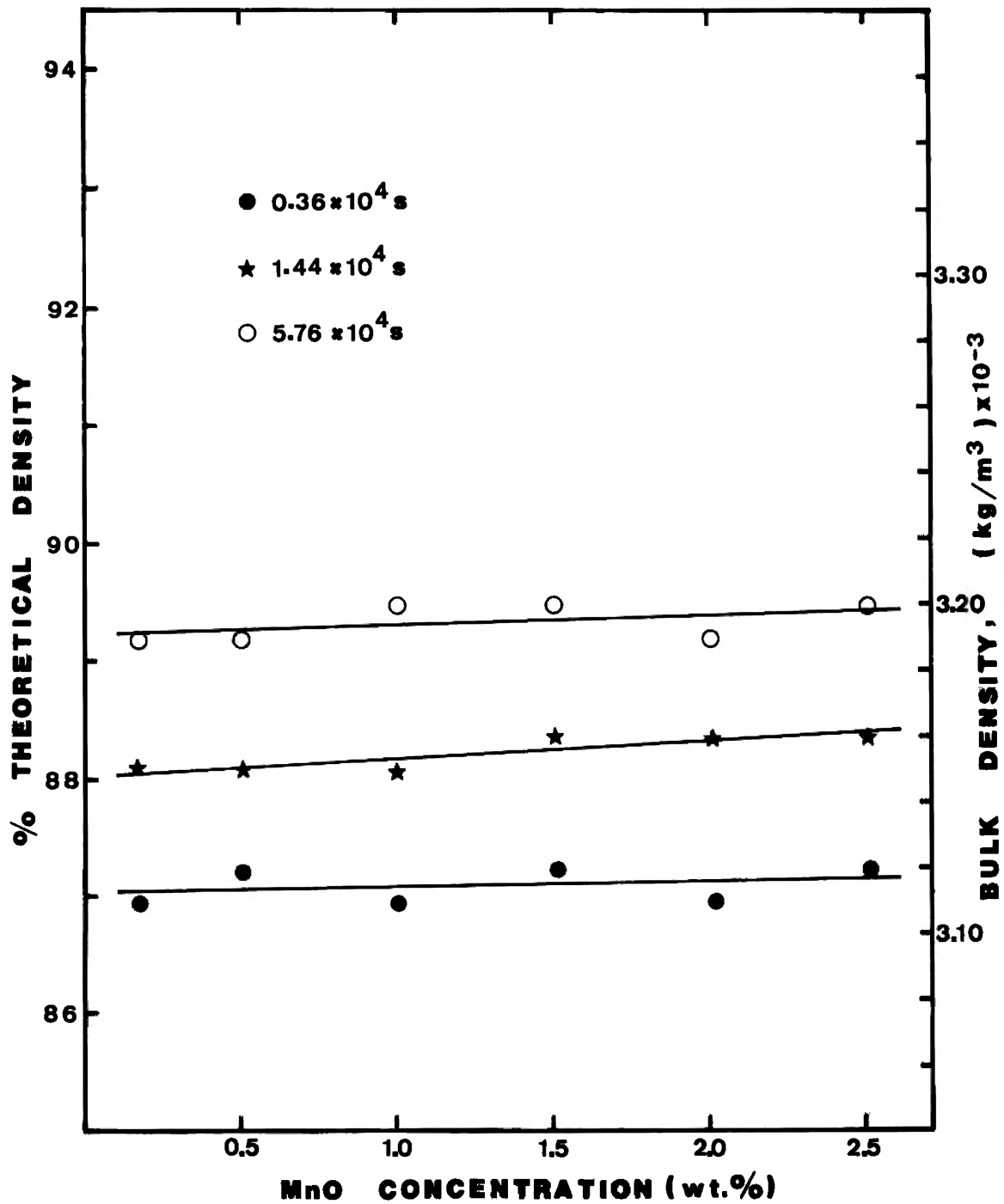
Figure 11.   Percent theoretical density versus MnO concentration
for samples fired in $P_{O_2} = 10^{-7}$ KPa at 1760°C.

the purpose of clarity, only the curves for time of sintering of 3.6, 14.4, and 57.6 Ks are shown, leaving out the data for 7.2 and 28.8 Ks.

A striking difference can be seen between the results obtained for firing in air and reducing atmosphere. For air, there is a positive influence of the MnO content on densification. However, in reducing atmosphere, the densification process is not influenced by the MnO doping.

These results were also observed by Jones et al.[52] in an investigation of the influence of Fe oxides on sintering of MgO at temperatures from 900 to 1500°C under different atmosphere of oxygen and hydrogen. They found that Fe oxide has a positive influence on densification of MgO when fired under an atmosphere of oxygen, but no effect was observed for the samples fired in hydrogen (reducing atmosphere). They interpreted that the atmosphere changes the number of cation vacancies in the MgO lattice due to a valence change of the Fe ion. With reducing atmosphere, practically all the Fe ion is divalent, going into solid solution with MgO without creating lattice defects thereby not altering the densification behavior. Under oxidizing conditions, the fraction of trivalent ions present promoted sintering by the formation of cation vacancies. Nelson and Cutler[47] had predicted this behavior for Fe oxides and also for Mn oxides.

In contrast to the stability of MgO, Mn exhibits a large stoichiometric variation in its oxides. Davies and Richardson[79] have measured the deviation from stoichiometry of MnO with oxygen pressure. They found that while FeO is always metal deficient, the stoichiometric compound MnO is obtained at low pressures. As has been seen, MnO forms a complete solid solution with MgO (Figure 6a). On the other hand, the "binary" diagram MgO-Mn oxides in air (Figure 6b) shows that the solubility of Mn_2O_3 in (Mg, Mn)O solid solution increases dramatically above $1300^{\circ}C$. Therefore, Mn exists both as Mn^{+2} and Mn^{+3} in this (Mg,Mn)O solid solution. As has been discussed before, this diagram is not a "true binary diagram" and it cannot predict the distribution of Mn^{+2} and Mn^{+3} in the (Mg,Mn)O phase. This distribution, of course, will vary with temperature and furnace atmosphere.

According to Wagner and Schottky[80], "quasi chemical equations" may be written for the equilibrium between a metal and a surrounding gas. Thus, the change in stoichiometry of the crystal with variable gas pressure may be predicted. For Mn_xO in solid solution with MgO, for example, we can write:

$$2Mn^{+2} + 1/2O_2 \overset{MgO}{\underset{\longleftarrow}{\longrightarrow}} 2Mn^{+3} + V_{Mg}'' + O_o \qquad (5.1)$$
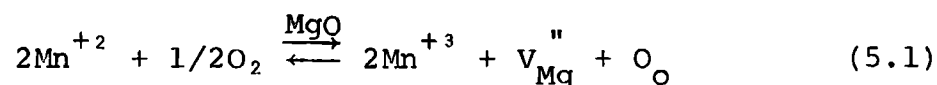
and

$$K = \frac{[V_{Mg}^{''}] [Mn^{+3}]^2}{[Mn^{+2}]^2 \, P_{O_2}^{1/2}} \qquad (5.2)$$

where $V_{Mg}^{''}$ is a cation vacancy and K is the equilibrium

constant. In this approach, we have assumed dilute

solution and not considered any association between

the defects, so the activities can be replaced by

concentrations. In this case, this may be true since

the maximum MnO concentration is 2.5 wt.%.

Now, if it is assumed that the concentration of

vacancies is equal to one-half the Mn^{+3} concentration

in order to maintain electrical neutrality, then

equation 5.2 becomes

$$\frac{4 [V_{Mg}^{''}]^3}{[Mn^{+2}]^2} = K \, P_{O_2}^{1/2} \qquad (5.3)$$

The equilibrium constant is related to temperature

through the relation

$$K = \exp \, (-\Delta G^O/RT) \qquad (5.4)$$

where ΔG^O is the free energy of formation of defects

for the reaction (5.1) and T is the temperature.

Therefore, at a constant temperature, the concentration

of Mn^{+3}, and consequently of $V_{Mg}^{''}$, should increase with

increasing oxygen partial pressure. However, at

constant oxygen partial pressure a decrease with the increasing temperature should be expected. Thus we can expect MnO to be more stable than Mn_2O_3 at high temperatures. Therefore, the phase diagram shown in Figure 6b is nothing else than a plot for the system MgO-Mn oxide for the partial pressure of oxygen in air.

Jones[81], and Jones and Cutler[82] measured the mutual inter-diffusion coefficient in the system Mn_xO-MgO by the Boltzmann-Matano method. They found that diffusion occurs by the counter diffusion of Mg^{+2}, and Mn^{+2}, Mn^{+3} and cation vacancies through a relatively rigid oxygen lattice. They made their experiments under the same atmospheric conditions used in this work, air and $P_{O_2} = 10^{-7}$ KPa. They used temperatures of $1380^O C$, $1480^O C$, and $1565^O C$ for the experiment in air, and $1500^O C$ for those in reducing atmosphere. They showed that the decrease in concentration of Mn^{+3} ions with the firing at $1500^O C$ and $P_{O_2} = 10^{-7}$ KPa, greatly retards the diffusion in the system, in comparison with samples fired in air.

Diffusion in the system MgO-Mn oxides can thus be described as counterdiffusion of Mg and Mn ions through a rigid oxygen lattice. In reducing conditions, the diffusion of Mg^{+2} is counterbalanced by the diffusion of Mn^{+2} in the opposite direction. On the other hand, under oxidizing conditions the diffusion of Mg^{+2} is counterbalanced by the diffusion of either Mn^{+2}, or Mn^{+3} plus a

cation vacancy in the opposite direction. This is illustrated in Figure 12. Magnesium ion diffusion is much faster for the oxidizing atmosphere, where there are more cation vacancies present, than is the case for the reducing atmosphere. In air, the increase in MnO concentration increased the cation vacancy concentration, thereby increasing the lattice diffusion of Mg ions which increased the densification rate. In reducing atmosphere, no cation vacancies are created with the introduction of Mn^{+2}, so the diffusion of Mg^{+2} remains relatively unchanged from the pure case and no change in rate is observed.

2. <u>Influence of Time</u>. Figures 13 and 14 show data for percent total porosity and percent closed pores versus time of sintering for composition A fired at temperatures of 1700 and $1760^{\circ}C$, in air (Figure 13) and in reducing atmosphere of $P_{O_2} = 10^{-7}$ KPa (Figure 14). Data for compositions B, C, D, E, and F are not plotted because they exhibit the same general type of behavior shown for composition A. These data are included only to illustrate porosity changes during the densification process.

As discussed before, the final stage of sintering starts when the continuous pore phase, characteristic of the intermediate stage sintering, becomes discontinuous. In a real process where the particles are not uniform in size and shape and their sintering behavior is not
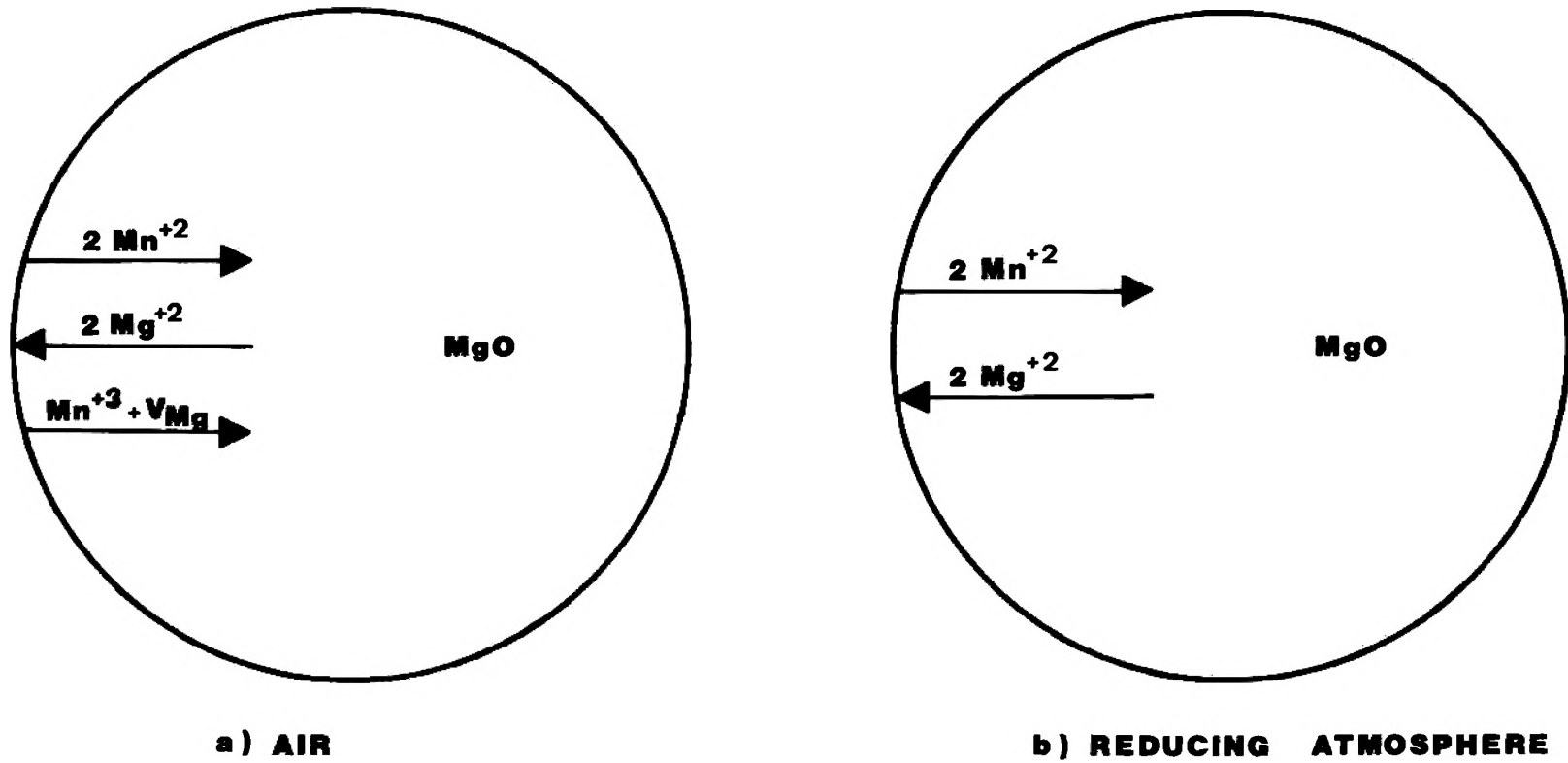
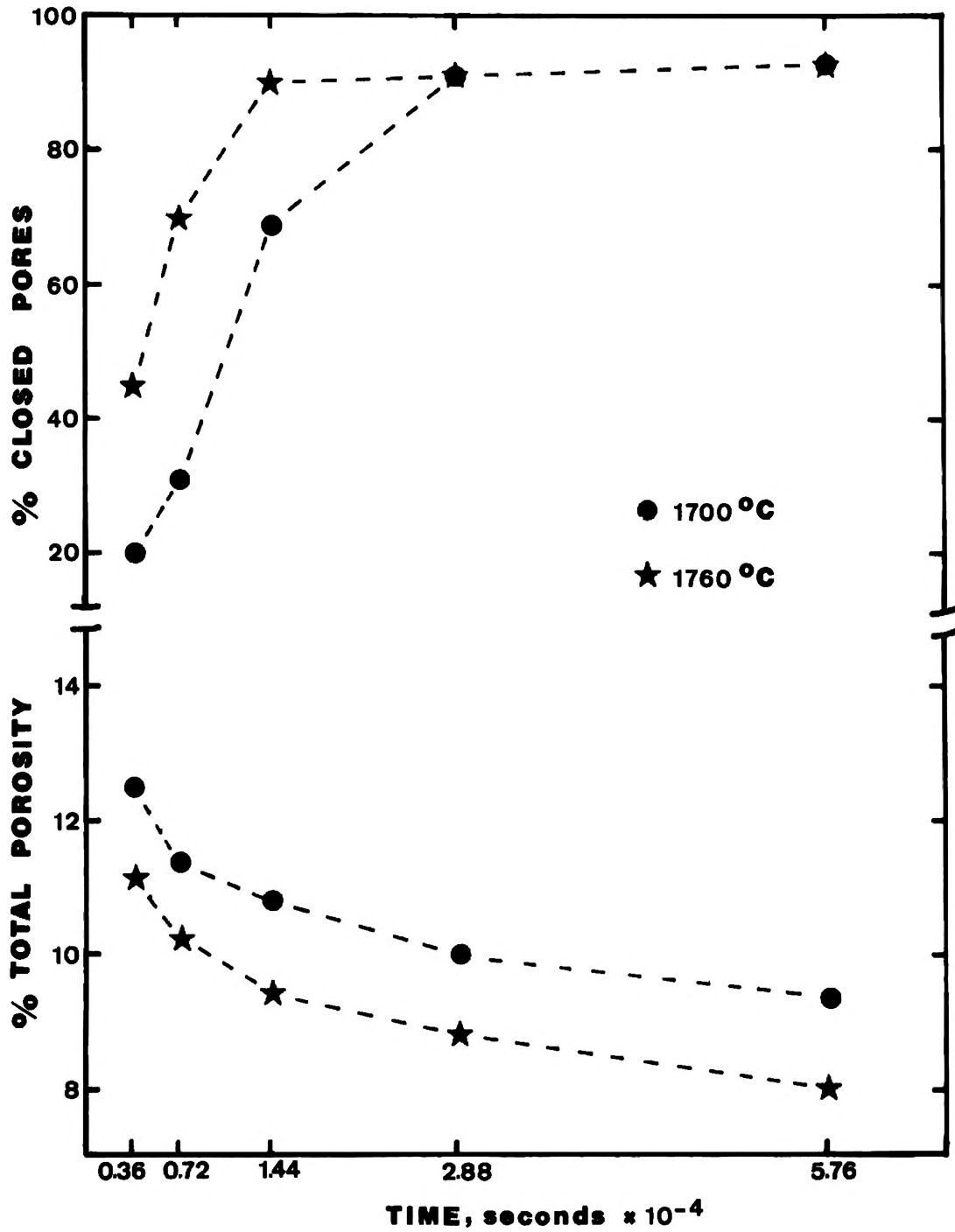Figure 12. Counter-diffusion of Mg and Mn ions in (a) oxidizing and (b) reducing atmospheres.

Figure 13. Percent total porosity and percent closed pores
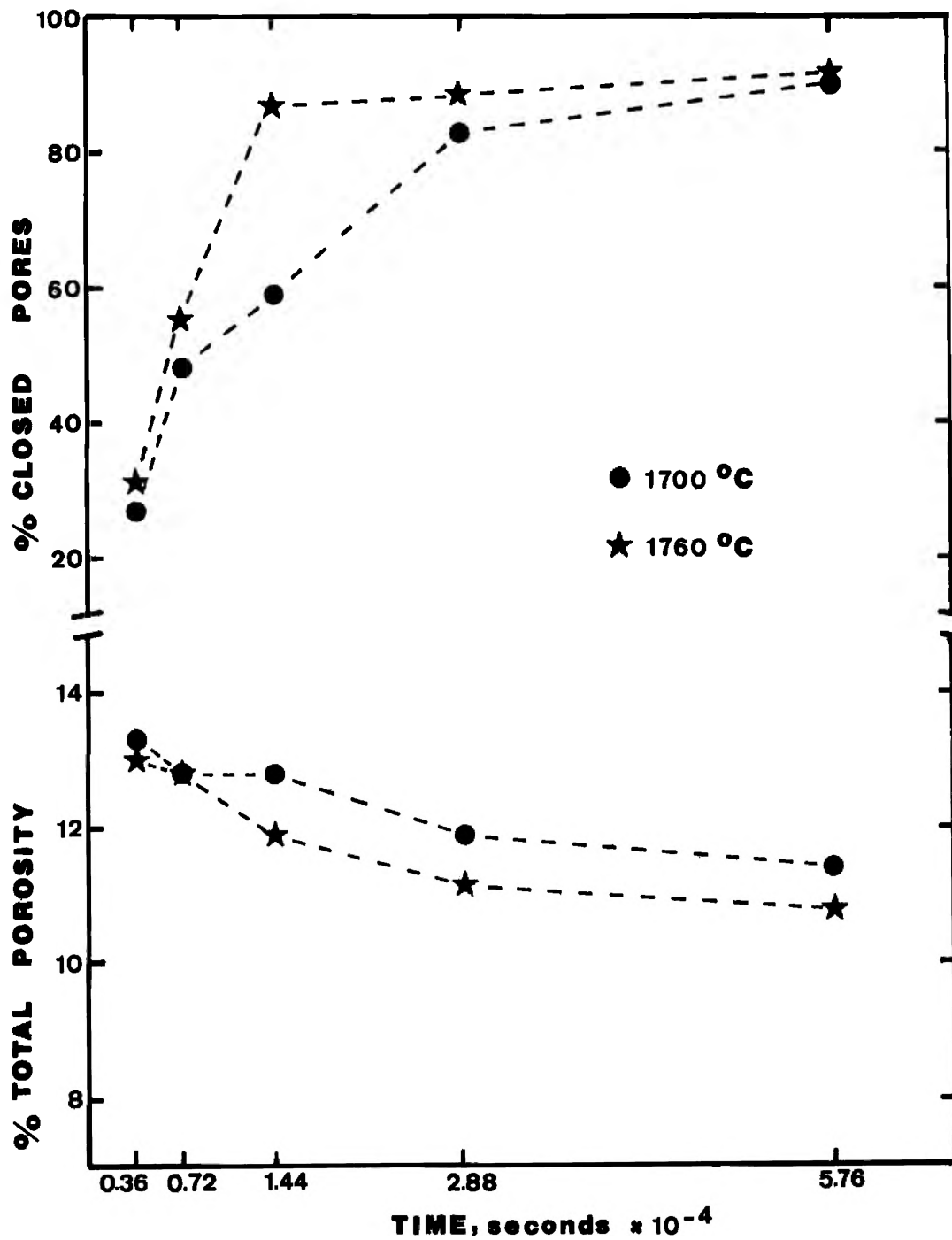versus time of sintering in air for
composition A (MnO = 0.16 wt.%).

Figure 14. Percent total porosity and percent closed pores versus time of sintering in $P_{O_2} = 10^{-7}$ KPa for composition A (MnO = 0.16 wt.%).

homogeneous throughout the material, there is not a sharp limit between the intermediate and the final stage, but rather a time range when the process goes from one stage to the other. This behavior can be easily seen in Figures 13 and 14 in which a transition from the intermediate to the final stage of sintering seems to exist in the time interval 3.6 to 14.4 Ks. Therefore, it appears that for the conditions studied in this investigation, the densification process appears to extend from the intermediate to the final stage.

In general, investigators have used plots of a function of the total porosity versus time of sintering in order to fit their data to a model.[25] The best fit for our data is found by plotting percent total porosity versus logarithm of time. Due to the importance of density, the data are plotted as percent theoretical density instead of percent total porosity. These data are shown in Figures 15, 16, 17, 18, 19, and 20 for compositions A, B, C, D, E, and F, respectively. These figures are plots of percent theoretical density versus logarithm of time for temperatures of 1700 and 1760°C and both atmospheres of air and $P_{O_2} = 10^{-7}$ KPa.

As discussed previously, the intermediate stage of sintering is not simple and the models developed to explain it are not very satisfactory, since either they are very difficult to apply[26] or because they do not take into
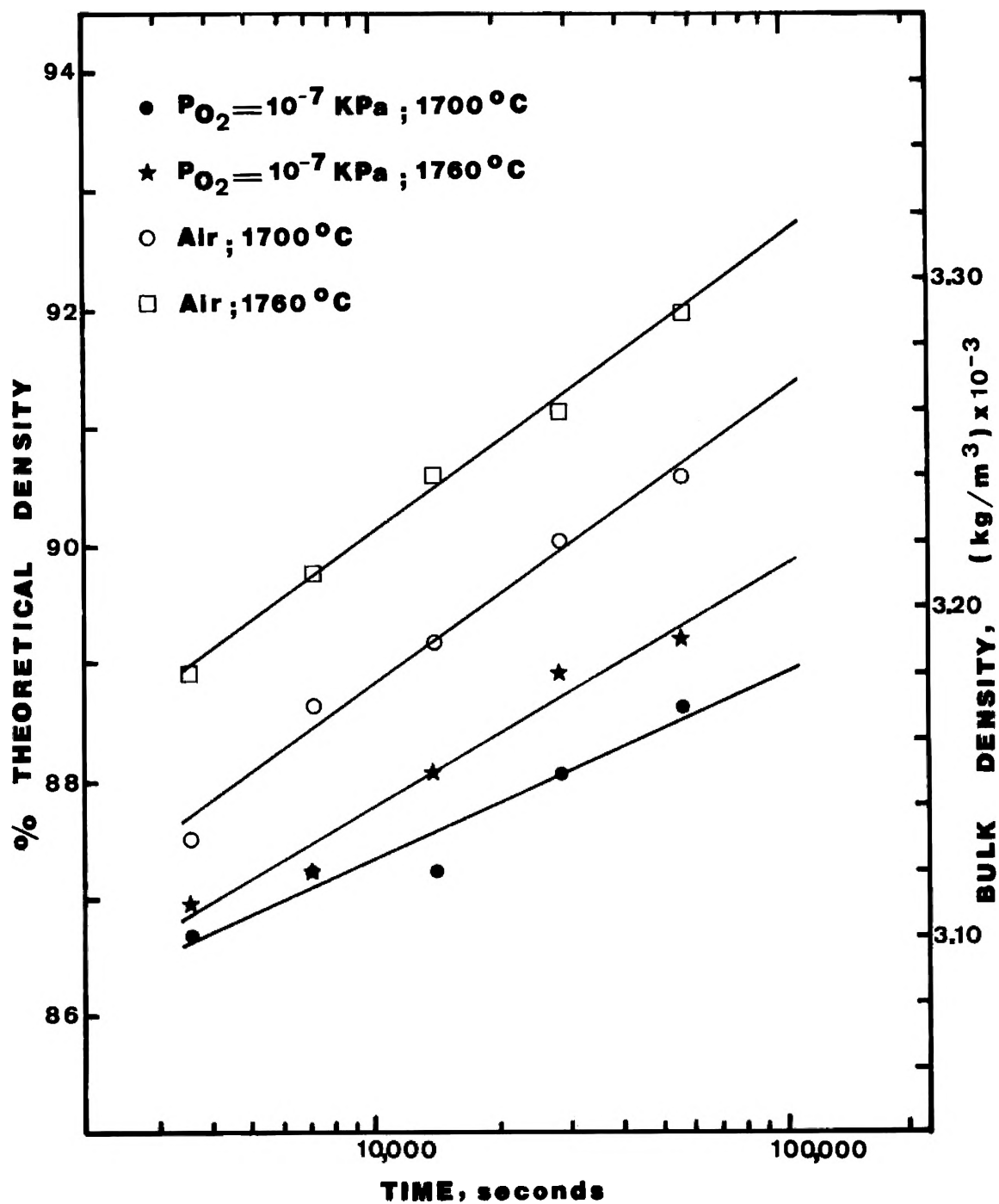
Figure 15.   Percent theoretical density versus logarithm time
of sintering temperature for composition A
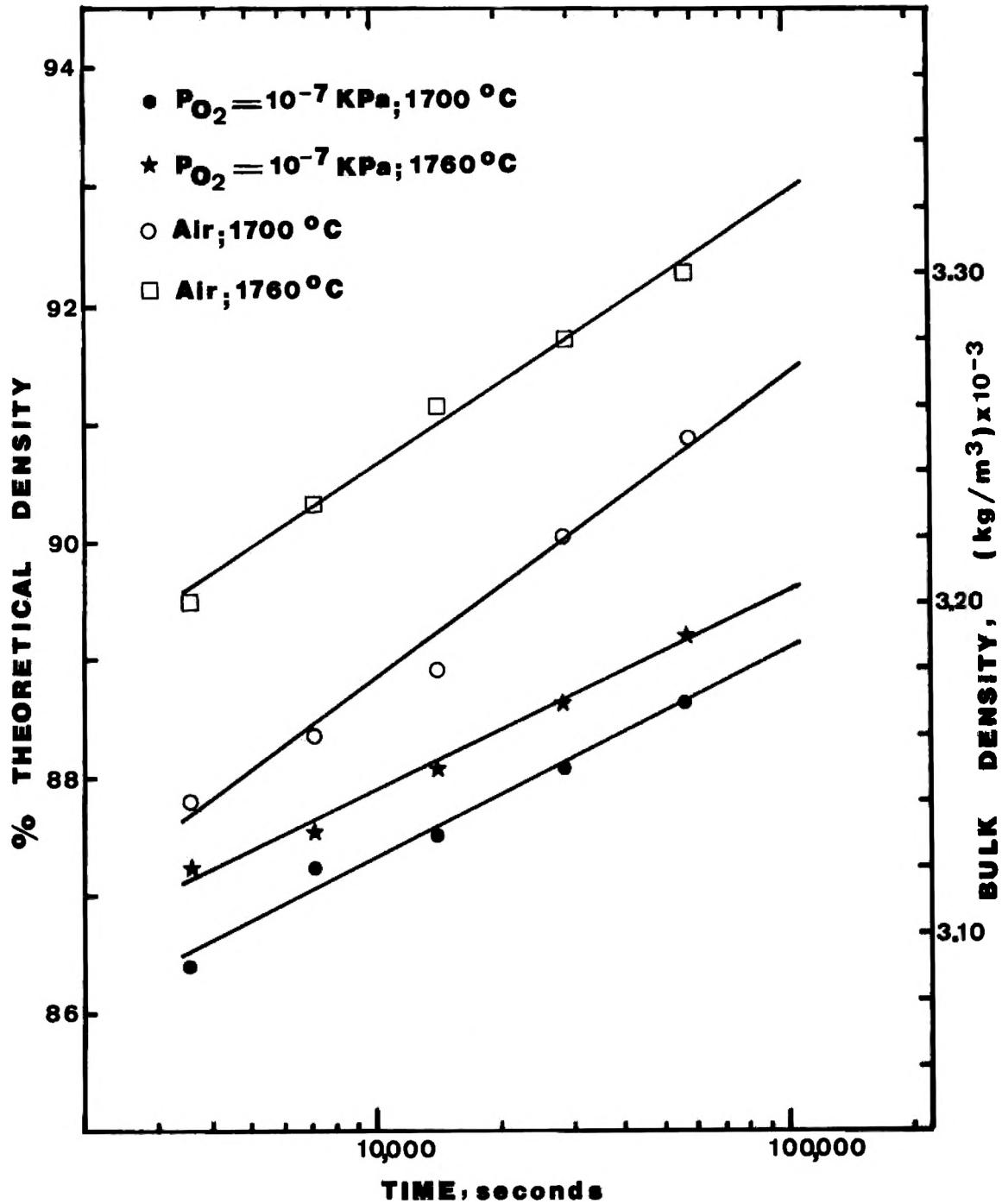(MnO = 0.16 wt.%).

Figure 16. Percent theoretical density versus logarithm time
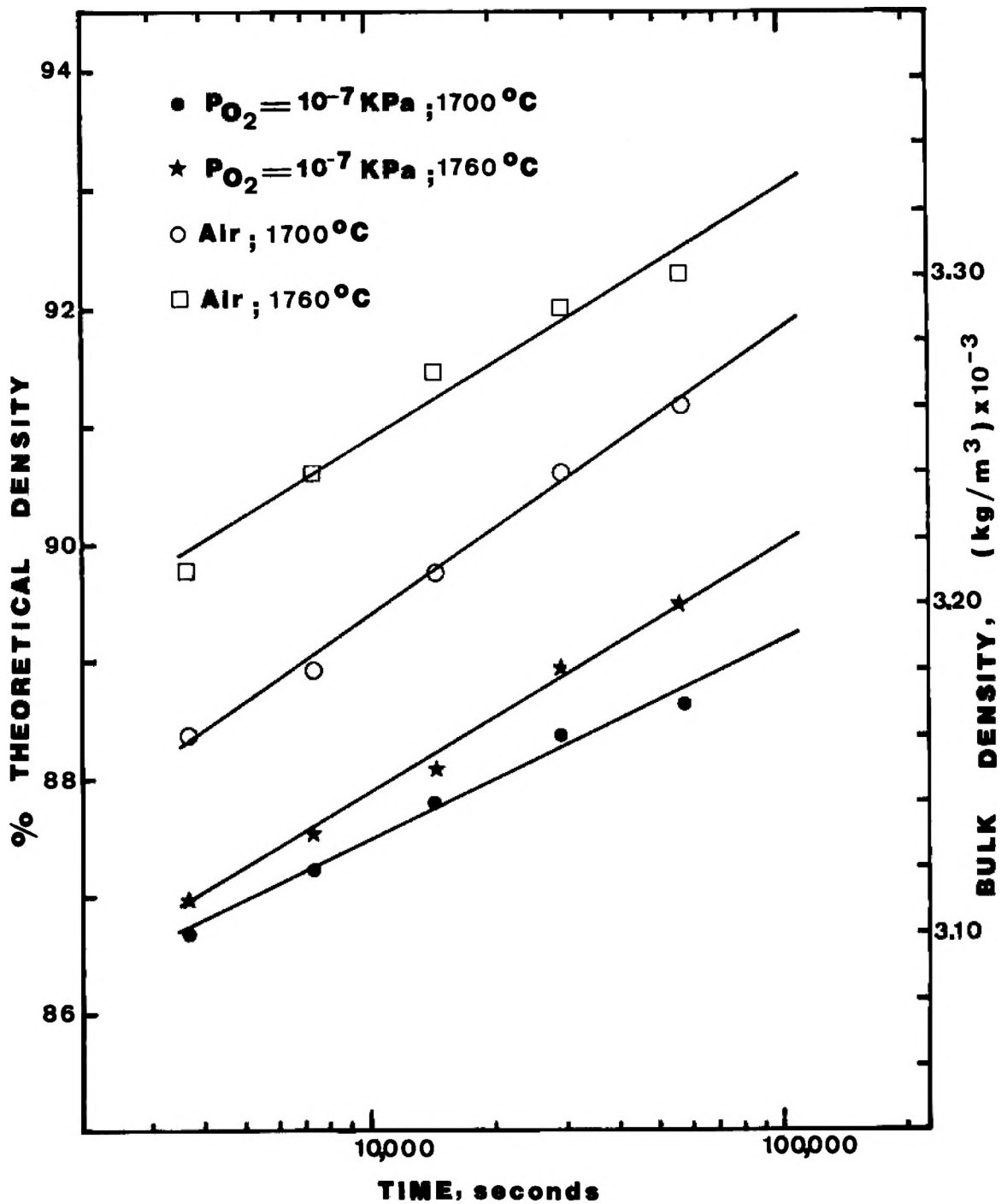of sintering for composition B (MnO = 0.50 wt.%).

Figure 17.   Percent theoretical density versus logarithm time
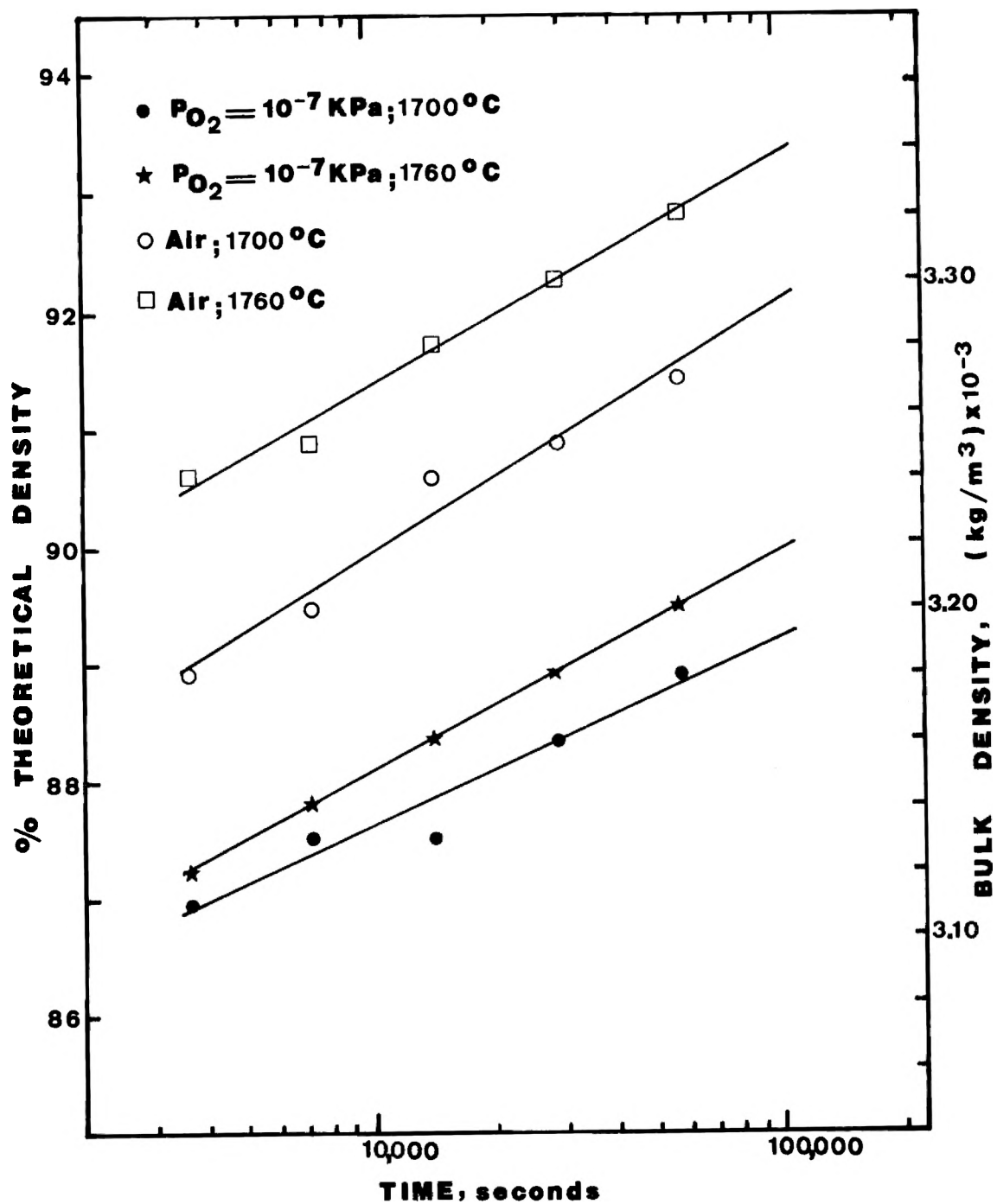   of sintering for composition C (MnO = 1.00 wt.%).

Figure 18. Percent theoretical density versus logarithm time
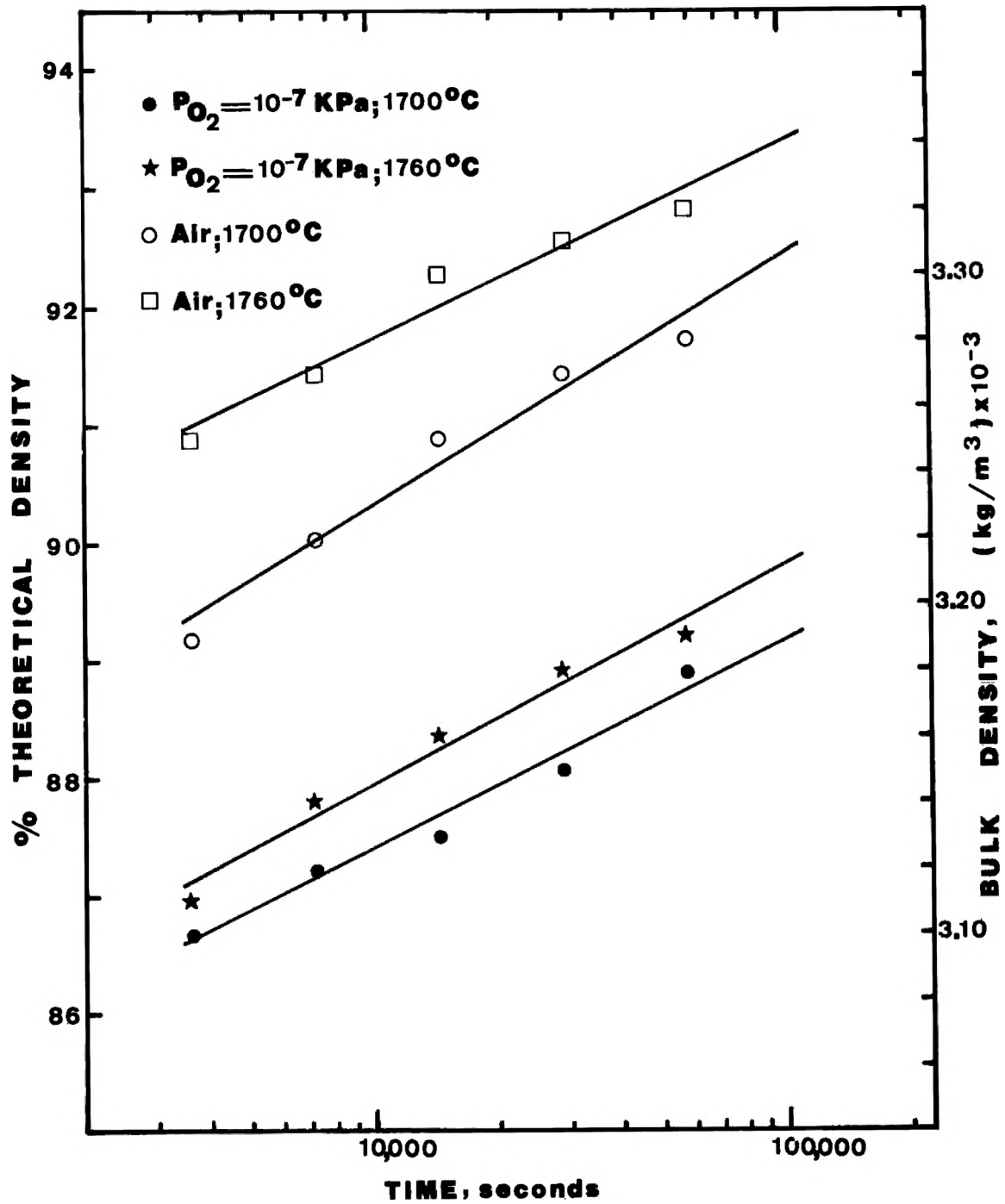   of sintering for composition D (MnO = 1.50 wt.%).

Figure 19. Percent theoretical density versus logarithm time
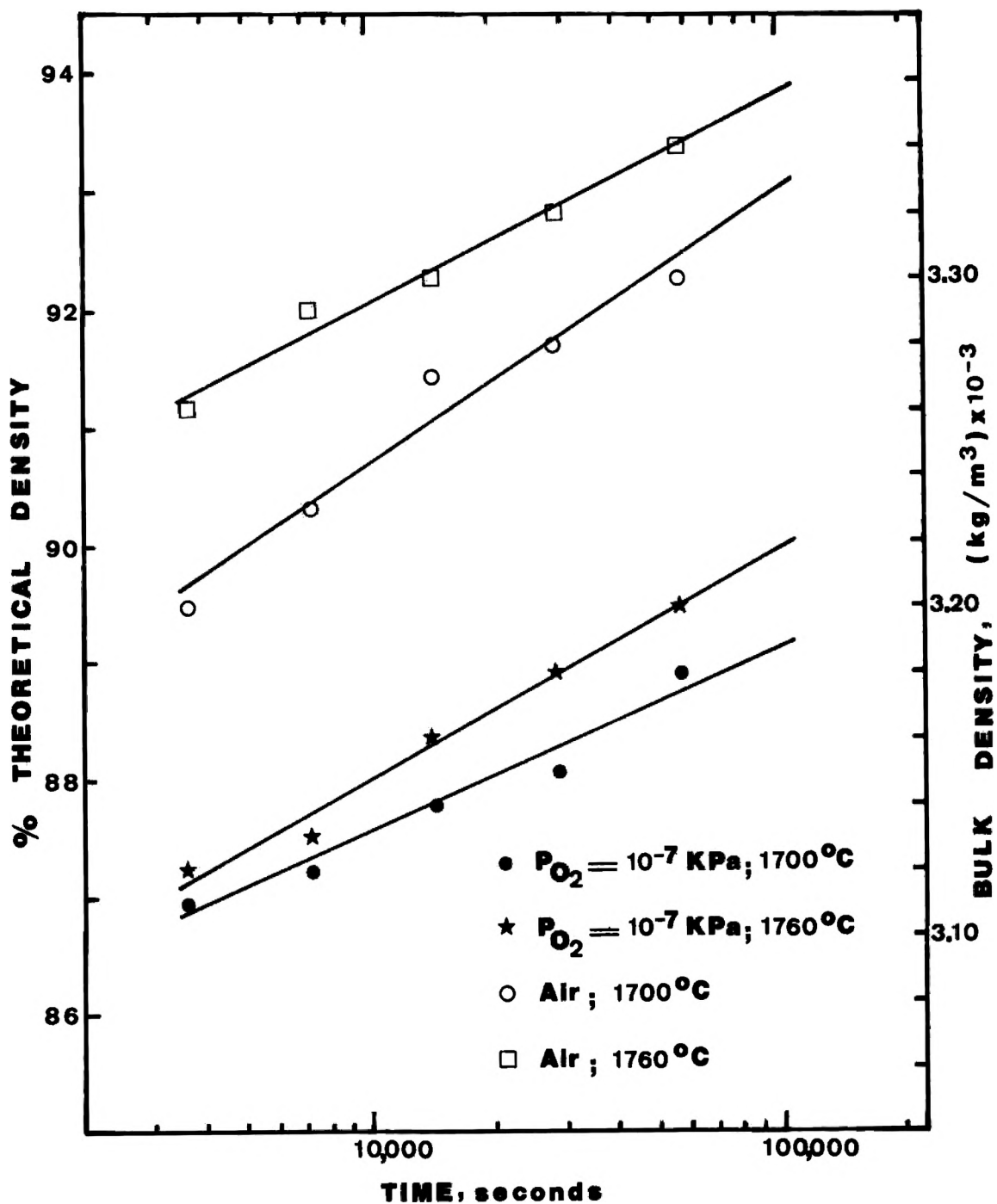of sintering for composition E (MnO = 2.00 wt.%)

Figure 20. Percent theoretical density versus logarithm time
of sintering for composition F (MnO = 2.50 wt.%).

consideration the change in grain size during the
process.[16-18] Thus these data are not being plotted
according to any model but as percent theoretical density
versus logarithm of time. As has been pointed out else-
where there is no theoretical justification in doing
this,[16-18,27] but many investigators have obtained linear
representations of their data with such plots. Attempts
to develop models which yield this type of behavior have
been made, however these models are still not satisfactory.
The sintering phenomena is very complex and has many
variables which can modify the rate of the process and
consequently it is very difficult to develop a model which
can explain all cases.

A very important feature of Figures 15 to 20 is the
influence of atmosphere on densification process. In
reducing atmosphere ($P_{O_2} = 10^{-7}$ KPa), the densification
is much lower than the densification in air and this
difference increases with MnO content. However, most of
the difference in densification occurs during heat up and
within the first 3,600s of sintering, as is illustrated
in Table XV. The percent of the density difference up to
3,600s of the sintering time was calculated as follows:

% Density Difference =

$$\left(\frac{\text{Density Difference up to 3,600s}}{\text{Density Difference up to 57,600s}}\right) \times 100 \quad (5.5)$$

TABLE XV

PERCENT OF THE DENSITY DIFFERENCE (Kg/m^3) BETWEEN SAMPLES FIRED IN AIR VERSUS IN $P_{O_2} = 10^{-7}$ KPa, WHICH OCCURS UP TO 3,600 s OF SINTERING

	Time	A	B	C	D	E	F
Density Difference at 1700°C (Kg/m^3)	3.6 Ks	20	20	35	50	75	80
	57.6 Ks	50	60	65	80	95	105
Density Difference at 1760°C (Kg/m^3)	3.6 Ks	50	65	85	95	115	125
	57.6 Ks	75	90	85	100	110	120
% Density Difference up to 3.6 Ks	1700°C	40%	33%	54%	63%	79%	76%
	1760°C	67%	72%	100%	95%	105%	104%

As we can see, the percent density difference up to 3,600s of sintering increases with temperature (from 1700 to 1760°C) and increases with MnO concentration. Therefore, these results show that most of the influence of MnO on densification occurs during heat up and within short sintering times. This behavior may be explained by the fact that the concentration of Mn^{+3} and Fe^{+3} in the MgO grain decreases at high temperatures for the samples fired in air, consequently reducing the difference between vacancy concentrations and densification rates in comparison to the samples fired in reducing atmosphere.

Another very important technological aspect of Figures 15 to 20 is the relative importance of temperature versus time on densification. On the average, 7,200s of sintering in air at 1760°C causes the same densification that 32,400s of sintering in air at 1700°C. These results show that temperature is a much more important variable than time in the densification of our MgO grain. Therefore, it might be concluded that for better densification of the MgO grain, we need to fire it at high temperatures under an oxidizing atmosphere and not necessarily for long periods of time.

3. **Influence of Temperature.** Tables XII, XIII, and XIV show density and porosity data versus temperature for a sintering time of 57,600s for all compositions. These data are plotted in Figures 21 (composition A),

22 (composition B), 23 (composition C), 24 (composition D),
25 (composition E), and 26 (composition F) for both
oxidizing (air) and reducing atmospheres ($P_{O_2} = 10^{-7}$ KPa).

For the range of temperature being investigated
(1520 to 1760°C), the densification of our MgO grain
sintered in air increased monotonically with temperature.
However, the densification behavior under reducing
conditions is not so simple and may be divided in two
parts. The first one goes from 1520 to 1640°C where the
densification also increases constantly with temperature.
In this region, the densities of samples fired in air and
in reducing atmosphere are nearly the same except for the
higher MnO concentrations. The second part occurs for
temperatures higher than 1640°C. Here it can be observed
that for all compositions as the temperature increases the
density decreases slightly in the temperature range 1640
to 1700°C followed by a small increase at 1760°C. In this
region, the density difference between samples fired in
air versus samples fired in reducing atmosphere becomes
very large and increases with the MnO concentration.

The reason for the small change in densification
behavior for the samples fired under reducing conditions
when the sintering temperatures goes from 1640 to 1700°C
appears to be associated with an evaporation process. It
was observed that these pellets had lost weight beyond what
we could expect from the evaporation of the binder and from
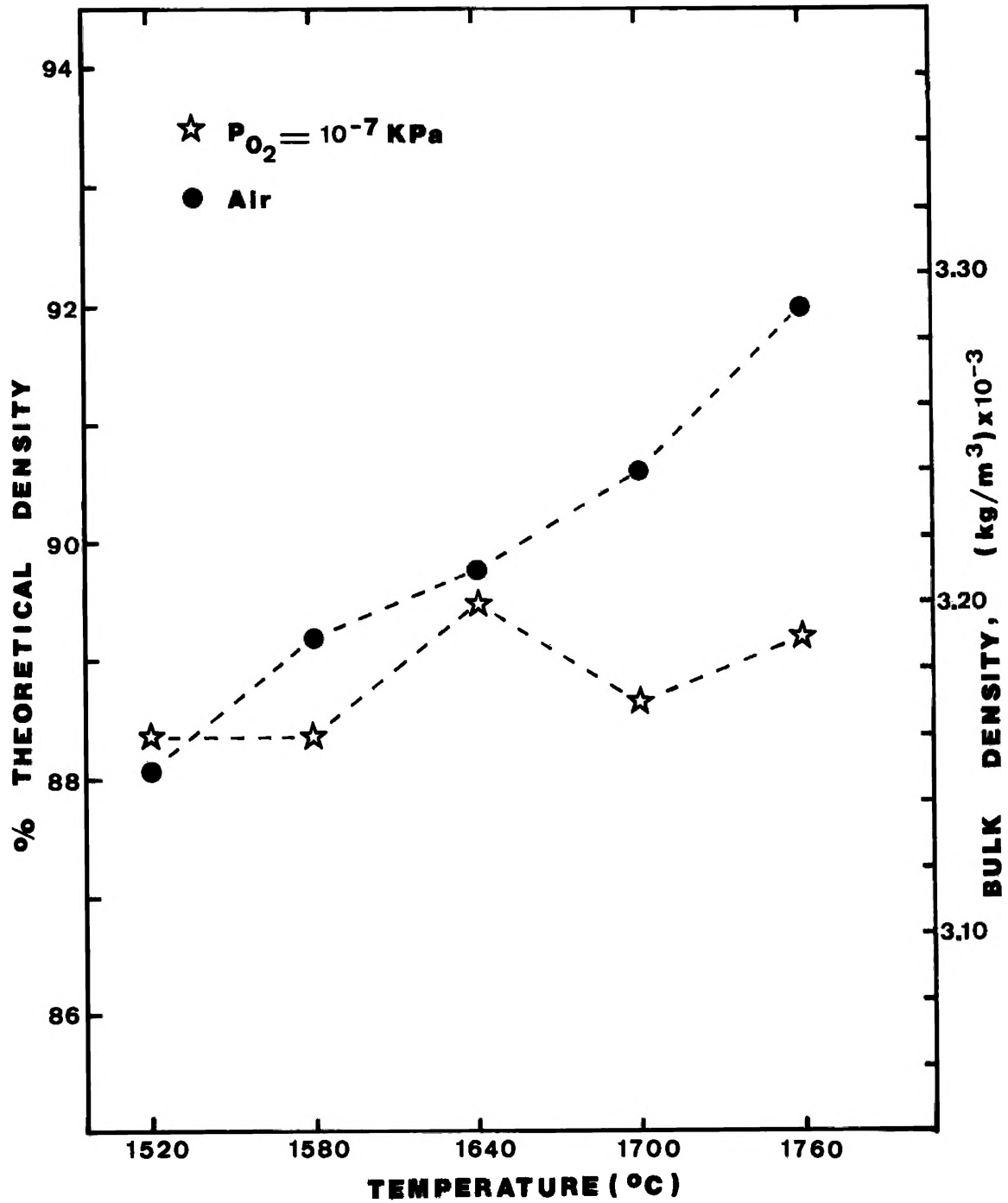
Figure 21. Percent theoretical density versus sintering
temperature (soaking time of 57,600s) for
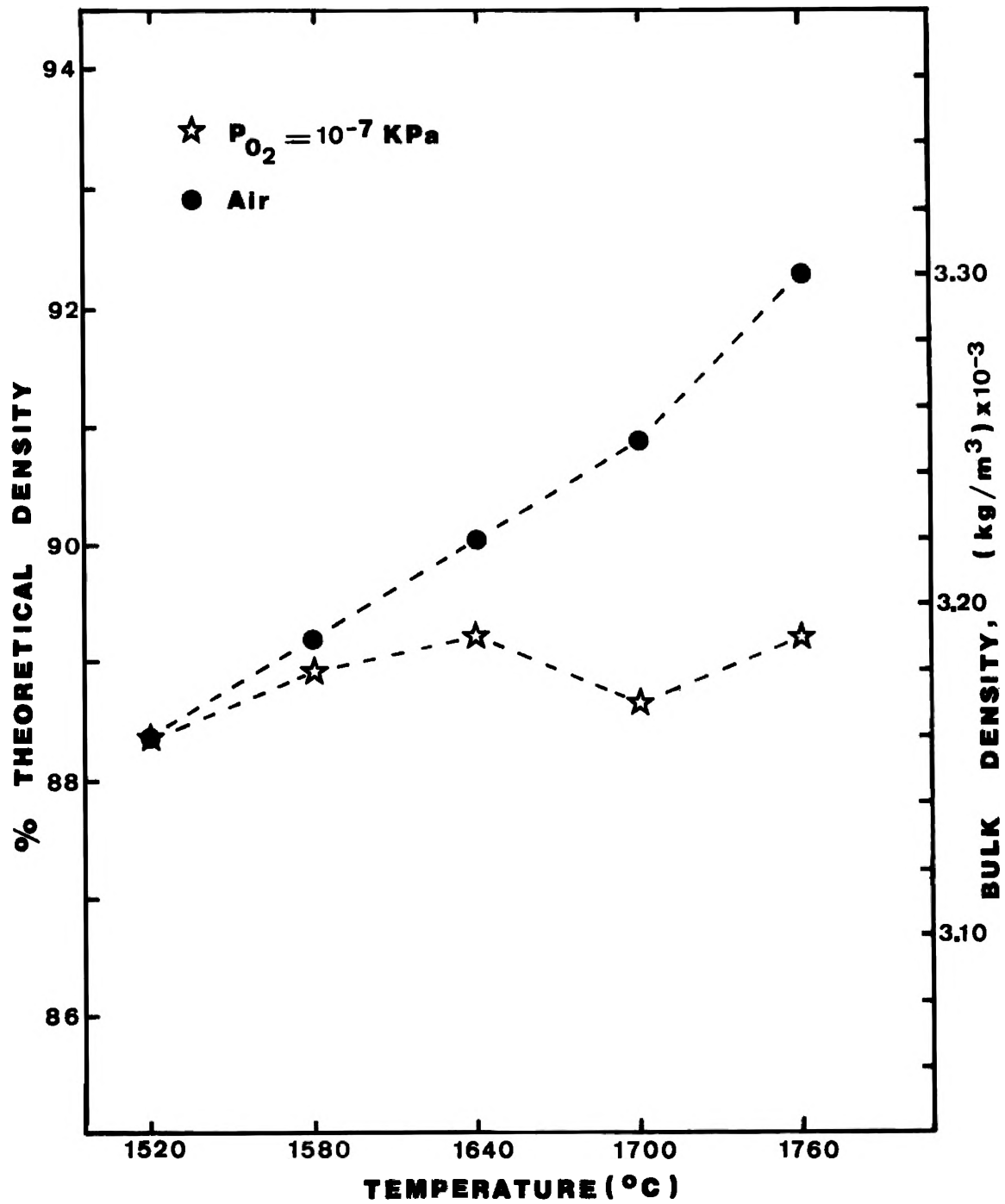composition A (MnO = 0.16 wt.%).

Figure 22. Percent theoretical density versus sintering
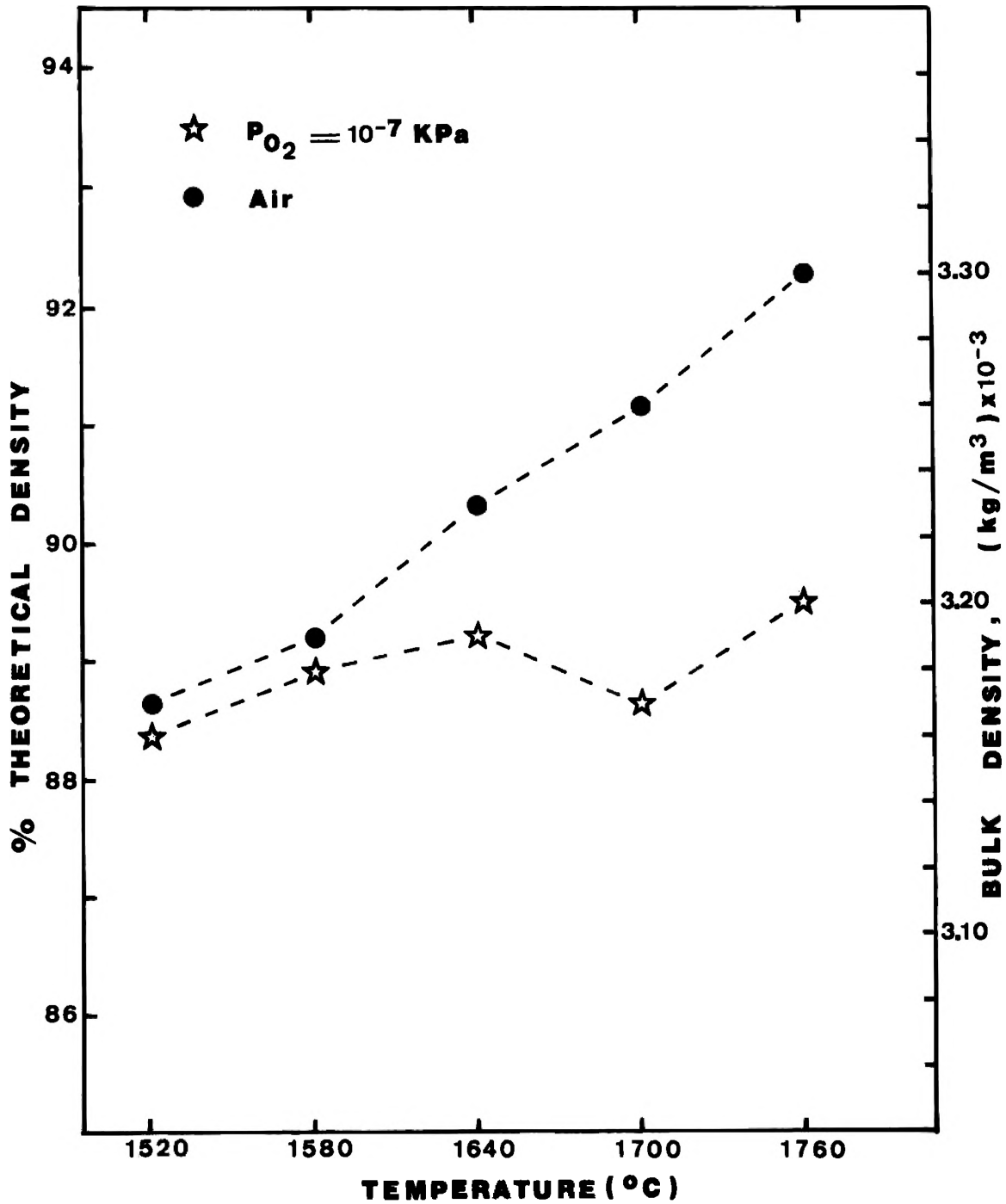temperature (soaking time of 57,600s) for
composition B (MnO = 0.50 wt.%).

Figure 23. Percent theoretical density versus sintering
temperature (soaking time of 57,600s) for
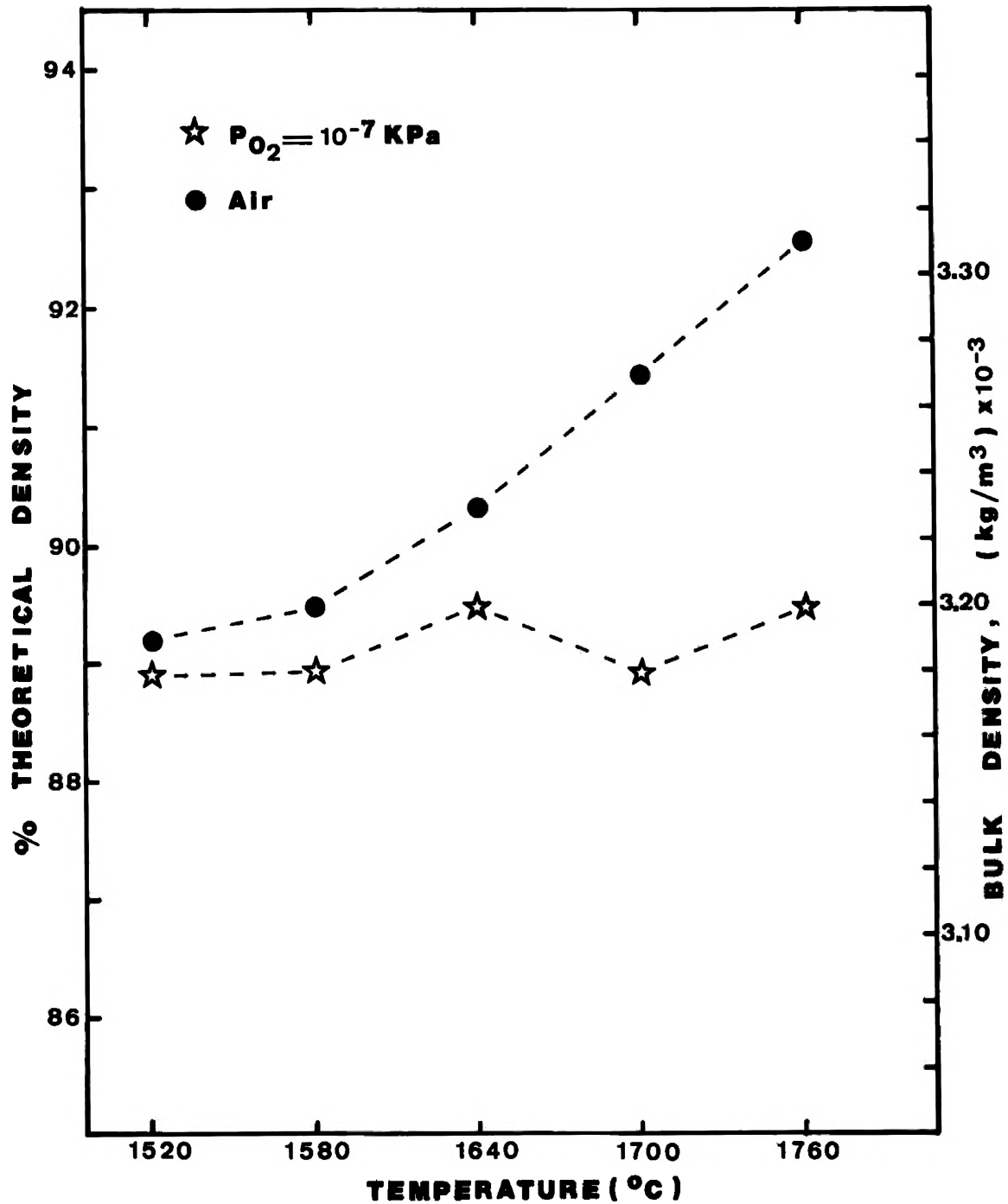composition C (MnO = 1.00 wt.%).

Figure 24. Percent theoretical density versus sintering
temperature (soaking time of 57,600s) for
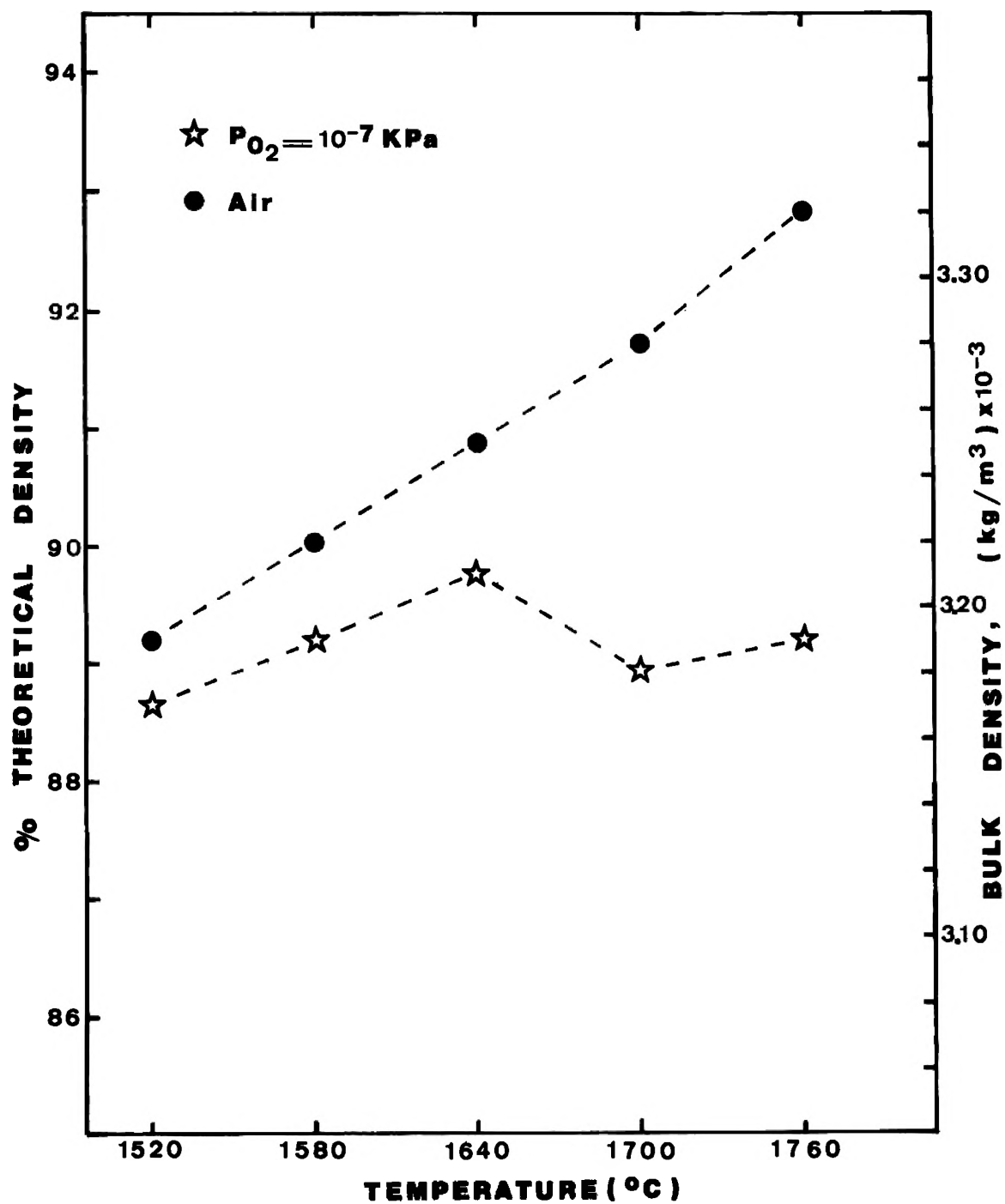composition D (MnO = 1.50 wt.%).

Figure 25. Percent theoretical density versus sintering
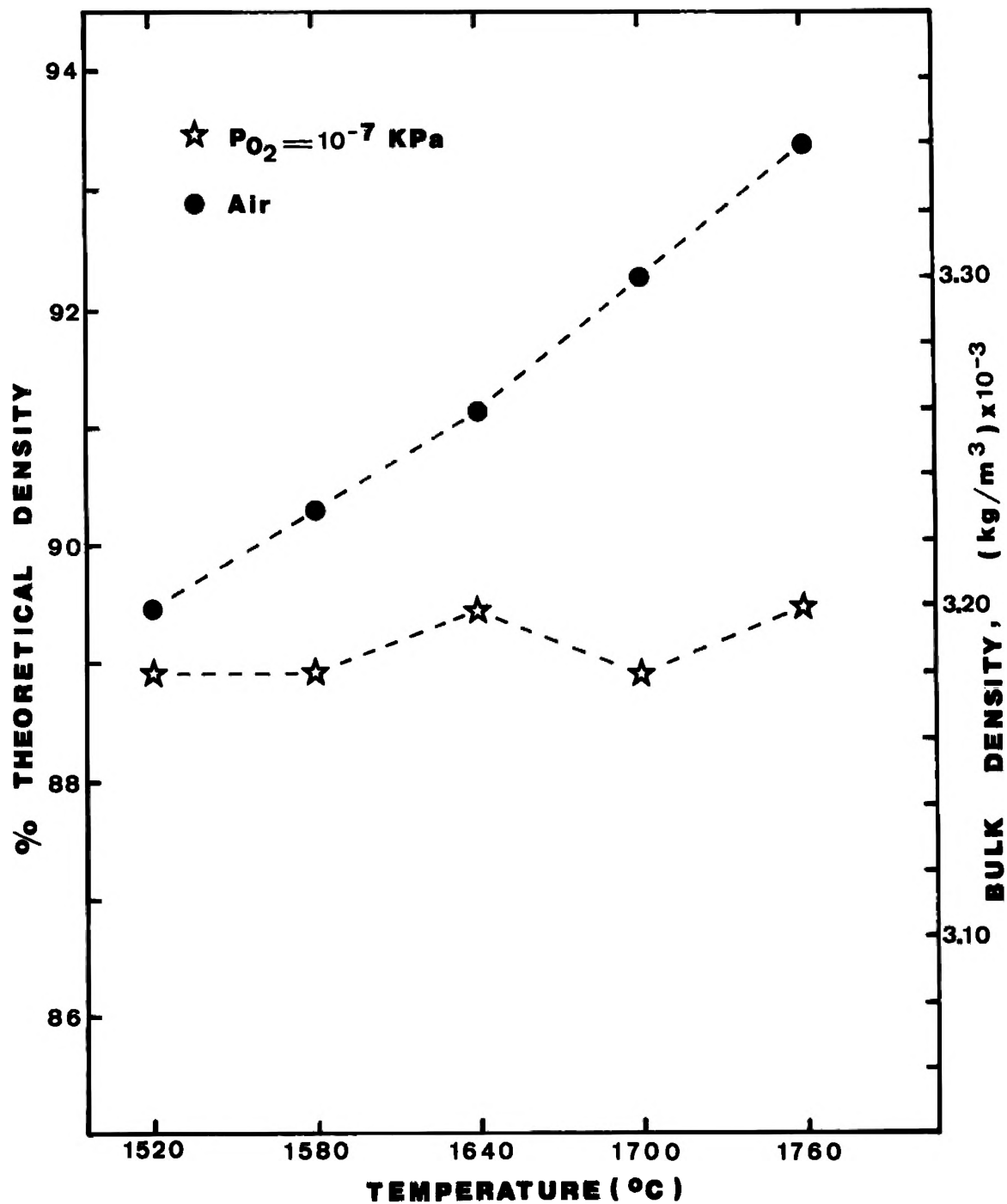temperature (soaking time of 57,600s) for
composition E (MnO = 2.00 wt.%).

Figure 26. Percent theoretical density versus sintering
temperature (soaking time of 57,600s) for
composition F (MnO = 2.50 wt.%).

the change in oxidation state of manganese and iron ions. In fact, these pellets were deformed in shape, and their dimensions could not be measured accurately, as discussed before. Weight measurements showed that at 1760°C the weight loss increased from about 0-1% for a sintering time of 3,600s to about 4-5% for a sintering time of 57,600s. For the temperature of 1700°C that weight loss was not detectable for sintering time of 3,600s, but was determined to be about 1-2% for sintering time of 57,600s.

To confirm the weight loss results and to see whether the presence of water vapor influenced the results, another experiment was made. Samples which had been fired in air for 3,600s were heated to 1760°C for 57,600s in atmosphere of $P_{O_2} = 10^{-7}$ KPa, using either CO/CO_2 or H_2/CO_2 as buffer gases. The results (Figure 27) show that a considerable weight loss does occur and that the weight loss in the H_2/CO_2 buffer gas system are slightly larger than that for CO/CO_2 buffer gas system. These data confirm the results found by Jungquist[83] firing pure MgO at 1600°C for 3,600s and $P_{O_2} \leq 10^{-7}$ KPa with CO/CO_2 and H_2/H_2O as buffer gases.

Most of the weight loss seems to be associated with a process of reduction of MgO and volatilization of Mg according to:
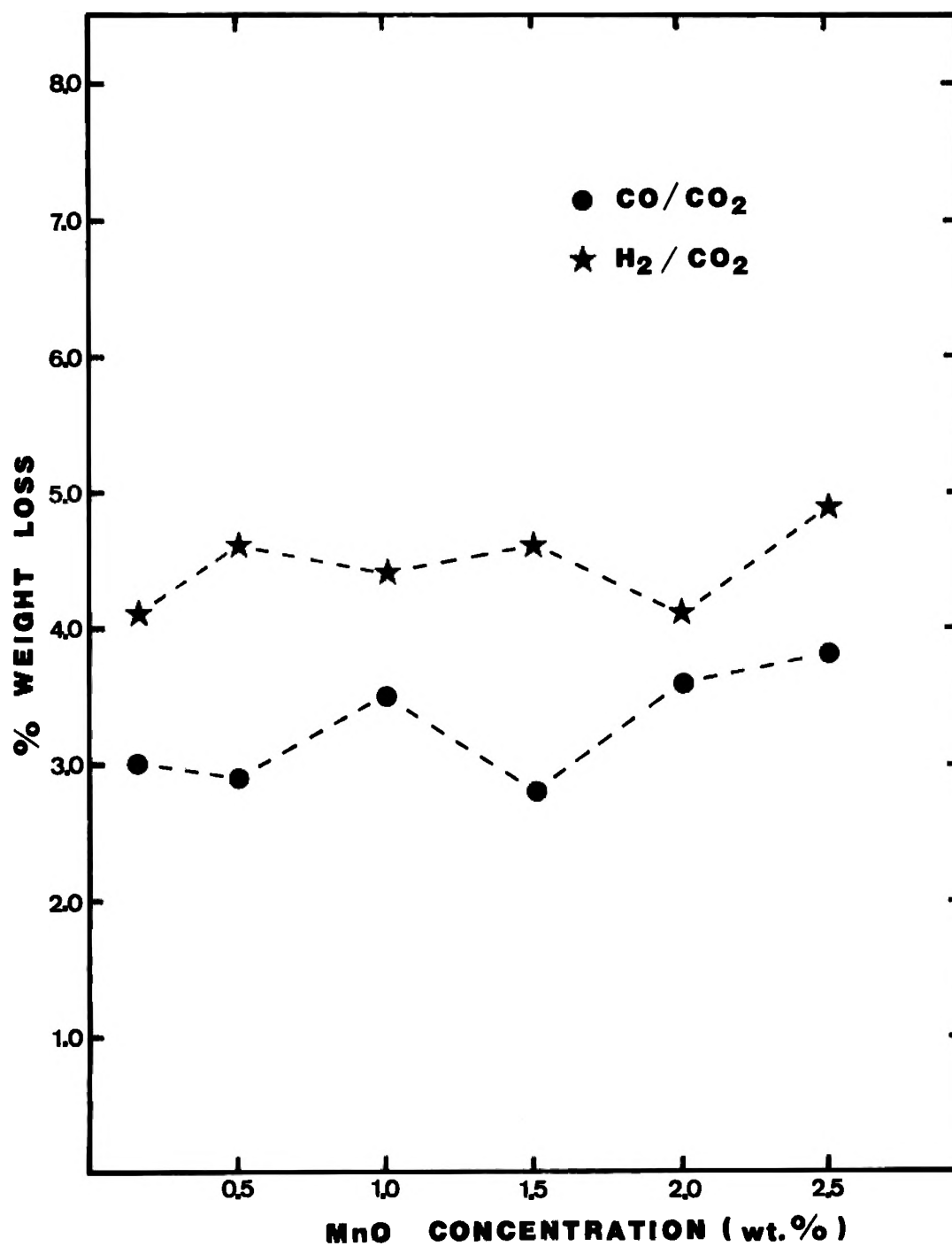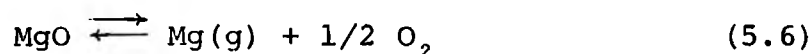
Figure 27. Percent weight loss versus MnO concentration for
samples fired at 1760°C for 57,600s in
$P_{O_2} = 10^{-7}$ KPa either using CO/CO_2 or H_2/CO_2
as buffer gases.

$$MgO \xrightleftharpoons{} Mg(g) + 1/2 \; O_2 \tag{5.6}$$

and

$$K = P_{Mg} \cdot P_{O_2}^{1/2} \tag{5.7}$$

where P_{Mg} is the partial pressure of Mg. At $2000^\circ K$, data in the literature[84] show that log K is equal to -8.355. Therefore, by using equation (5.7) we find that P_{Mg} is equal to 0.015 KPa. Although this partial pressure of magnesium is small, the long time (57,600s) used seems to be enough to cause the weight loss found in Figure 27, at least for the case with CO/CO_2 buffer gases. The higher weight loss for H_2/CO_2 buffer gases seems to be associated with an additional contribution of a competing process for removing Mg from the surface of the crystals due to a reaction of water vapor and Mg^{+2} with formation of $Mg(OH)_2$, which then evaporates. In fact, personal communication obtained from Anderson[85] shows that for firing pure MgO in N_2 at temperature of $1725^\circ C$, under a P_{O_2} = 0.1 KPa and P_{H_2O} = 10.1 KPa, there is a weight loss rate of 0.21 $\mu Kg/s$ for each square meter of specific surface. Since the conditions of P_{O_2}, temperature and time in our studies are favorable for the weight loss of the MgO grain, it is reasonable to explain the reduction in densification rate for samples fired at temperatures higher than $1640^\circ C$ in reducing atmosphere

to be due to the vaporization process mentioned above. As seen earlier, the evaporation-condensation as well as the surface diffusion mechanisms of matter transport have a deleterious effect on the densification rate, since they contribute to the decrease of excess free energy without causing densification.

4. Influence of Atmosphere. In a pure MgO system the number of vacancies increases exponentially with temperature. On the other hand, if aliovalent impurities are present in the system, the vacancy concentration may be controlled by the number of impurities present, and will be independent of temperature (extrinsic behavior). This temperature independence is not true when the impurity can change the oxidation state as in the case of Mn and Fe present in the MgO grain. In fact, in this case, the vacancy concentration will be dependent on partial pressure of oxygen and on temperature. The concentrations of Mn^{+3} and Fe^{+3} increase with partial pressure of oxygen and decrease with the increase of temperature.

Single crystal MgO tracer diffusion data shows that oxygen diffusion is several orders of magnitude slower than that for Mg[86,87]. On this basis, sintering should be controlled by the lattice diffusion of oxygen. However, Gupta[34] and other investigators have found that the sintering rate of MgO is controlled by lattice

diffusion of Mg ions, because the sintering rate is quantitatively related to the diffusion of Mg. Gupta[34] then proposed that the oxygen diffusion occurs mainly along grain boundaries where oxygen diffusivity is known to be much greater than in the crystal lattice.[88,89]

Kingery[90] has suggested that the ionic nature of ceramic oxides leads to the formation of an electrostatic potential on grain-boundaries which depends strongly on defect structure, impurity concentrations, and temperature. Therefore, the surface and grain boundaries of an ionic crystal may carry an electric charge resulting from the presence of excess ions of one sign; this charge is just compensated by a space-charge cloud of the opposite sign adjacent the boundary. The magnitude and sign of the boundary charge will change when there are aliovalent solutes present which alter the concentrations of lattice defects in the crystal. Kingery[91] also showed that these aliotropic solutes tend to segregate in the space-charge region, having a significant effect on the magnitude of the charge. This segregation has been detected on grain boundaries of polycrystalline MgO[91-98]. Kingery[91] has also suggested that materials like MgO which has substantial preference for grain-boundary diffusion of only one ion (O in MgO), the grain-boundary charge has the same sign as this ion (negative sign for MgO).

As has already been discussed, the atmosphere has a large influence on densification of MgO. The atmosphere changes the concentration of Mn^{+3} and Fe^{+3} ions, consequently affecting the concentration of cation vacancies. Since the diffusion of Mg is in general the rate-limiting ion in the densification process of MgO, a reduction in the cation vacancy concentration directly influences the lattice diffusion of Mg and reduces the densification. According to Sonder et al.[99], the oxidation or reduction of Fe (or Mn) impurity ions due to changes in ambient oxygen partial pressure requires three steps or reactions: (1) the reaction of oxygen gas at the MgO surface to produce or remove lattice defects and charges; (2) the propagation of lattice defects and charge into the bulk of the crystal; and, (3) the actual change in valence of the impurity ions. They assumed that the propagation step is the rate limiting.

In the opinion of this author, if the partial pressure of oxygen is low enough, it can have not only a deleterious effect in diffusion of Mg ions through the MgO lattice, but also a deleterious effect on grain-boundary diffusion of oxygen ions. In fact, the low oxygen partial pressure may remove the excess oxygen on the surface, decreasing the segregation of Mn^{+3}, Fe^{+3} and cation vacancies in the space-charge region. This causes a reduction in the diffusion of oxygen in

the grain-boundary since the cation vacancy concentration in this region is very important for the mechanism of diffusion for oxygen ions. Figure 28 illustrated this fact and also the case for firing in oxidizing conditions where oxygen will be available at the surface and at the grain boundaries forming a space-charge region with segregation of Fe^{+3}, Mn^{+3} and cation vacancies and where the oxygen can diffuse faster. Thus the combination of the reduction in cation vacancy concentration and the increased sublimation rate under reducing conditions makes the use of reducing atmospheres very detrimental to the production of dense MgO.

B. MICROSTRUCTURE STUDIES

Most of the microstructure studies, either by using optical microscopy or electron micro-probe analysis, have been done by the Department of R & D of MAGNESITA SA of Brazil. Therefore, part of the discussion here is based on the internal report DPD 118/81[100] of this department. Photographs in Figures 29 to 40 show microstructures taken using optical microscopy for compositions A (#29 for air, #30 for $P_{O_2} = 10^{-7}$ KPa), B (#31 for air, #32 for $P_{O_2} = 10^{-7}$ KPa), C (#33 for air, #34 for $P_{O_2} = 10^{-7}$ KPa), D (#35 for air, #36 for $P_{O_2} = 10^{-7}$ KPa), E (#37 for air, #38 for $P_{O_2} = 10^{-7}$ KPa), and F (#39 for air, #40 for $P_{O_2} = 10^{-7}$ KPa), after sintered at $1760^{\circ}C$ for 57,600s.
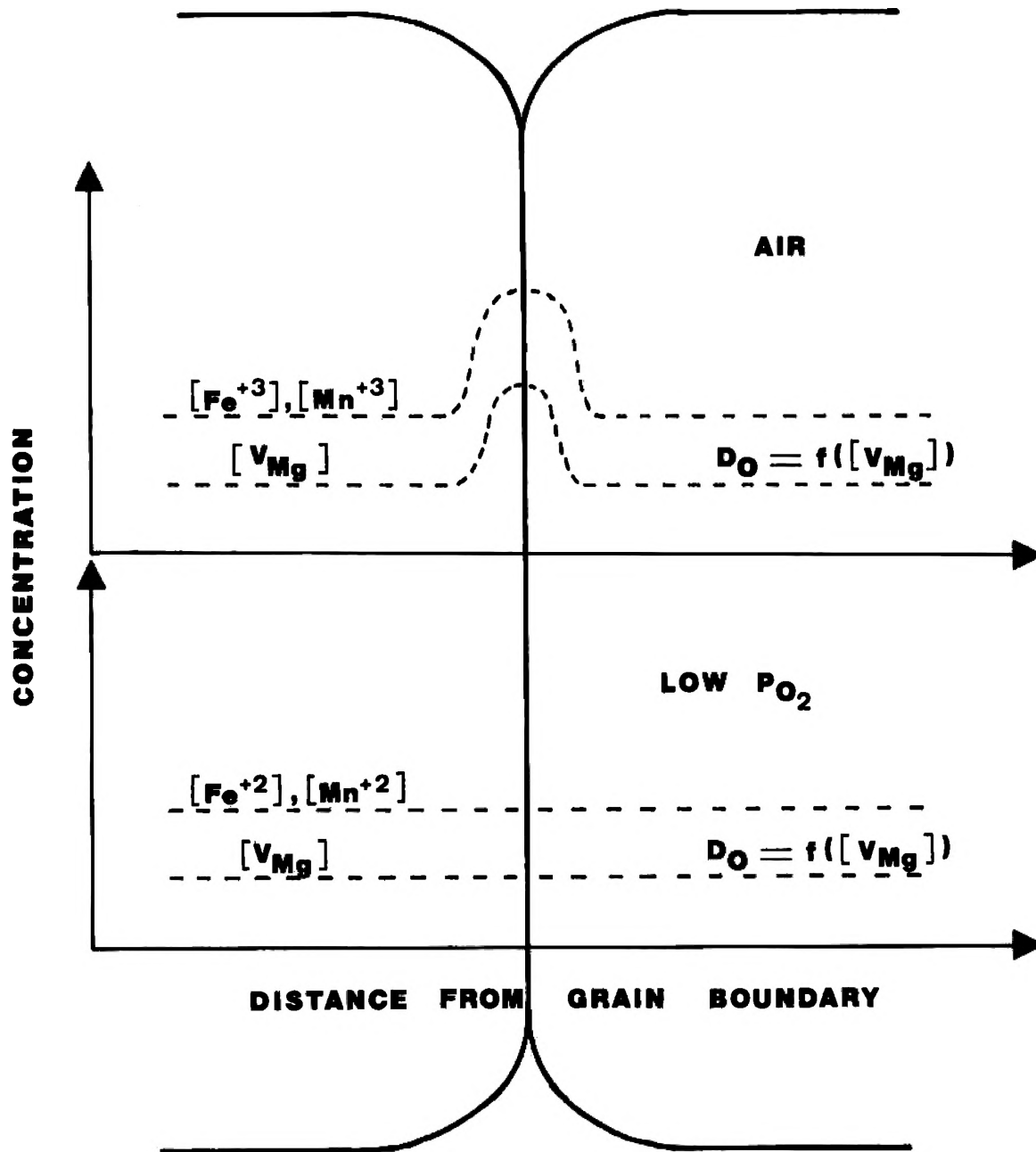
Figure 28. Influence of Mn and Fe ions segregation at the
grain boundary of MgO, on the grain boundary
diffusion of oxygen ions under different
atmospheres.

Figure 29. Optical microscopy photograph for composition A fired at 1760°C for 57,600s in air (magnification of 240x).

Figure 30. Optical microscopy photograph for composition A fired at 1760°C for 57,600s in $P_{O_2} = 10^{-7}$ KPA (magnification of 240x).

Figure 31.   Optical microscopy photograph for composition B
fired at 1760°C for 57,600s in air (magnification
of 240x).

Figure 32.   Optical microscopy photograph for composition B
fired at 1760°C for 57,600s in $P_{O_2} = 10^{-7}$ KPa
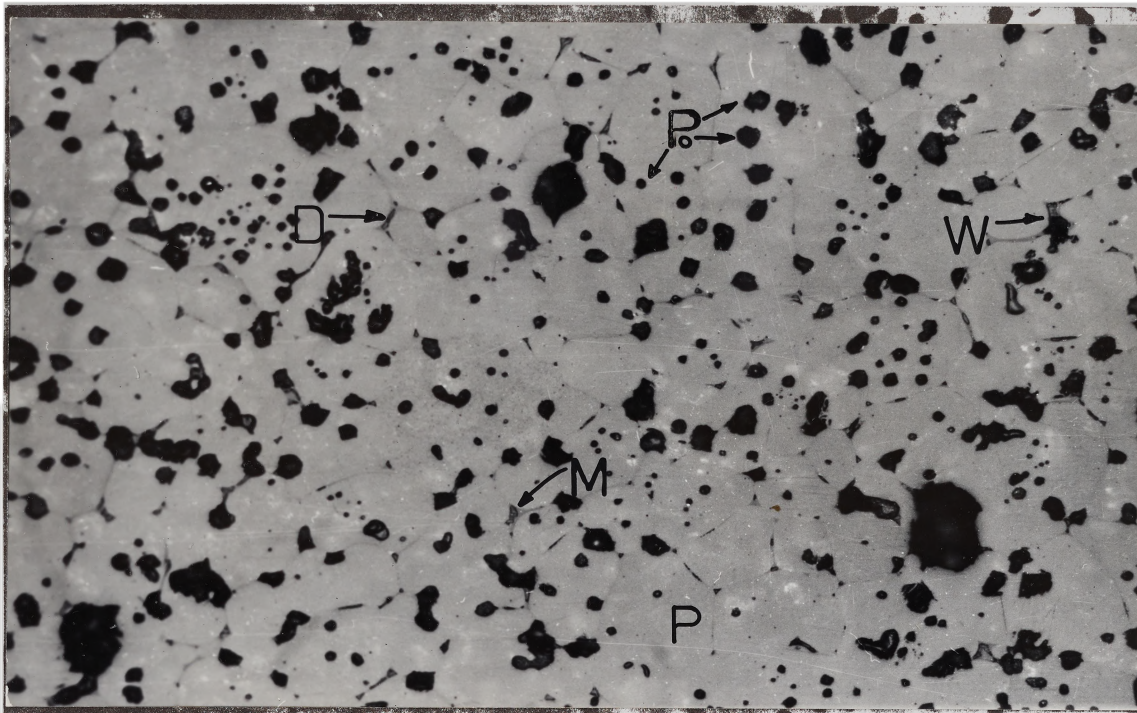(magnification of 240x).

Figure 33. Optical microscopy photograph for composition C
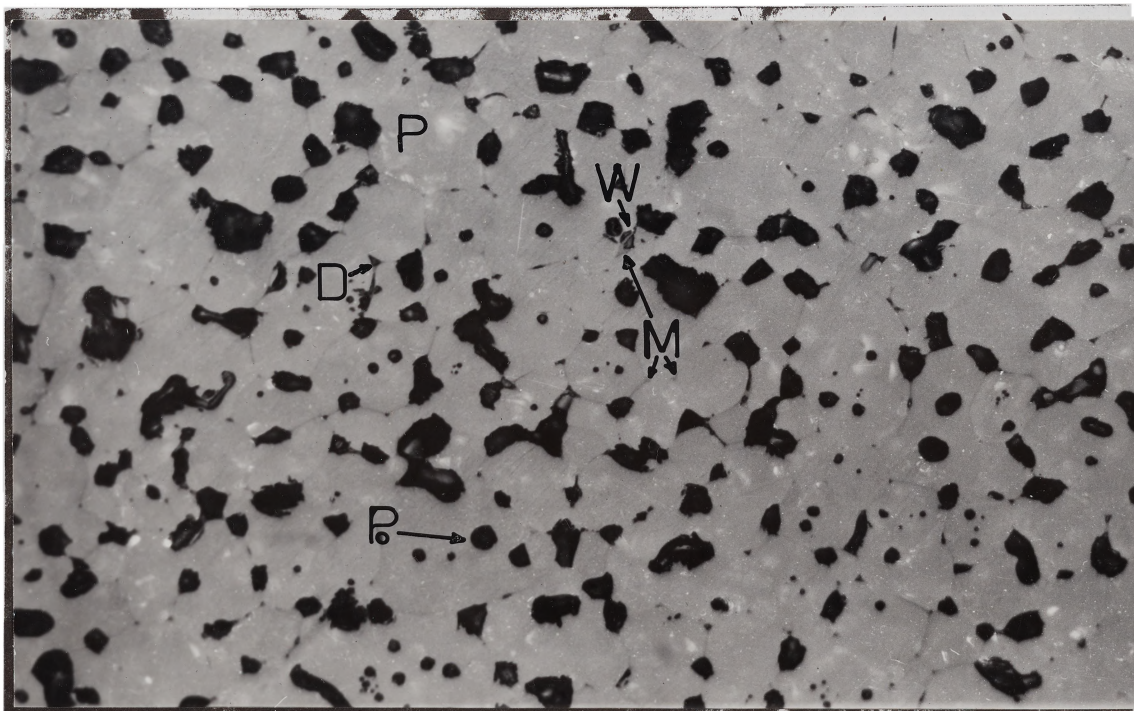fired at 1760°C for 57,600s in air (magnification
of 240x).

Figure 34. Optical microscopy photograph for composition C
fired at 1760°C for 57,600s in $P_{O_2} = 10^{-7}$ KPa
(magnification of 240x).

Figure 35.   Optical microscopy photograph for composition D
             fired at 1760°C for 57,600s in air (magnification
             of 240x).

Figure 36.   Optical microscopy photograph for composition D
             fired at 1760°C for 57,600s in P_{O_2} = 10^{-7} KPa
             (magnification of 240x).

Figure 37. Optical microscopy photograph for composition E
fired at 1760°C for 57,600s in air (magnification
of 240x).

Figure 38. Optical microscopy photograph for composition E
fired at 1760°C for 57,600s in $P_{O_2} = 10^{-7}$ KPa
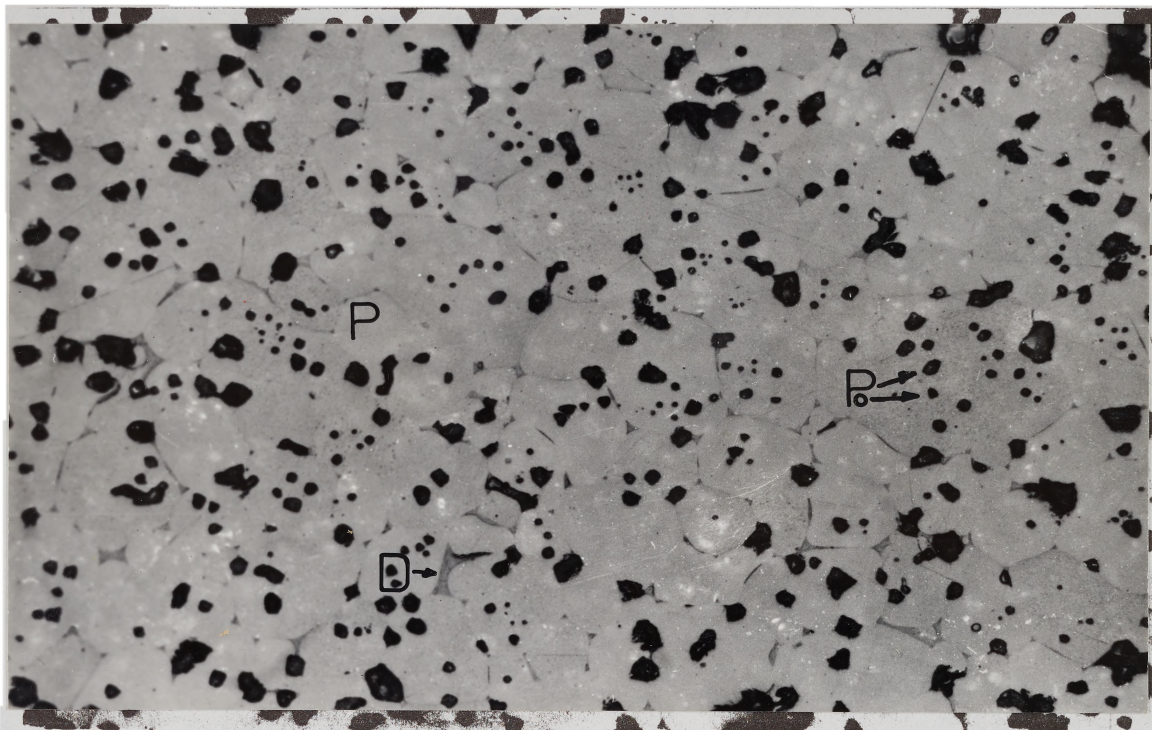(magnification of 240x).
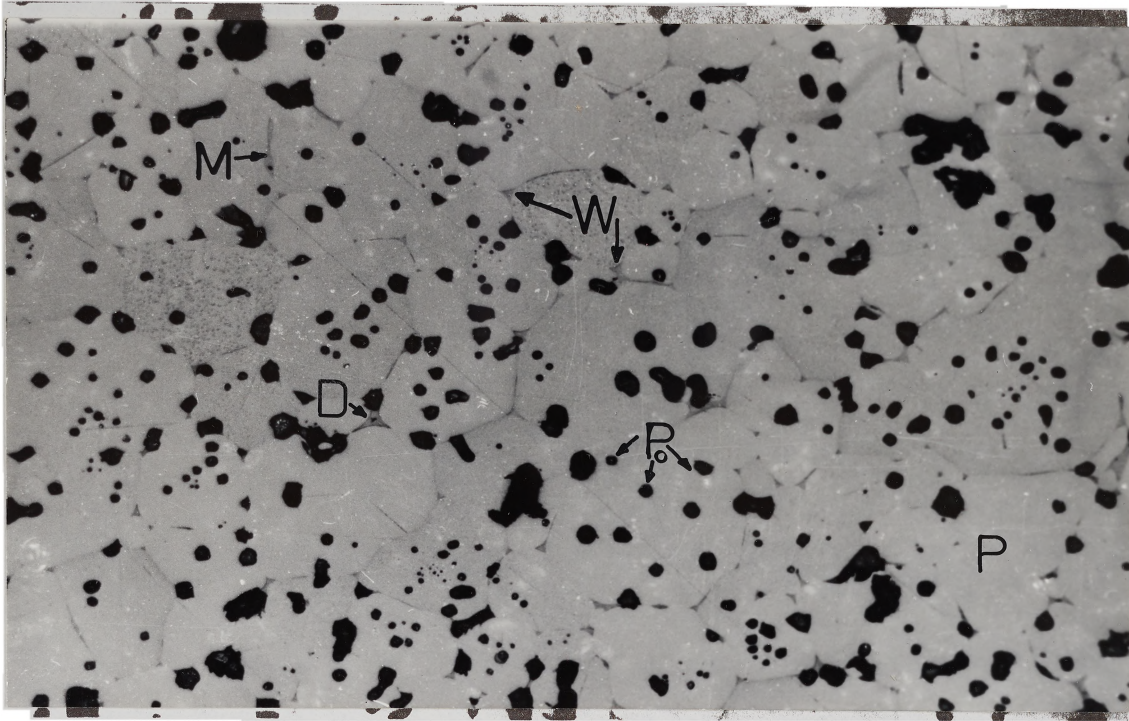
Figure 39. Optical microscopy photograph for composition F
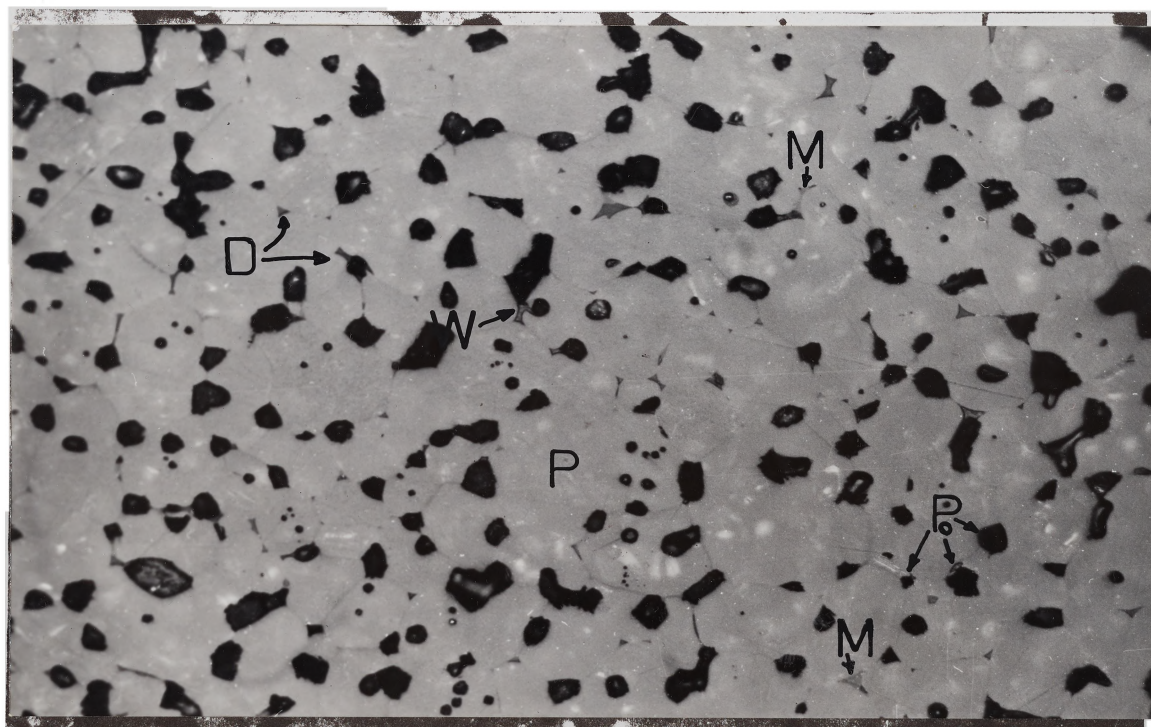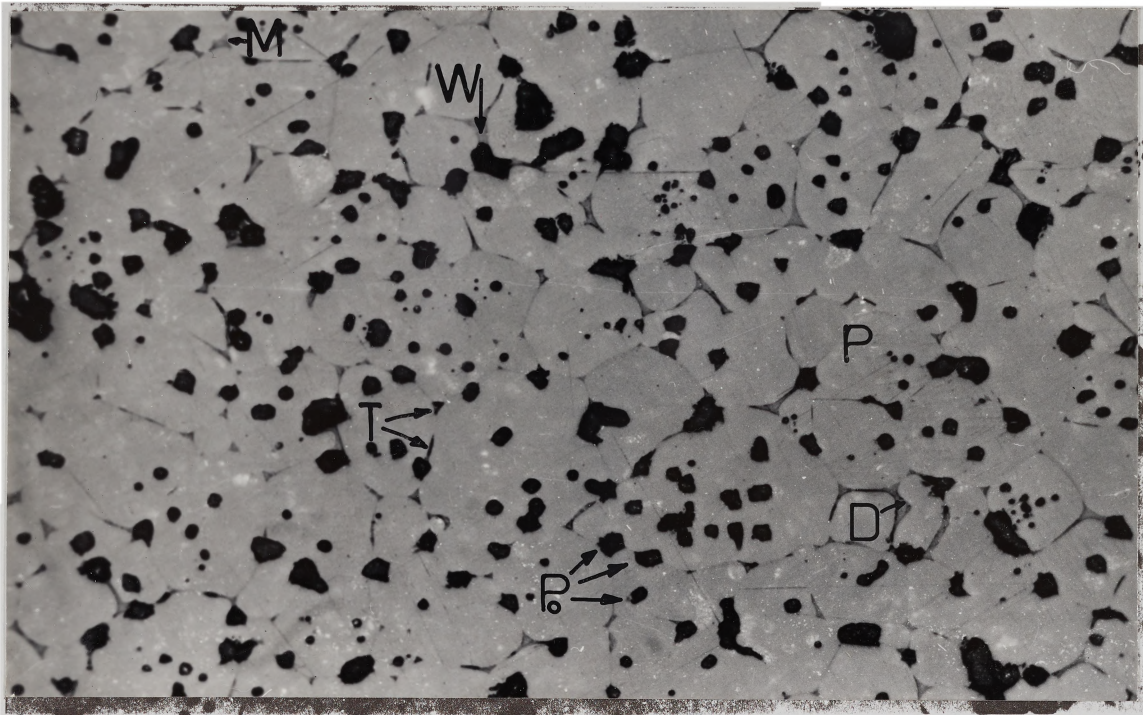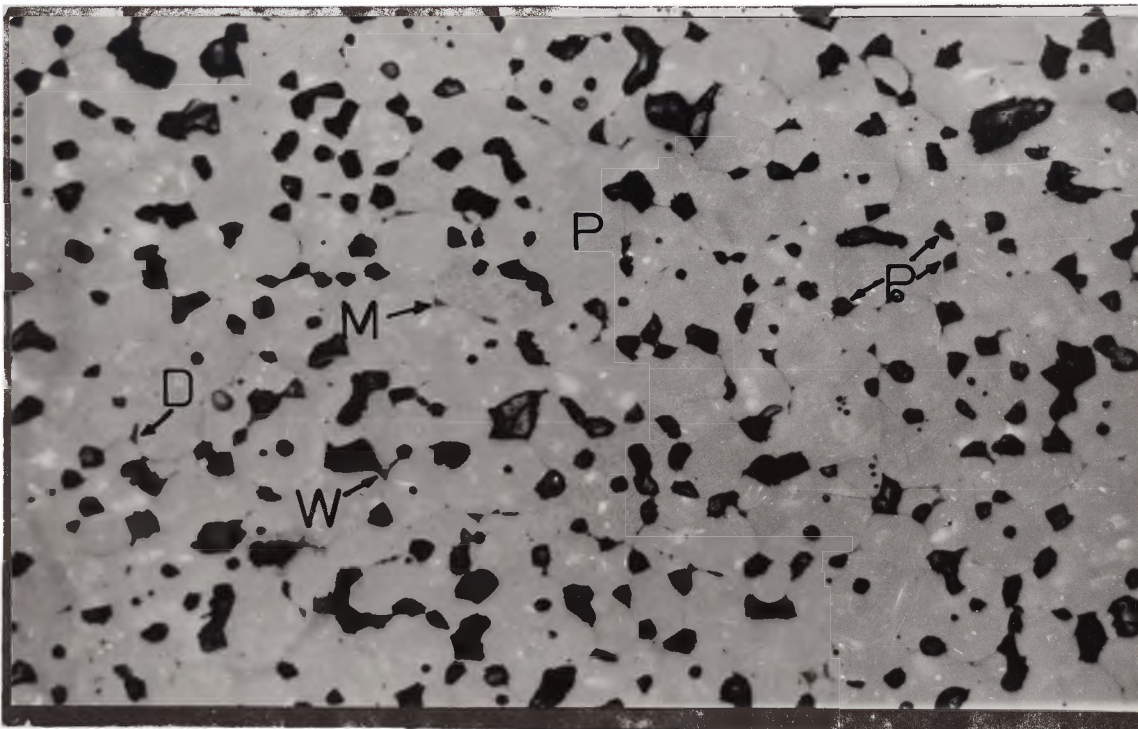fired at 1760°C for 57,600s in air (magnification
of 240x).
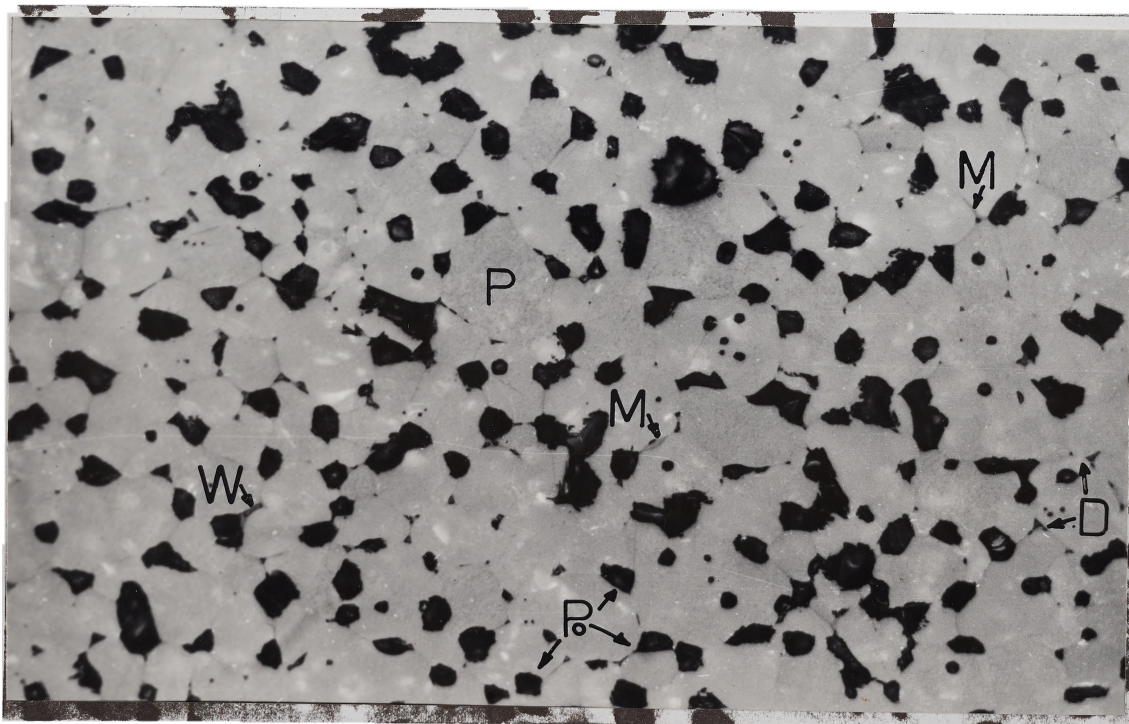
Figure 40. Optical microscopy photograph for composition F
fired at 1760°C for 57,600s in $P_{O_2} = 10^{-7}$ KPa
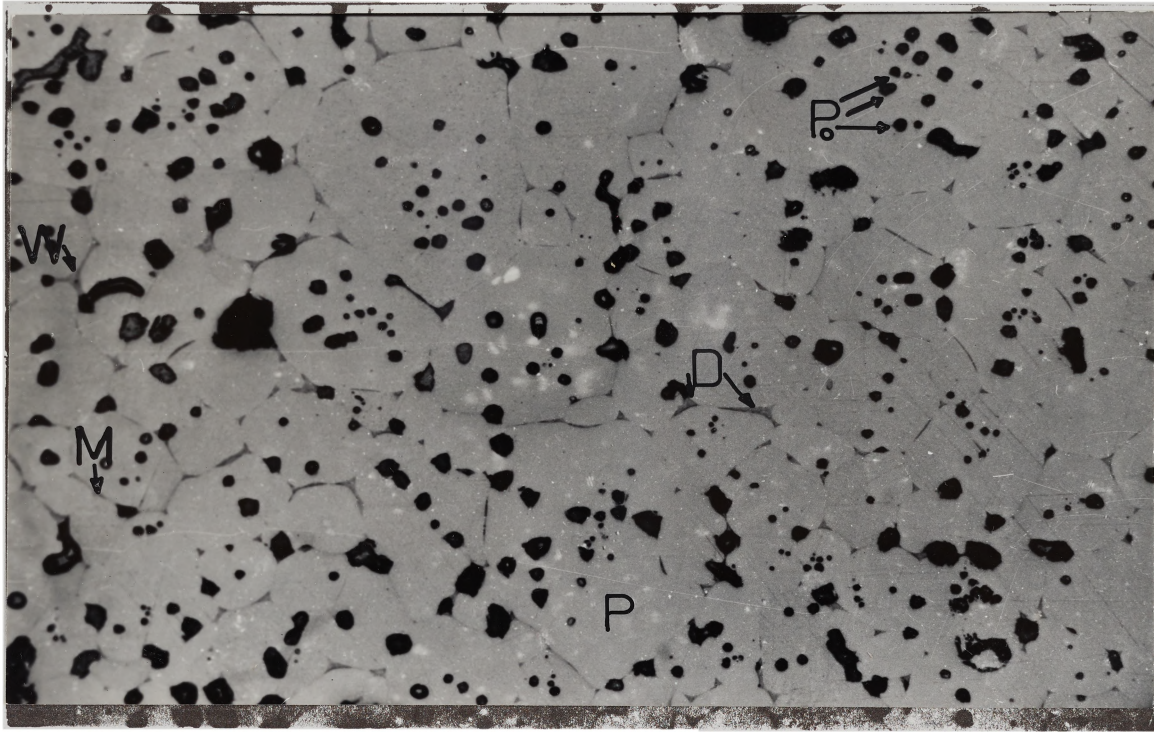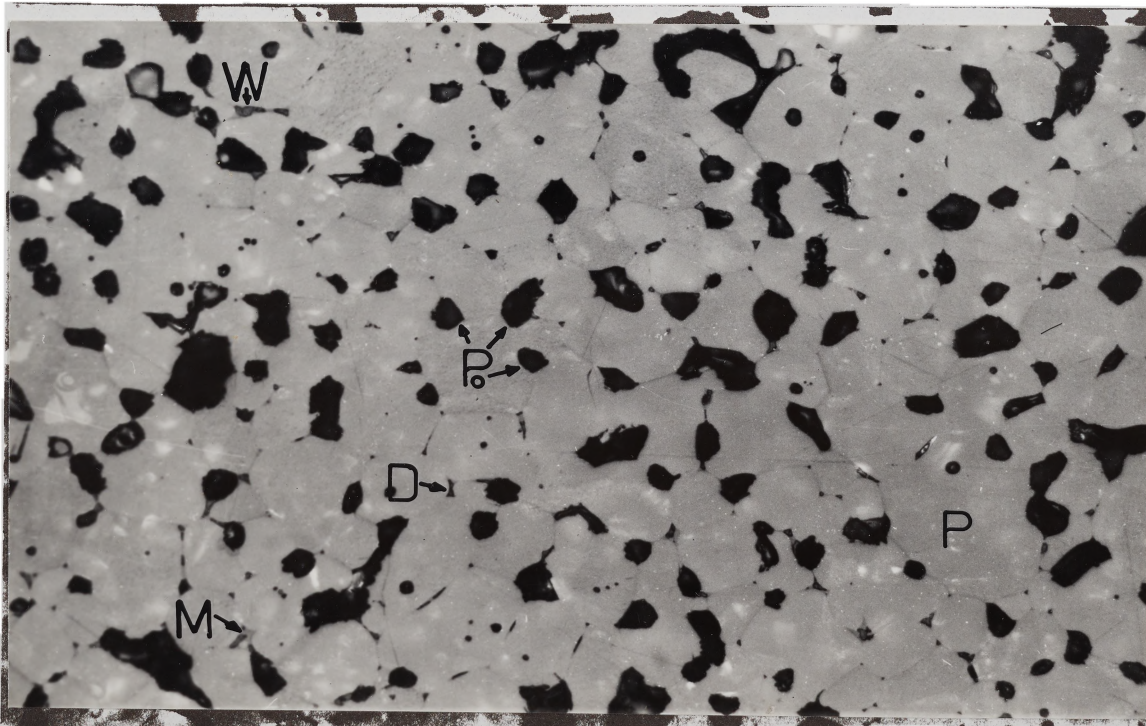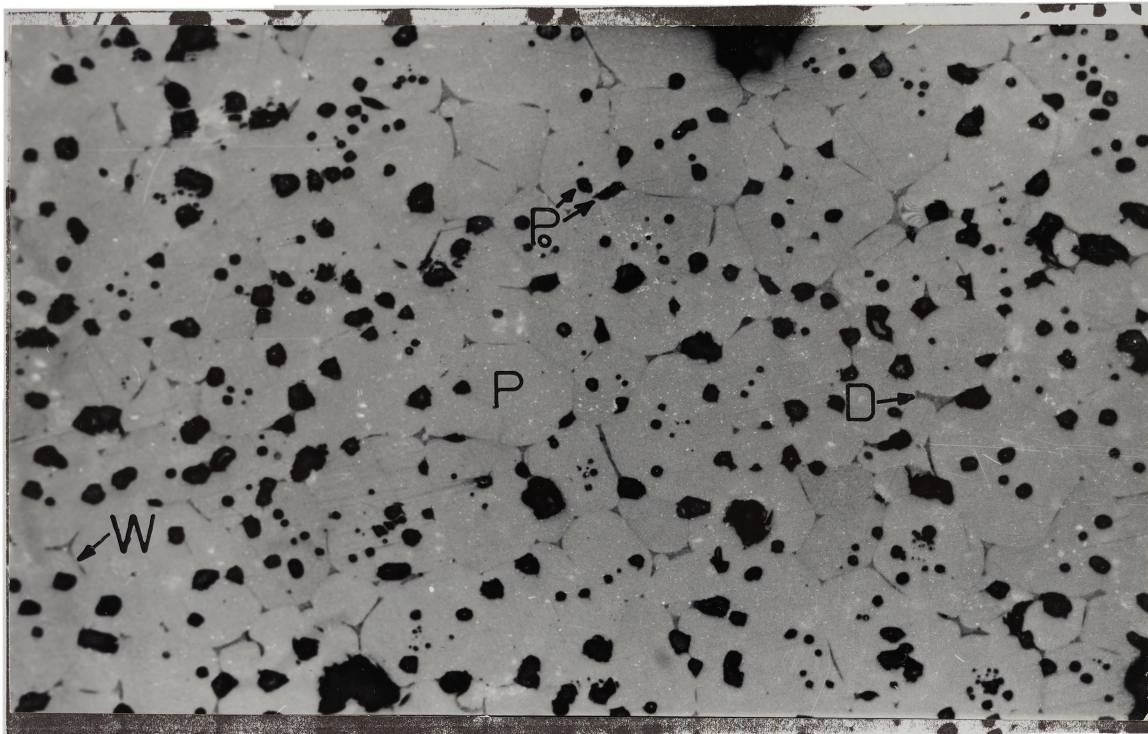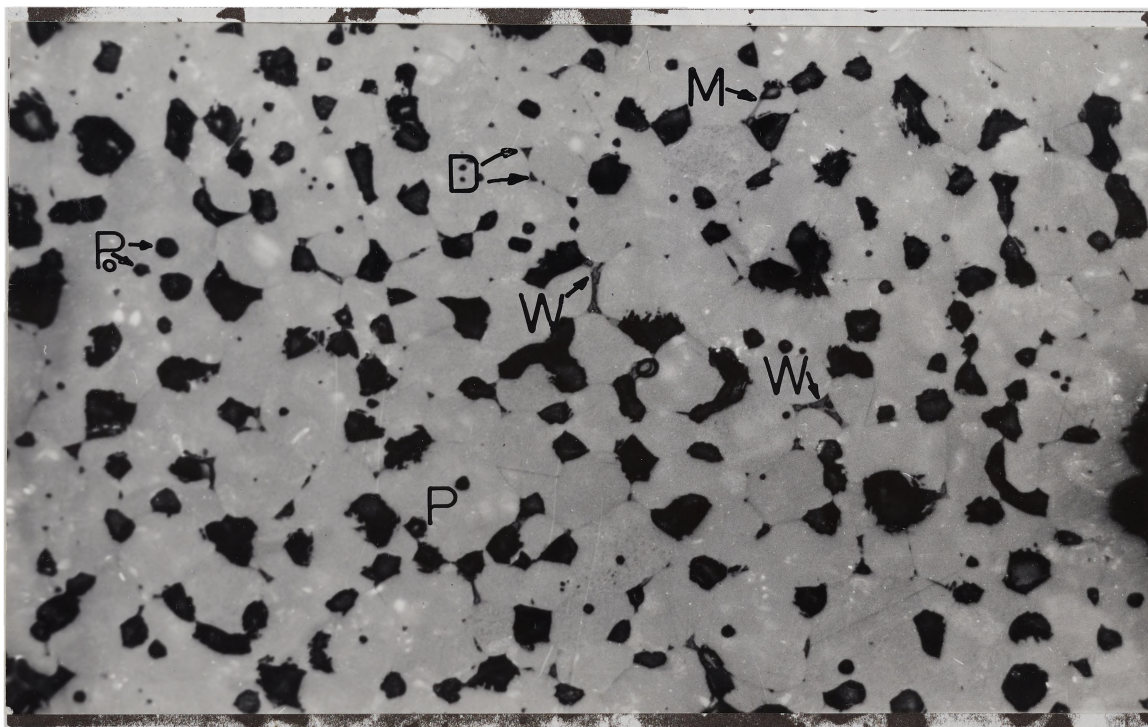(magnification of 240x).

In all cases the samples are constituted mineralog-
ically by periclase crystals as the major phase and by
the silicate C_2S as secondary phase. Minor amounts of
the silicates CMS, C_3MS_2 and C_3S were also found,
probably due to local heterogeneities in the samples.
A striking microstructural difference can be seen
between samples fired in air in comparison with samples
fired in reducing atmosphere. Samples fired in air
have lower porosity, smaller pore sizes, and better
polygonized crystals with higher direct periclase to
periclase bond. For both cases, the pores are essentially
closed and rounded, either intercrystalline or intra-
crystalline. A very small amount of phases of high
reflectivity of submicroscopic size, which were located
mainly at the grain boundaries of periclase crystals or
in association with the silicate phase, were observed
in both atmospheres. However, these highly reflective
phases are much less common for the samples fired in
air.

Grain size measurements (Table XVI) have shown that
grain growth occurs for all compositions fired at $1760^{\circ}C$.
The grain growth results for composition D are plotted
in Figure 41 and shows a behavior given by the equation
G^n = kt where n is equal to 3.1 for firing in air and
3.2 for firing in reducing atmosphere. It can also be
seen in Table XVI that while there exists a small increase

TABLE XVI

GRAIN SIZE (μm) MEASUREMENTS FOR SAMPLES FIRED AT 1760°C

Atmosphere	Time s x 10^{-4}	A	B	C	D	E	F
Air	0.36	-	-	-	30	-	-
	0.72	31	33	35	36	35	40
	1.44	-	-	-	48	-	-
	2.88	-	-	-	59	-	-
	5.76	63	68	66	70	71	73
$P_{O_2} = 10^{-7}$ KPa	0.36	-	-	-	26	-	-
	0.72	35	40	37	35	36	39
	1.44	-	-	-	43	-	-
	2.88	-	-	-	54	-	-
	5.76	66	64	59	63	66	58
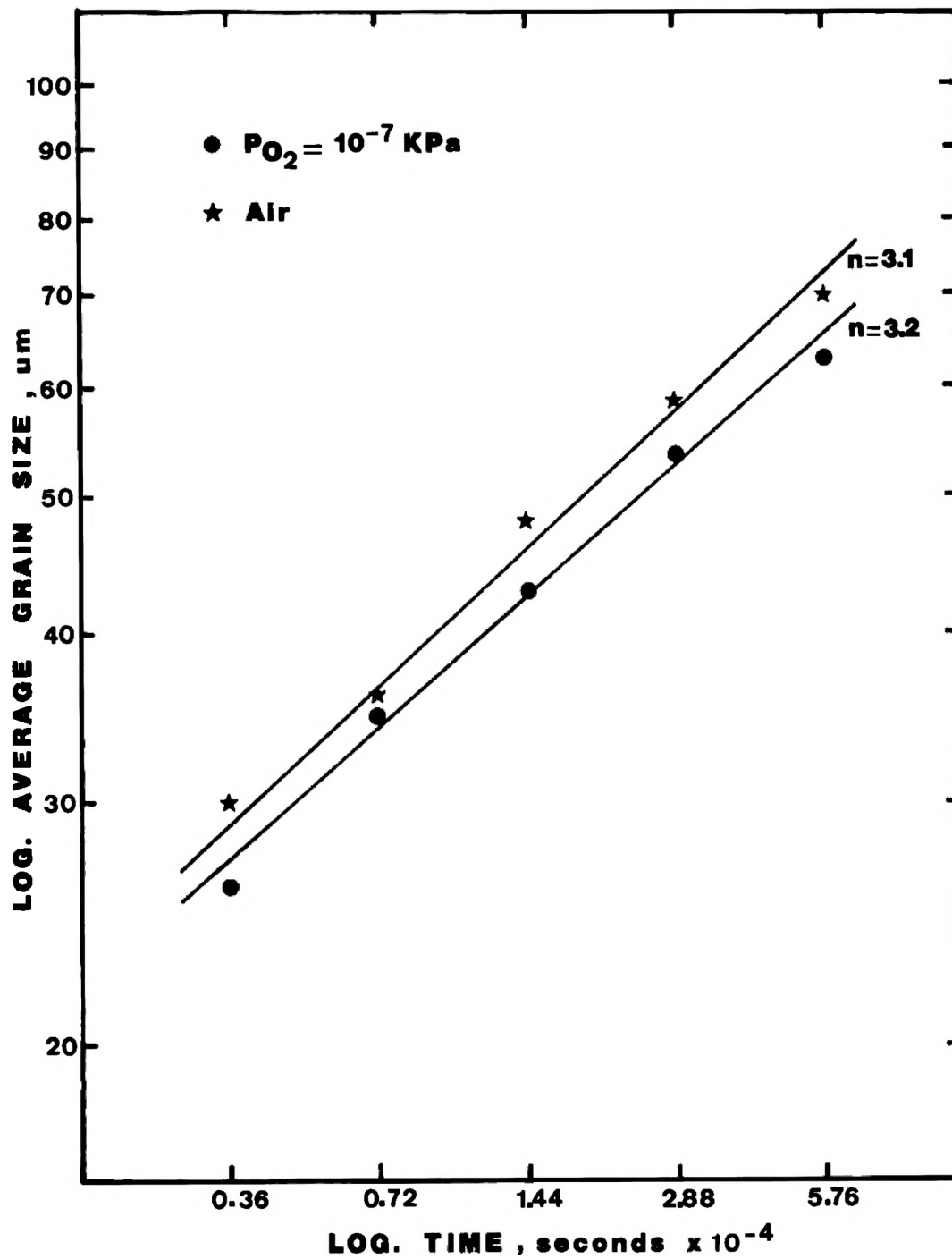
Figure 41. Average grain size diameter versus time of sintering at 1760°C for composition D (MnO = 1.50 wt.%).

in grain size with the increase in MnO concentration for samples fired in air, variable results were found for samples fired in reducing atmosphere.

The results obtained by using Electron Microprobe analysis are illustrated in photographs in Figures 42 to 49 for composition F fired in air, and in Figures 50 to 57 for composition F fired in $P_{O_2} = 10^{-7}$ KPa. Photographs for the other compositions are not shown because they are similar to the composition F with the only difference being the intensity decrease for Mn-mapping with the decrease in Mn concentration. Mapping of Fe and Mn shows that these elements have a homogeneous distribution throughout the microstructure, independent of the type of atmosphere. Calcium and Si are associated together around the MgO crystals. Calcium is present within the MgO lattice in small amounts, but Si is absent. Titanium, which is a minor impurity in the Brazilian magnesite, is distributed throughout the microstructure but also occurs in some small spots of high concentration always associated with the silicate phase. These spots rich in Ti have been identified as phases of high reflectivity.

The identification of spots rich in Ti as being a phase of high reflectivity could lead us to generalize that all phases of high reflectivity should be associated with the Ti phase. In this case, the phase
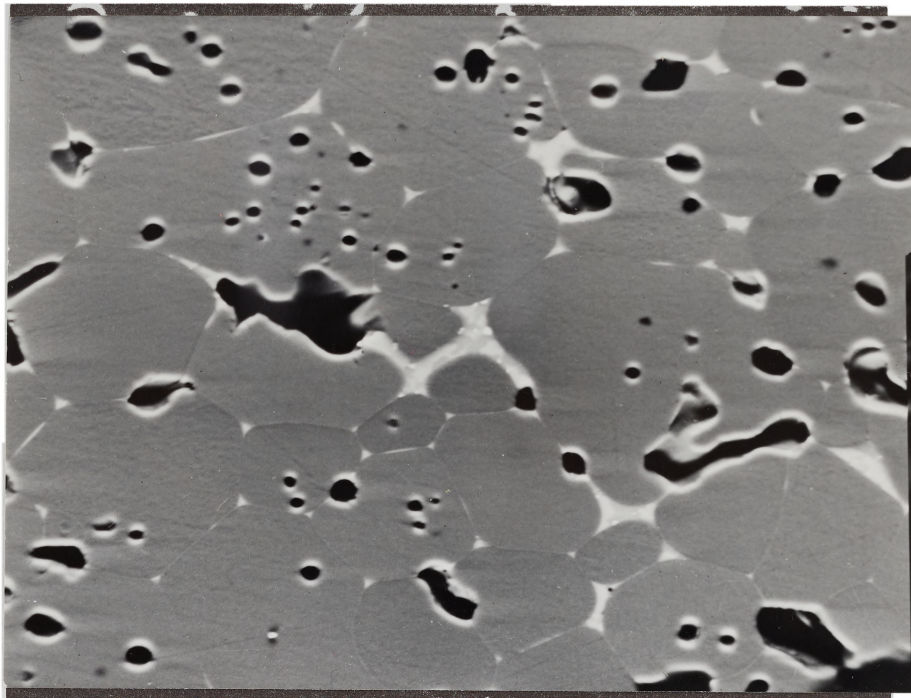
Figure 42. Electron microprobe photograph for composition F fired at 1760°C for 57,600s in air (magnification of 550x).
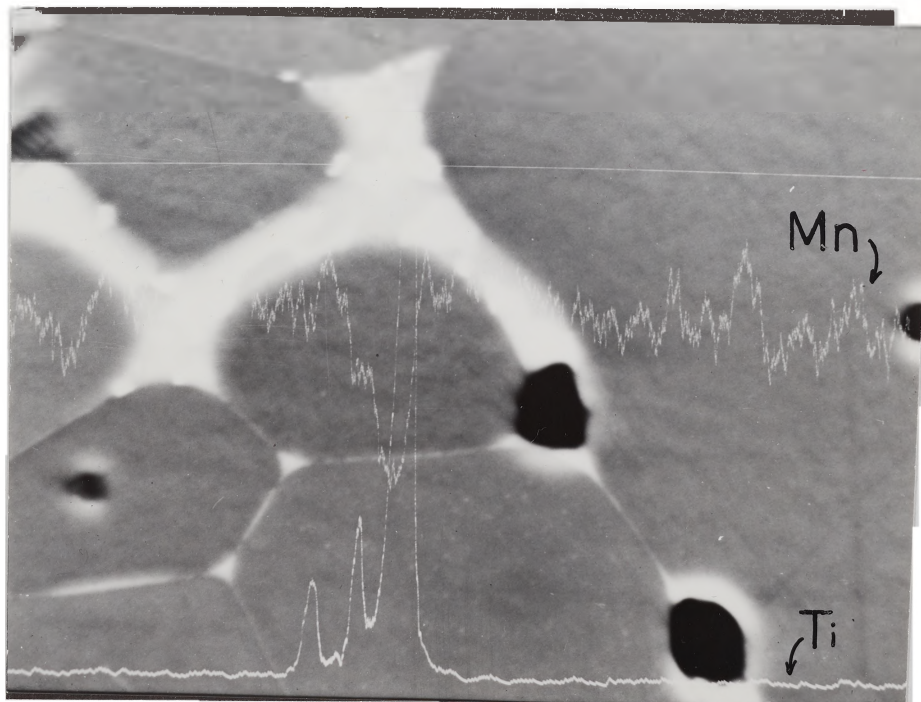
Figure 43. Increased magnification for electron microprobe photograph of the same area as Figure 42 (magnification of 1,800x).
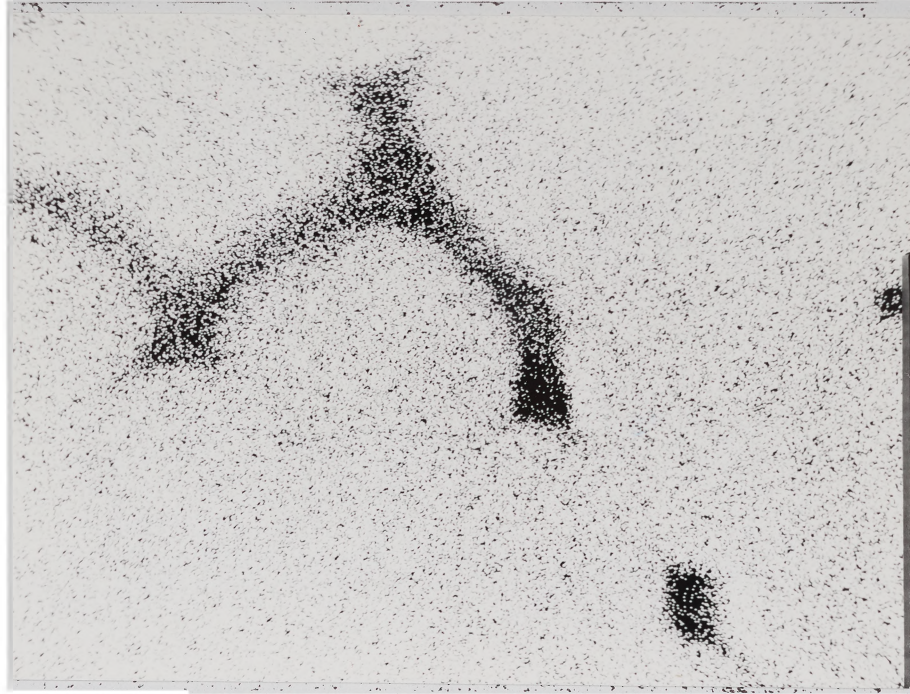
Figure 44. Magnesium x-ray image for the area in Figure 43
(magnification of 1,800x).
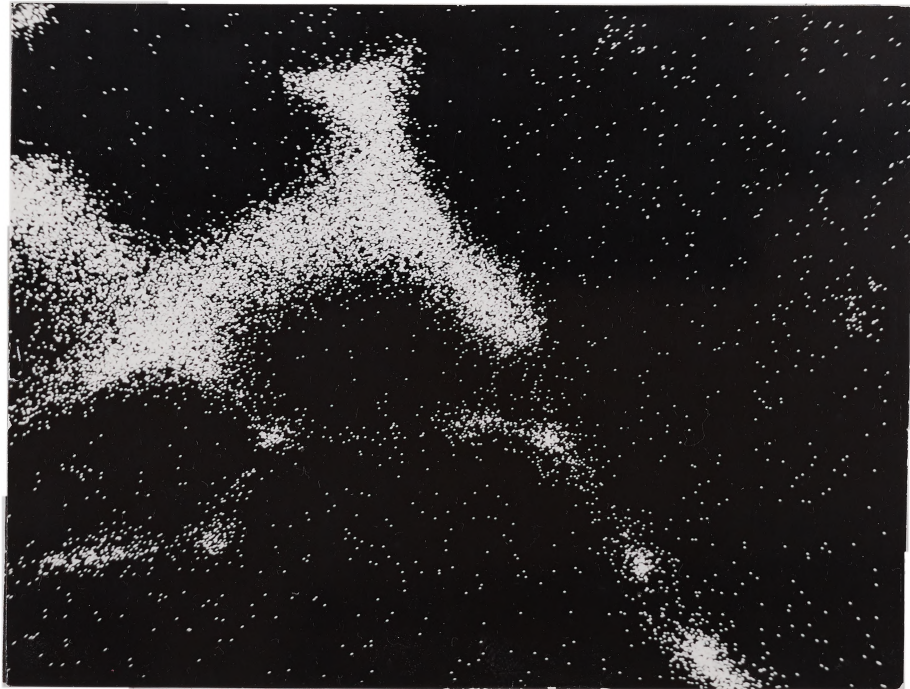
Figure 45. Calcium x-ray image for the area in Figure 43
(magnification of 1,800x).
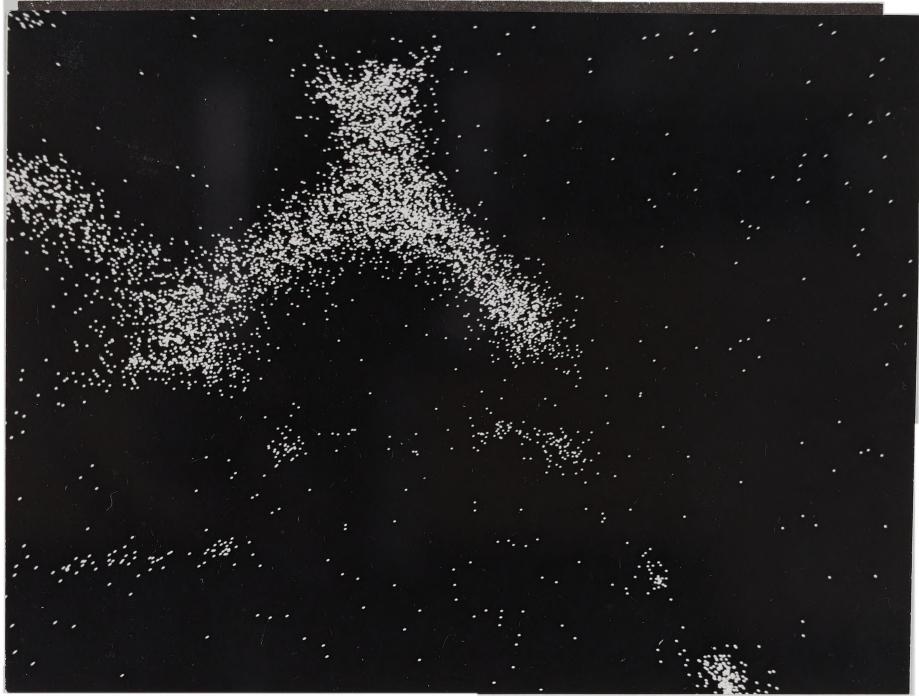
Figure 46.   Silicon x-ray image for the area in Figure 43
             (magnification ox 1,800x).

Figure 47.   Manganese x-ray image for the area in Figure 43
             (magnification of 1,800x).

Figure 48.   Iron x-ray image for the area in Figure 43
             (magnification of 1,800x).

Figure 49.   Titanium x-ray image for the area in Figure 43
             (magnification of 1,800x).
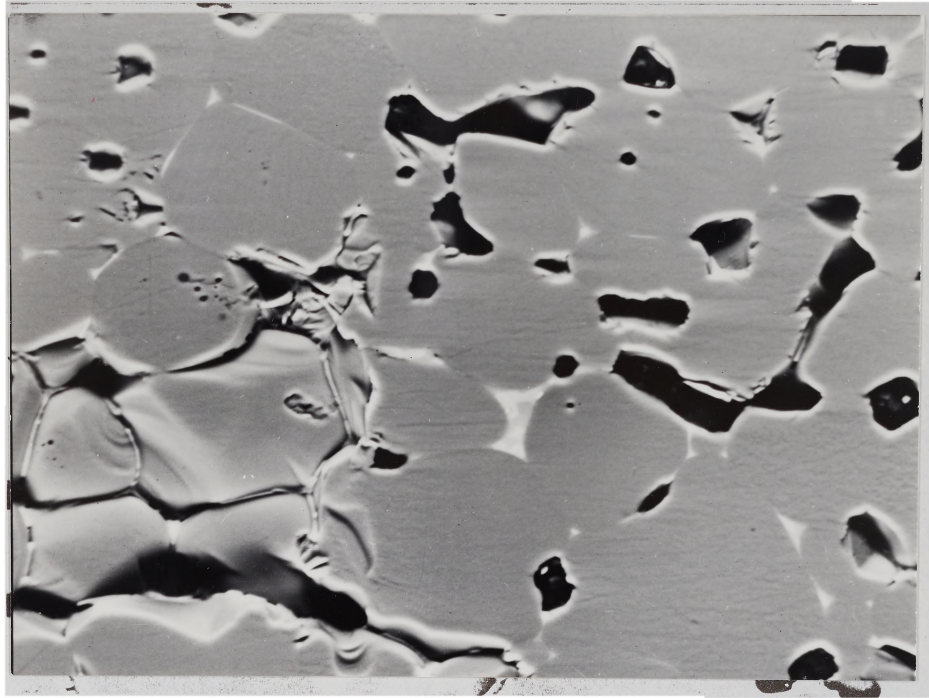
Figure 50. Electron microprobe photograph for composition F
fired at 1760°C for 57,600s in $P_{O_2} = 10^{-7}$ KPa
(magnification of 550x).
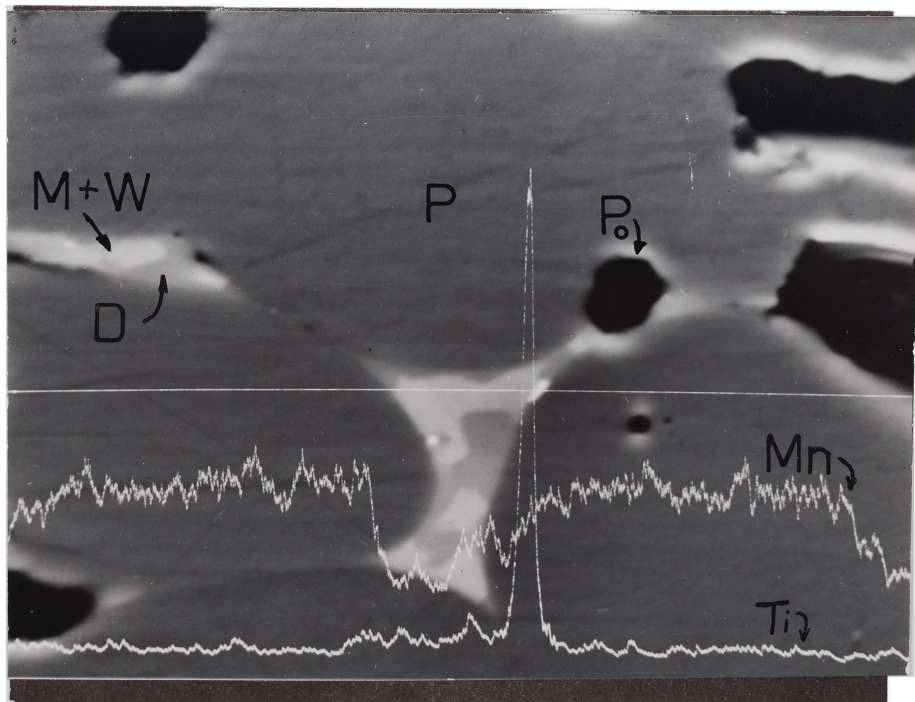
Figure 51. Increased magnification for electron microprobe
photograph of the same area in Figure 50 (magnification
of 1,800x).
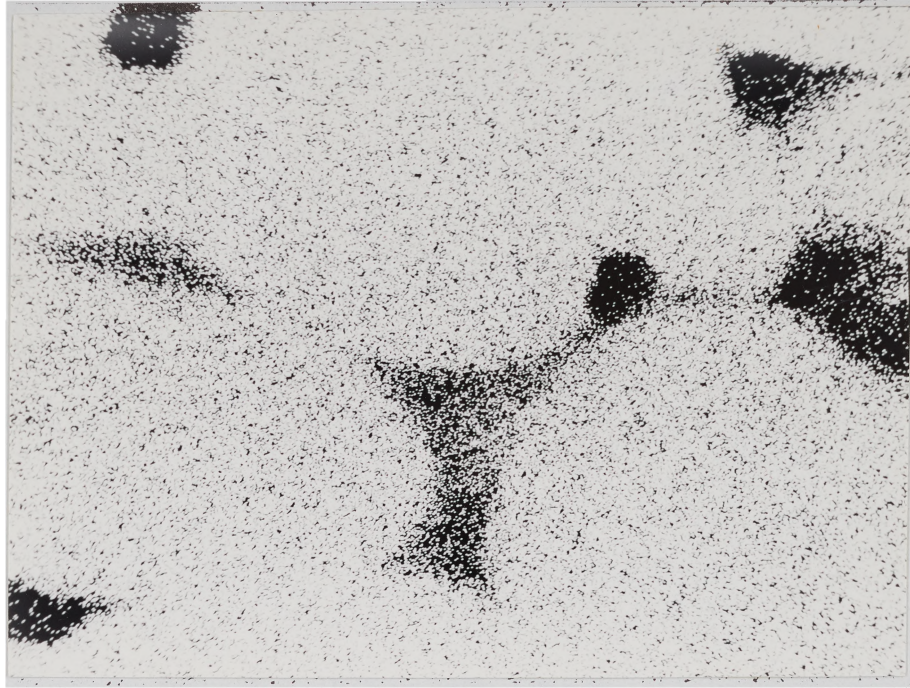
Figure 52.   Magnesium x-ray image for the area in Figure 51
             (magnification of 1,800x).
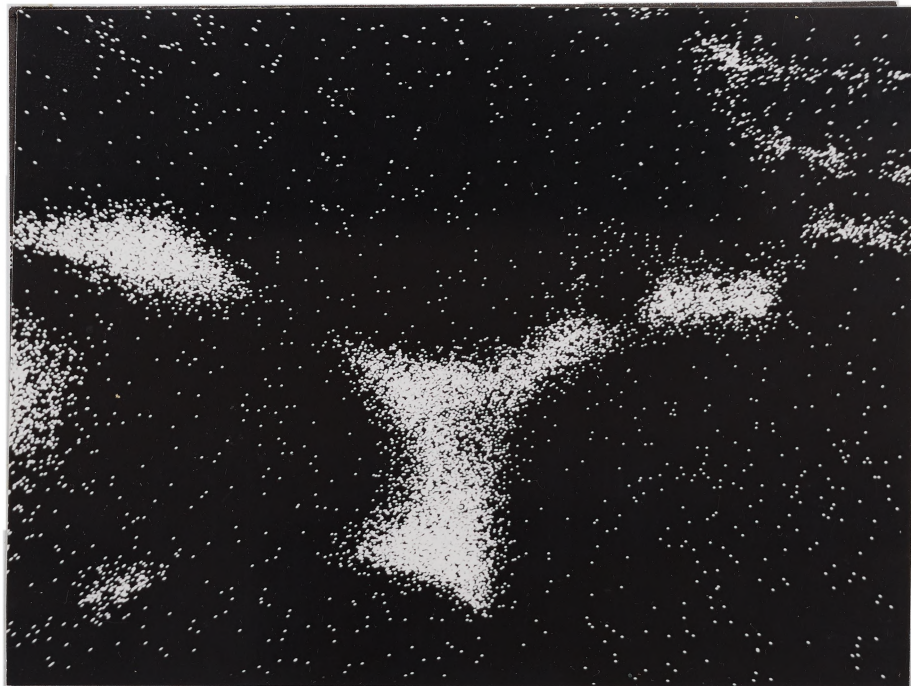
Figure 53.   Calcium x-ray image for the area in Figure 51
             (magnification of 1,800x).
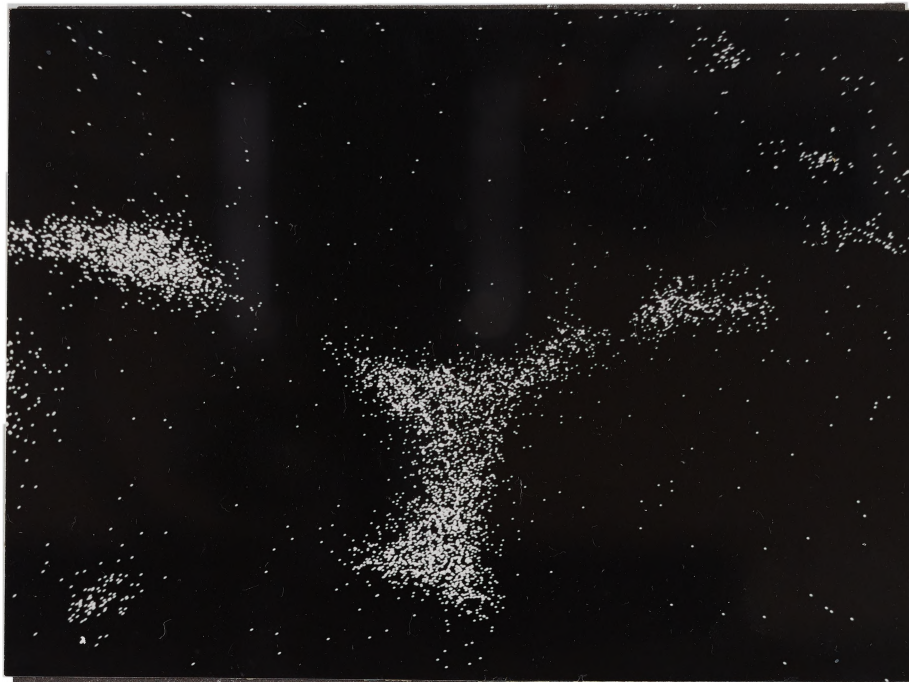
Figure 54.   Silicon x-ray image for the area in Figure 51
             (magnification of 1,800x).

Figure 55.   Manganese x-ray image for the area in Figure 51
             (magnification of 1,800x).

Figure 56.   Iron x-ray image for the area in Figure 51
             (magnification of 1,800x).
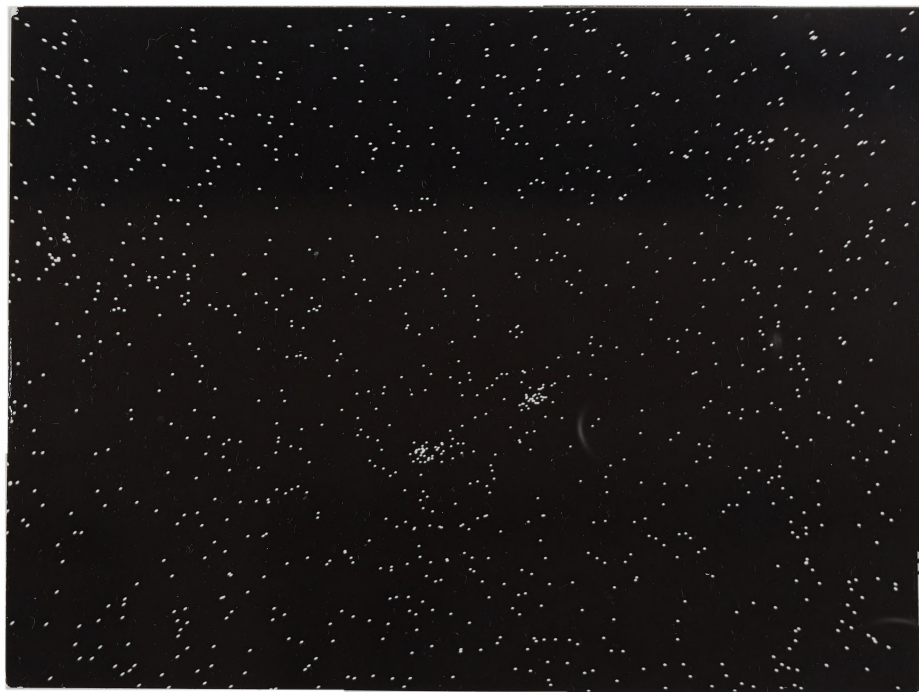
Figure 57.   Titanium x-ray image for the area in Figure 51
             (magnification of 1,800 x).

rich in Ti should be more stable in reducing atmosphere,
in order to explain their higher concentration for firing
in $P_{O_2} = 10^{-7}$ KPa. However, this seems not to be the
only explanation to the appearance of these phases of
high reflectivity. As discussed before, these high
reflectivity phases seem to be also associated with
formation of single crystals of MgO due to the evaporation-
condensation process which occurs in reducing conditions,
as illustrated in Figures 58 and 59. In this case,
their identification by using a "mapping technique"
with the electron microprobe is futile, because it is
not possible to distinguish between the intensity of
the Mg x-ray image coming from these phase crystals or
from the MgO grains themselves. Consequently, further
investigation will be necessary for the complete
identification of these phases.
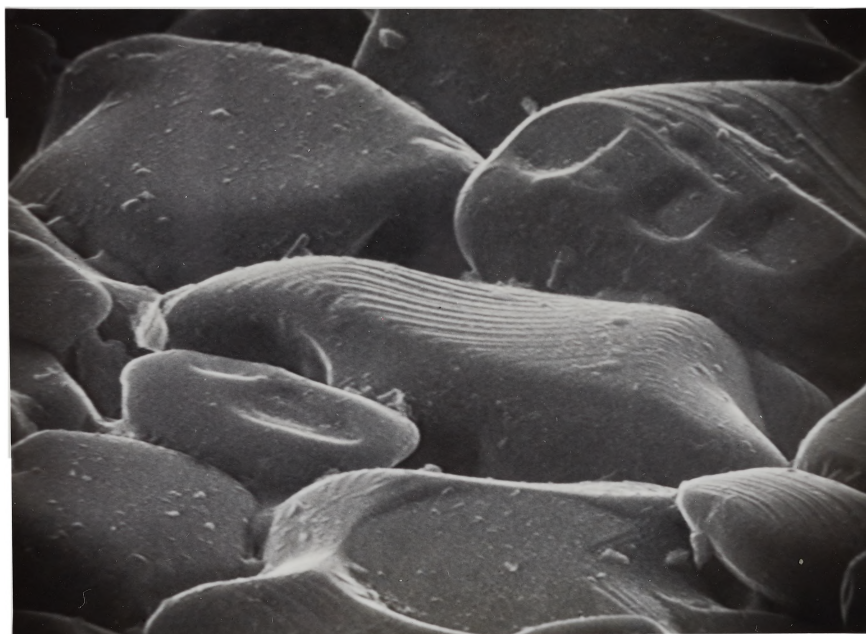
Figure 58. Scanning microphotograph showing formation of MgO
crystals by an evaporation-condensation process
(magnification of 1,500x).
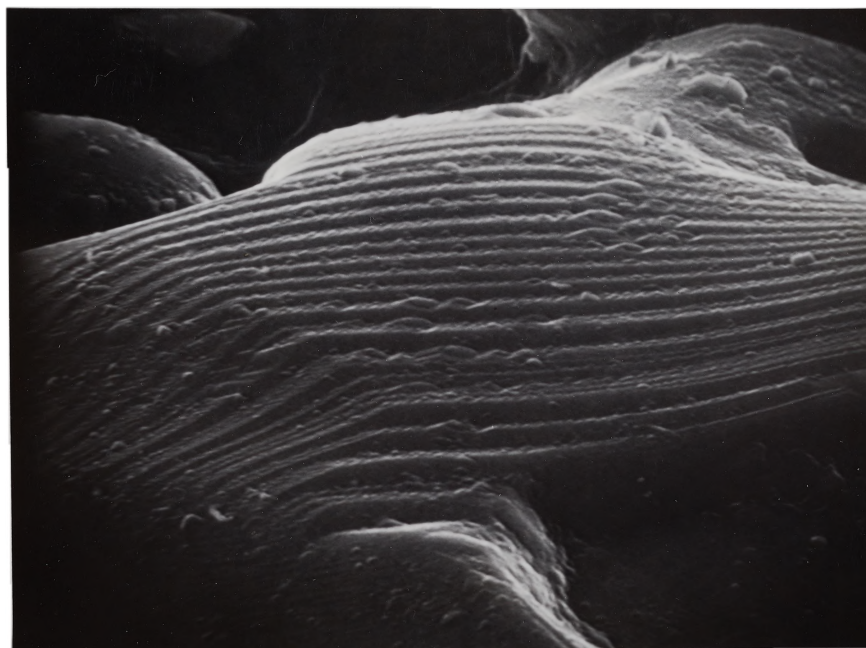
Figure 59. Increased magnification for scanning microphotograph
of the same area as Figure 58 (magnification of
3,500x).

VI. CONCLUSIONS

1. The addition of MnO up to a concentration of
    2.50 wt.% has a positive influence on densification
    of the Brazilian natural magnesite for samples
    sintered in air. In fact, for samples fired for
    3,600s in air at either 1700 or 1760°C, there is an
    increase of 80 Kg/m^3 in the bulk density for the
    sample containing 2.50 wt.% MnO over the sample
    containing 0.16 wt.% MnO. This fact seems to be
   associated with the increase in lattice diffusion of
    Mg ions due to the increase in vacancy concentration
    defects in the MgO lattice by the presence of Mn^{+3}.
    As Mg diffusion is thought to be rate limiting for
    the sintering process of MgO, an increase in the
    lattice diffusion of Mg causes an increase in the
    densification.

2. The addition of MnO for samples fired in reducing
    atmosphere of $P_{O_2} = 10^{-7}$ KPa at either 1700 or
    1760°C has shown no influence on the densification
    process. In these conditions, Mn is in plus two
    valence state and does not create extra vacancies
    by its diffusion into the MgO lattice, therefore
    the lattice diffusion of Mg and densification rate
    are unchanged.

3. Plots of percent total porosity and percent closed pores versus time of sintering and microstructure studies have shown that, for sintering temperatures of 1700 and 1760°C and times from 3,600 to 57,600s, the sintering process is at the end of the intermediate stage. Linear lines have been obtained by plotting data of percent theoretical density versus logarithm of time, an empirical relationship which is often used to correlate data in the intermediate stage sintering.

4. The logarithmic dependence of time for the densification process shows that long times are not very effective in increasing bulk densities of MgO. In fact, sintering at 1760°C for 7,200s in air, shows bulk densities going from 3,210 Kg/m^3 for composition A (0.16 wt.% MnO) to 3,280 Kg/m^3 for composition F (2.50 wt.% MnO), while sintering for 57,600s causes an average additional increase of only 70 Kg/m^3. A similar behavior occurs for samples fired at 1760°C under reducing atmosphere of $P_{O_2} = 10^{-7}$ KPa, where the bulk densities are, on the average, 3,130 Kg/m^3 for 7,200s of sintering and an additional average increase of only 60 Kg/m^3 is found for 57,600s of sintering.

5. Most of the difference in densification between samples fired in air versus samples fired under atmosphere of $P_{O_2} = 10^{-7}$ KPa occurred during heat up and up to 3,600s of sintering.

6. Another very important technological aspect is the relative importance of temperature and time on the densification of MgO grain, for the range of temperature and time being investigated. On the average, 7,200s of sintering at 1760°C in air, causes the same densification that 32,400s of sintering at 1700°C in air.

7. Studies on the influence of temperature ranging from 1520° to 1760°C on densification of MgO grain, have shown that samples fired in air for 57,600s follow a very simple behavior, with a gradual increase in bulk densities with increasing temperature. Samples fired in reducing atmosphere of $P_{O_2} = 10^{-7}$ KPa follow a similar behavior in the range of 1520 to 1640°C, but they have a discontinuity in the temperature range 1640°C to 1700°C, in which a small decrease in bulk density occurs. The decrease in density seems to be mostly associated with the increase in vapor pressure of Mg for temperatures higher than 1640°C.

8. In summary, these investigations have shown that
    atmosphere has an important influence on densification
    of MgO grain doped with MnO. Manganese oxide aids
    densification under oxidizing atmosphere but has
    no effect under reducing conditions. Moreover,
    for the range of temperature and time investigated,
    temperature is more effective on densification
    than time. For better densification, therefore, it
    is necessary to fire at high temperatures, under
    oxidizing conditions, and not necessarily for long
    times.

BIBLIOGRAPHY

1. D.R.F. Spencer, "Basic Refractory Raw Materials", Trans. Brit. Ceram. Soc., 71[5], 123-134 (1972).

2. R.J. Hall and D.R.F. Spencer, "A Review of the Production and Properties of Sea-Water Magnesia", Interceram, 22[3], 212-218 (1973).

3. J.H. Chester, "Refractories: Production and Properties", The Iron and Steel Institute, London (1973).

4. W.S. Treffner, "Microstructure of Periclase", J. Am. Ceram. Soc., 47[8], 401-409 (1964).

5. D.G. Jones and D.A. Melford, "Comparison of the High-Temperature Constitution of Sea-Water Magnesites with that of Natural Greek Material", Trans. Brit. Ceram. Soc., 68[5], 241-247 (1969).

6. J. White, "High Temperature Oxides; Part I: Magnesia, Lime and Chrome Refractories", Edited by A.M. Alper, Academic Press, New York (1970).

7. M.I. Taylor, W.F Ford, and J. White, "Phase Relationships in Sections of the System $CaO-MgO-B_2O_3-SiO_2$ Relevant to Magnesite Refractories Containing B_2O_3", Trans. Brit. Ceram. Soc., 70[2], 51-56 (1971).

8. I. Menezes, "Dense Periclase Sinter of a Brazilian Natural Magnesite", I Seminario Latino Americano de Refratarios para a Industria Siderurgica - ILAFA-ALAFAR, Monterrey, Mexico (1971).

9. I. Menezes, "Raw Materials for Basic Refractories", XVII Congresso Brasileiro de Ceramica, Salvador, Brazil (1973).

10. I. Menezes and G.E. Goncalves, "Basic Refractories Produced with Brazilian MgO Sinters", VI Congresso da ALAFAR, Salvador, Brazil (1976).

11. H.U. Anderson, "The Sintering Phenomenon as Related to Oxides", Eighth Annual Symposium on Refractories, St. Louis Section of the American Ceramic Society, St. Louis (1972).

12. R.L. Coble and J.E. Burke, "Sintering in Ceramics", in Progress in Ceramic Science, Vol. 3, Edited by J.E. Burke, The Macmillan Company, New York (1963).

13. W.D. Kingery, "Introduction to Ceramics", 2nd edition, John Wiley & Sons, New York (1976).

14. J.E. Burke, "Role of Grain Boundaries in Sintering", J. Am. Ceram. Soc., 40[3], 80-85 (1957).

15. W.D. Kingery and M. Berg, "Study of the Initial Stages of Sintering Solids by Viscous Flow, Evaporation-Condensation, and Self Diffusion", J. Appl. Phys., 26[10], 1205-1212 (1955).

16. R.L. Coble, "Sintering Crystalline Solids. I. Intermediate and Final State Diffusion Models", J. Appl. Phys., 32[5], 787-792 (1961).

17. R.L. Coble, "Sintering Crystalline Solids. II. Experimental Test of Diffusion Models in Powder Compacts", J. Appl. Phys., 32[5], 793-799 (1961).

18. R.L. Coble, "Intermediate-Stage Sintering: Modification and Correction of a Lattice-Diffusion Model", J. Appl. Phys., 36[7], 2327 (1965).

19. D.L. Johnson, "Fundamentals of the Sintering of Ceramics", in Materials Science Research, Vol. 11, Edited by H. Palmour III, R.F. Davis and T.M. Hare, Published by Plenum Press, New York (1977).

20. G.C. Kuczynski, "Theory of Solid State Sintering", in Powder Metallurgy, edited by W. Lezynsky; Interscience Publishers, New York (1960).

21. G.C. Kuczynski, "Self-Diffusion in Sintering of Metallic Particles", Trans. AIME, 185[2], 169-179 (1949).

22. R.L. Coble, "Initial Sintering of Alumina and Hematite", J. Amer. Ceram. Soc., 41[2], 55-62 (1958).

23. D.L. Johnson and I.B. Cutler, "Diffusion Sintering:
    I. Initial Stage Sintering Models and Their
    Application to Shrinkage of Powder Compacts",
    J. Am. Ceram. Soc., 46[11], 541-545 (1963).

24. W. Beere, "The Intermediate Stage of Sintering",
    Vacancies '76, Edited by R.E. Smallman and
    J.E. Harris, The Metals Society, London (1977).

25. R.L. Coble and T.K. Gupta, "Intermediate Stage
    Sintering", in Sintering and Related Phenomena,
    Edited by G.C. Kuczynski, N.A. Hooton and
    C.F. Gibbon; Gordon and Breach Science Publishers,
    New York (1967).

26. D.L. Johnson, "A General Model for the Intermediate
    Stage of Sintering", J. Am. Ceram. Soc., 53[10],
    574-577 (1970).

27. P.J. Jorgensen, "Modification of Sintering
    Kinetics by Solute Segregation in Al_2O_3",
    J. Am. Ceram. Soc., 48[4], 207-210 (1965).

28. C.A. Bruch, "Sintering Kinetics for the High
    Density Alumina Process", Am. Ceram. Soc. Bull.,
    41[12], 799-806 (1962).

29. T.K. Gupta and R.L. Coble, "Sintering of ZnO:
    I, Densification and Grain Growth", J. Am. Ceram.
    Soc., 51[9], 521-525 (1968).

30. T.K. Gupta and R.L. Coble, "Sintering of ZnO: II, Density Decrease and Pore Growth During the Final Stage of the Process", J. Am. Ceram. Soc., 51[9], 525-528 (1968).

31. M. Paulus, "Relationship Between Densification, Crystal Growth, and Mechanisms of Formation in Ceramics", in Sintering and Related Phenomena, Materials Science Research, Vol. 6, Edited by G.C. Kuczynski, New York (1973).

32. J.H. Rosolowski and C. Greskovich, "Theory of the Dependence of Densification on Grain Growth During Intermediate-Stage Sintering", J. Am. Ceram. Soc., 58[5-6], 177-182 (1975).

33. R.A. Brown, "Sintering in Very Pure Magnesium Oxide and Magnesium Oxide Containing Vanadium", Am. Ceram. Soc. Bull., 44[6], 483-487 (1965).

34. T.K. Gupta, "Sintering of MgO: Densification and Grain Growth", J. Mat. Sci., 6[1], 25-32 (1971).

35. W. Beere, "The Second Stage Sintering Kinetics of Powder Compacts", Acta Met., 23[1], 139-145 (1975).

36. W. Beere, "The Intermediate Stage of Sintering", Metal Science, [8], 294-296 (1976).

37. R.L. Coble, "Progress in Sintering Theory", in Sintering and Related Phenomena, Materials Science Research, Vol. 6, Edited by G.C. Kuczynski, New York (1973).

38. I.B. Cutler, "Sintered Alumina and Magnesia", in High Temperature Oxides, Vol. 5-III, Edited by A.M. Alper, Academic Press, New York (1970).

39. W.R. Eubank, "Calcination Studies of Magnesium Oxide", J. Am. Ceram. Soc., 34[8], 225-229 (1951).

40. A. Pande and R. Singh, "Electron Microscope and Electron Diffraction Studies of Sintering of Magnesite", J. Am. Ceram. Soc., 41[10], 394-96 (1958).

41. P.W. Clark and J. White, "Some Aspects of Sintering", Trans. Brit. Ceram. Soc., 49[7], 305-333 (1950).

42. A.G. Allison, E.C. Sesler Jr., L. Haldy, and W.H. Ducworth, "Sintering of High-Purity Magnesia", J. Am. Ceram. Soc., 39[4], 151-154 (1956).

43. J.F. Quirk, "Factors Affecting Sinterability of Oxide Powders: BeO and MgO", J. Am. Ceram. Soc., 42[4], 178-81 (1959).

44. L.L. Hench, "Sintering and Reactions of MgO and CrO_3", Ph.D. Dissertation, Ohio State University (1964).

45. V.D. Skivis, "Dead-Burned Magnesia From an Ontario Magnesite Concentrate", Am. Ceram. Soc. Bull., 48[7], 724-728 (1969).

46. L.M. Atlas, "Effect of Some Lithium Compounds on Sintering of MgO", J. Am. Ceram. Soc., 40[6], 196-199 (1957).

47. J.W. Nelson and I.B. Cutler, "Effect of Oxide Additions on Sintering of Magnesia", J. Am. Ceram. Soc., 41[10], 406-409 (1958).

48. G.K. Layden Jr., "The Effect of Minor Additions on the Sintering of Magnesium Oxide", Master Thesis, The Pennsylvania State University (1959).

49. G.K. Layden and M.C. McQuarrie, "Effect of Minor Additions on Sintering of MgO", J. Am. Ceram. Soc., 42[2], 89-92 (1959).

50. H.J.S. Kriek, W.F. Ford, and J. White, "The Effect of Additions on the Sintering and Dead-Burning of Magnesia", Trans. Brit. Ceram. Soc., 58[1], 1-34 (1959).

51. D.R.F. Spencer and D.S. Coleman, "Sintering Behavior of Pure Magnesia with Additions from the $CaO-MgO-SiO_2$ System", in Science of Ceramics, Edited by C. Brosset and E. Knopp; Swedish Institute for Silicate Research (1970).

52. J.T. Jones, P.K. Maitra, and I.B. Cutler, "Role of Structural Defects in the Sintering of Alumina and Magnesia", J. Am. Ceram. Soc., 41[9], 353-357 (1958).

53. G.E. Jungquist, "Final Sintering of Cr_2O_3 with Minor Additions of MgO and Sintering of MgO with Minor Additions of Cr_2O_3", Master Thesis, University of Missouri-Rolla (1971).

54. L.L. Hench and R. Russel Jr., "Effect of Cr_2O_3 Vaporization on the Sintering of MgO", Trans. Brit. Ceram. Soc., 67[9], 377-89 (1968).

55. J. Barta and J. Gorni, "Direct Conversion of $Mg(OH)_2$ to High-Density Periclase", Trans. Brit. Ceram. Soc., 67[2], 57-67 (1968).

56. P.J. Anderson and P.L. Morgan, "Effect of Water Vapor on Sintering of MgO", Trans. Faraday Soc. 60[5], 930-937 (1964).

57. P.J. Anderson, R.E. Horlock and J.F. Oliver, "Interaction of Water with the Magnesium Oxide Surface", Trans. Faraday Soc., 61[12], 2754-62 (1965).

58. P.F. Eastman and I.B. Cutler, "Effect of Water Vapor on Initial Sintering of Magnesia", J. Am. Ceram. Soc., 49[10], 526-530 (1966).

59. K. Hamano, K. Asano, Y. Akiyama, et al., "Effects of Water Vapor Pressure on Sintering of Magnesia", Tokyo Inst. Technol., [4], 59-68 (1979). From Ceramic Abstracts, 59[9-10], 182 (1980).

60. R.F. Deacon, S.F.A. Miskin, and B.J. Ladell,
    "Gas Entrapment During the Sintering of Magnesia
    in Argon", Trans. Brit. Ceram. Soc., 65[10],
    585-601 (1966).

61. R.C. Doman, J.B. Bair, R.N. Mcnally, and
    A.M. Alper, "Phase Equilibria in the System
    CaO-MgO", J. Am. Ceram. Soc., 46[2], 313-316
    (1963).

62. J.W. Henney and J.W.S. Jones, "The Solid Solubility
    of CaO and SiO_2 in MgO and its Effect on the
    $MgO-CaO-SiO_2$ System at $1750^{O}C$", Trans. Brit.
    Ceram. Soc., 68[4], 201-203 (1969).

63. D.R.F. Spencer, T.W. Beamond, and D.S. Coleman,
    "The Solubility of CaO in MgO and its Effect on
    the $CaO-MgO-SiO_2$ System at $1800^{O}C$, Trans. Brit.
    Ceram. Soc., 70[1], 31-33 (1971).

64. E.M. Levin, C.R. Robbins, and H.F. McMurdie,
    Phase Diagram for Ceramists, Edited and Published
    by the American Ceramic Society (1964).

65. T. Hatfield, C. Richmond, W.F. Ford, and J. White",
    Compatibility Relationships Between the Periclase
    and Silicate Phases in Magnesite Refractories at
    High Temperatures", Trans. Brit. Ceram. Soc.,
    69[3], 53-58 (1970).

66. J. Henney and J.W.S. Jones, "The Effect of Controlled Additions of Silicate Phases on the Hot Strength of Magnesia", Trans. Brit. Ceram. Soc., 70[6], 209-213 (1971).

67. A. Muan, "Oxides of Transition Elements", in High Temperature Oxides - Part I, Edited by A.M. Alper, Academic Press, New York (1970).

68. N.L. Bowen and J.F. Schairer, "The System $MgO-FeO-SiO_2$", Am. J. Sci., 29[170], 151-217 (1935).

69. H. Schenck and W. Plaff, "Das System Eisen (II)-Oxyd-Magnesiumoxyd und seine Verteilungsgleichgewichte mit flussigem", Arch. Eisenhuettenw., 32[11], 741-751 (1961).

70. F.P. Glasser and E.F. Osborn, "The Ternary System $MgO-MnO-SiO_2$", J. Am. Ceram. Soc., 43[3], 132-140 (1960).

71. H. Schenck, M.G. Frohberg, and R. Nunninghoff, "The System MnO(-FeO)-MgO(-CaO) and its Distribution Equilibria with Molten Manganese with Respect to Fe-Mn Alloys", Arch. Eisenhuettenw, 35[4], 269-277 (1964).

72. B. Phillips, S. Somiya, and A. Muan, "Melting Relations of Magnesium Oxide-Iron Oxide Mixtures in Air", J. Am. Ceram. Soc., 44[4], 167-169 (1961).

73. P.V. Riboud and A. Muan, "Melting Relations of CaO-Manganese Oxide and MgO-Manganese Oxide Mixtures in Air", J. Am. Ceram. Soc., 46[1], 33-36 (1963).

74. B. Phillips and A. Muan, "Phase Equilibria in the System CaO-Iron Oxide-SiO_2 in Air", J. Am. Ceram. Soc., 42[9], 413-423 (1959).

75. F.P. Glasser, "The Ternary System CaO-MnO-SiO_2", J. Am. Ceram. Soc., 45[5], 242-249 (1962).

76. R.B. Snow, "Identification of CaO-MgO Orthosilicate Crystals, Including Merwinite ($3CaO.MgO.2SiO_2$), Through the Use of Etched Polished Sections", Trans. AIME, 172[ ], 121-136 (1947).

77. Test ANSI/ASTM C830-79, Annual Book of ASTM Standards, Part 17, American Society for Testing and Materials, Philadelphia (1980).

78. R.L. Fullman, "Measurement of Particle Sizes in Opaque Bodies", Trans. AIME, 197[3], 447-452 (1953).

79. M.W. Davies and F.D. Richardson, "The Non-Stoichiometry of Manganous Oxide", Trans. Faraday Soc., 55[4], 604-610 (1959).

80. C. Wagner and W. Schottky, "Theory of Arranged Mixed Phases", Z. Physik-Chem., B11, 163-210 (1930).

81. J.T. Jones, "The Diffusion of Manganese Oxide in Single Crystals of Periclase", Ph.D. Dissertation, University of Utah (1965).

82. J.T. Jones and I.B. Cutler, "Interdiffusion in the System Mn_xO-MgO", J. Am. Ceram. Soc., 54[7], 335-338 (1971).

83. G.E. Jungquist, "Final Sintering of Cr_2O_3 with Minor Additions of MgO and Sintering of MgO with Minor Additions of Cr_2O_3", Master Thesis, University of Missouri-Rolla (1971).

84. R.A. Robie and D.R. Waldbaum, "Thermodynamic Properties of Minerals and Related Substances at $298.15^{\circ}K$ ($25.0^{\circ}C$) and One Atmosphere (1.013 Bars) Pressure and at Higher Temperatures", Geological Survey Bulletin 1259, Washington (1968).

85. H.U. Anderson, Personal Communication, Ceramic Department, University of Missouri-Rolla (1982).

86. R. Lindner and G.D. Parfitt, "Diffusion of Radioactive Magnesium in Magnesium Oxide Crystals", J. Chem. Phys., 26[1], 182-185 (1957).

87. Y. Oishi and W.D. Kingery, "Oxygen Diffusion in Periclase Crystals", J. Chem. Phys., 33[3], 905-906 (1960).

88. D.R. McKenzie, A.W. Searcy, J.B. Holt, and R.H. Condit, "Oxygen Grain-Boundary Diffusion in MgO", J. Am. Ceram. Soc., 54[4], 188-190 (1971).

89. H. Hashimoto, M. Hama, and S. Shirasaki, "Preferential Diffusion of Oxygen Along Grain Boundaries in Polycrystalline MgO", J. Appl. Phys. 43[11], 4828-4829 (1972).

90. W.D. Kingery, "Plausible Concepts Necessary and Sufficient for Interpretation of Ceramic Grain-Boundary Phenomena: I, Grain-Boundary Characteristics, Structure, and Electrostatic Potential", J. Am. Ceram. Soc., 57[1], 1-8 (1974).

91. W.D. Kingery, "Plausible Concepts Necessary and Sufficient for Interpretation of Ceramic Grain-Boundary Phenomena: II, Solute Segregation, Grain-Boundary Diffusion, and General Discussion", J. Am. Ceram. Soc., 57[2], 74-83 (1974).

92. B.J. Wensch and T. Vasilos, "Grain-Boundary Diffusion in MgO", J. Am. Ceram. Soc., 47[2], 63-68 (1964).

93. B.J. Wensch and T. Vasilos, "Origin of Grain-Boundary Diffusion in MgO", J. Am. Ceram. Soc., 49[8], 433-436 (1966).

94. W.D. Kingery, W.L. Robbins, and A.F. Henriksen, "Surface Segregation of Aluminum (Spinel Precipitation) in MgO Crystals", J. Am. Ceram. Soc., 59[5-6], 239-241 (1976).

95. W.C. Johnson, "Grain Boundary Segregation in Ceramics", Metall. Trans., 8A[9], 1413-1422 (1977).

96. W.D. Kingery, T. Mitamura, J.B. Vander Sande, and E.L. Hall, "Boundary Segregation of Ca, Fe, La and Si in Magnesium Oxide", J. Mat. Sci., 14[7], 1766-1767 (1979).

97. J.R.H. Black and W.D. Kingery, "Segregation of Aliovalent Solutes Adjacent Surfaces in MgO", J. Am. Ceram. Soc., 62[3-4], 176-178 (1979).

98. Y.M. Chiang, A.F. Henriksen, and W.D. Kingery, "Characterization of Grain-Boundary Segregation in MgO", J. Am. Ceram. Soc., 46[7], 385-389 (1981).

99. E. Sonder, T.G. Stratton, and R.A. Weeks, "Kinetics of Fe^{2+} Oxidation and Fe^{3+} Reduction in MgO Single Crystals", J. Chem. Phys., 70[10], 4603-4608 (1979).

100. Internal Report DPD 118/81, MAGNESITA SA of Brazil (1981).

101. A. Muan and E.F. Osborn, "Phase Equilibria Among Oxides in Steelmaking", Addison-Wesley Publishing Company, Inc., Reading, Massachusetts (1965).

102. C. Wagner, "Beitrag Zur Theorie des Anlaufvorgangs", Z. Phys. Chem., B21, 25-41 (1933).

VITA

Alamar Kasan Duarte was born on June 30, 1952 in
Areado, Minas Gerais, Brazil. He received his primary
education in Guaxupé, M.G., Brazil and his secondary
education at Colegio Universitário de Minas Gerais in
Belo Horizonte, M.G., Brazil. He received a Bachelor of
Science degree in Metallurgical Engineering from
Universidade Federal de Minas Gerais, Brazil in 1974.
Upon graduation he accepted a position as Research
Assistant Engineer with MAGNESITA SA of Brazil. In 1978
he became manager of the Development Group of the
Department of R & D of MAGNESITA SA. In August 1980
MAGNESITA SA offered him a graduate course, and since
then he has been enrolled at the University of Missouri-
Rolla to get his Master of Science degree in Ceramic
Engineering.

APPENDIX A

CHEMICAL REAGENTS

1. Manganous Carbonate (Powder) - Manganese (II) Carbonate

     Assay (as Mn) 44.0%

     Insoluble in HCl 0.005%

     Chloride (Cl) 0.002%

     Sulfate (SO$_4$) 0.002%

     Substances not Precipitated
     by (NH$_4$)$_2$S (as SO$_4$). 0.11%

     Other heavy metals (as Pb) 0.002%

     Iron (Fe) 0.001%

     Zinc (Zn) 0.005%

          From J.T. Baker Chemical Company,
          Phillipsburg, New Jersey

2. Calcium Carbonate (Powder) - Low in alkalies

     Assay (CaCO$_3$) 100.3%

     Insoluble in HCl 0.005%

     Ammonium Hydroxide Precipitate 0.005%

     Chloride (Cl). 0.005%

     Sulfate (SO$_4$) 0.005%

     Barium (Ba) 0.001%

     Heavy Metals (as Pb) 0.005%

     Iron (Fe) 0.005%

     Magnesium (Mg) 0.005%

     Potassium (K) 0.009%

     Sodium (Na) 0.004%

     Strontium (Sr) 0.01%
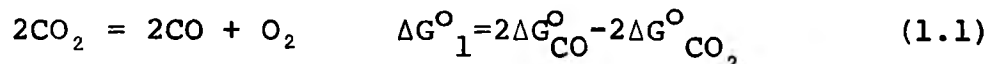
          From J.T. Baker Chemical Company,
          Phillipsburg, New Jersey

APPENDIX B

OXYGEN GAUGE CELL - EMF CALCULATIONS FOR
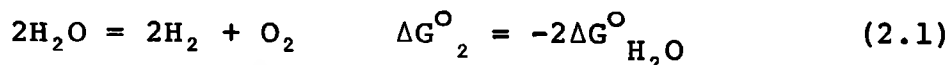## $P_{O_2} = 10^{-7}$ KPa-CO_2/H_2 BUFFER SYSTEM

1. Assuming the reaction[101]:

$$2CO_2 = 2CO + O_2 \qquad \Delta G^O_1 = 2\Delta G^O_{CO} - 2\Delta G^O_{CO_2} \qquad (1.1)$$

where:

$$K_1 = P_{O_2} \left(\frac{P_{CO}}{P_{CO_2}}\right)^2 = \exp(-\Delta G^O_1/RT) \qquad (1.2)$$

2. Assuming the reaction:

$$2H_2O = 2H_2 + O_2 \qquad \Delta G^O_2 = -2\Delta G^O_{H_2O} \qquad (2.1)$$

where:

$$K_2 = P_{O_2} \left(\frac{P_{H_2}}{P_{H_2O}}\right)^2 = \exp(-\Delta^O G_2/RT) \qquad (2.2)$$

3. Combining equations (1.1) and (2.1):

$$CO_2 + H_2 = CO + H_2O \qquad \Delta G^O_3 = \Delta G^O_{CO} + \Delta G^O_{H_2O} - \Delta G^O_{CO_2}$$

$$\Delta G^O_3 = \frac{1}{2}(\Delta G^O_1 - \Delta G^O_2) \qquad (3.1)$$
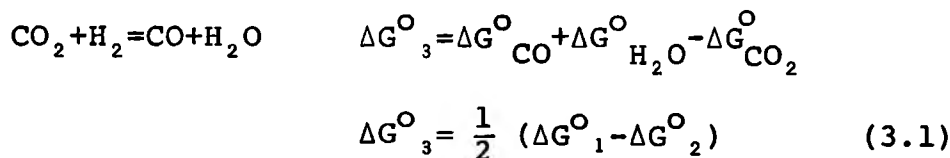
where:

$$K_3 = \frac{P_{CO}}{P_{CO_2}} \frac{P_{H_2O}}{P_{H_2}} = \left(\frac{K_1}{K_2}\right)^{1/2} = \exp(-\Delta G^O_3/RT) \qquad (3.2)$$

4. Defining:

$$P_{H_2}(i),\ P_{CO_2}(i) = \text{initial partial pressure}$$
of H_2 and CO_2 at room temperature.

$$P_{CO_2},\ P_{H_2},\ P_{CO},\ P_{H_2O},\ \text{and}\ P_{O_2} =$$
equilibrium partial pressures of the various gas species at elevated temperature

Then:

$$P_{CO_2}(i) = P_{CO_2} + P_{CO} \tag{4.1}$$

$$P_{H_2}(i) = P_{H_2} + P_{H_2O} \tag{4.2}$$

5. Defining:

$$r = \text{original gas mixing ratio} =$$
$$P_{CO_2}(i)/P_{H_2}(i)$$

Hence:

$$r = \frac{P_{CO_2} + P_{CO}}{P_{H_2} + P_{H_2O}} = \frac{P_{CO}}{P_{H_2O}}\ \frac{[1 + (P_{CO_2}/P_{CO})]}{[1 + (P_{H_2}/P_{H_2O})]} \tag{5.1}$$

Since K_1 and K_2 are much smaller than K_3, we have from equation (3.1) that P_{CO} is equal to P_{H_2O}, and hence:

$$r \simeq \frac{1 + (P_{CO_2}/P_{CO})}{1 + (P_{H_2}/P_{H_2O})} \tag{5.2}$$

6. Let: $x = P_{CO_2}/P_{CO}$ and $y = P_{H_2}/P_{H_2O}$.

Therefore, we have for equations (5.2) and (3.2):

$$r = \frac{1 + x}{1 + y} \qquad (6.1)$$

and

$$k_3 = \frac{1}{x \cdot y} \qquad (6.2)$$

Hence,

$$r = \frac{x(1+x)}{x + (1/K_3)} \qquad (6.3)$$

7. The electromotive force generated in the Oxygen Sensor is given by an equation derived by Wagner[102]:

$$E = t_i \frac{RT}{4F} \ln \frac{P_{O_2}}{P_{O_2(ref)}} \qquad (7.1)$$

where: E = e.m.f. developed by the cell(V), T is temperature ($^\circ$K), R is the universal gas constant (8.314 J/$^\circ$K.mol), F is the Faraday's constant (96490 C/mol), t_i is the ionic transport number which is 1 for the ZrO_2-CaO electrolyte operated at 1273°K, $P_{O_2(ref)}$ is the partial pressure of oxygen reference in the outer part of the electrolyte (0.21 atm for air), and finally P_{O_2} is the partial pressure of oxygen of the gas which we desire to

measure at the interior of the electrolyte. In our case we want an atmosphere of $P_{O_2} = 10^{-9}$ atm at the high operating temperatures for the sintering furnace. Therefore, it is necessary a correction for P_{O_2} measured at $1273^{O}K$ by the Oxygen Sensor.

8. Defining:

$P_{O_2 (T)}$ = Partial pressure of oxygen at the sintering temperature

$P_{O_2 (1273)}$ = Partial pressure of oxygen at the operation temperature of the Oxygen Sensor

Therefore,

$$E = \frac{RT}{4F} \ln \frac{P_{O_2}(1273)}{P_{O_2}(ref)} \qquad (8.1)$$

9. Finally, the procedure for calculating the E.m.f. of the Oxygen Sensor, operated at $1273^{O}K$, for a given $P_{O_2}(T)$ is given by:

- Calculate $\Delta G^{O}_{1(T)}$ from equation (1.1)

- Calculate $K_{1(T)}$ from equation (1.2)

- Calculate $\Delta G^{O}_{2(T)}$ from equation (2.1)

- Calculate $K_{2(T)}$ from equation (2.2)

- Calculate $x_{(T)}$ from equation 1.2, where

$$x_{(T)} = (P_{O_2}/K_1)^{1/2} \qquad (9.1)$$

- Calculate $K_{3(T)}$ from equation (3.2),

where, $K_{3(T)} = (K_1/K_2)^{1/2} \qquad (9.2)$

- Calculate r from equation (6.3)

- Calculate $K_{3\ (1273^O K)}$ from equation (3.2)

- Calculate $x_{(1273^O K)}$ from equation (6.3),

where:

$$x_{(1273^O K)} = (-(1-r) + (1-r)^2 + 4r/K_{3\ (1273)})/2$$

$$(9.3)$$

- Calculate $P_{O_2(1273^O K)}$ from equation (1.2),

where:

$$P_{O_2(1273^O K)} = K_{1(1273^O K)} \cdot x^2_{\ (1273)}$$

- Calculate E from equation (8.1) where

$$E = \frac{RT}{4F} \ln \frac{P_{O_2(1273)}}{P_{O_2(ref)}}$$

The results for the temperature being investigated are shown in Table XVII.

149

TABLE XVII

E.M.F. CALCULATIONS FOR THE OXYGEN SENSOR

Temperature (^{o}C)	$\Delta G^{o}_f{}^{84}$(CO) joules/mole	$G^{o}_f{}^{84}$(CO$_2$) joules/mole	$G^{o}_f{}^{84}$(H$_2$O) joules/mole	P_{O_2}(T) (KPa)	$P_{CO_2}(i)/P_{H_2(i)}$	P_{O_2}(1000°C) (KPa)	E.m.f. (V)
1000	-224,144	-396,194	-177,406	10^{-7}	-	-	-
1520	-268,631	-396,386	-147,595	10^{-7}	0.45135	1.0130×10^{-13}	-0.904
1580	-273,678	-396,386	-144,115	10^{-7}	0.29192	2.8816×10^{-14}	-0.938
1640	-278,725	-396,386	-140,645	10^{-7}	0.18895	1.1305×10^{-14}	-0.964
1700	-283,760	-396,382	-137,159	10^{-7}	0.12281	4.5620×10^{-15}	-0.989
1760	-288,794	-396,382	-133,673	10^{-7}	0.08066	1.9084×10^{-15}	-1.013